INVESTIGATING GLYCOPROTEIN-DEPENDENT AND -INDEPENDENT CELL SURFACE ATTACHMENT MECHANISMS OF HEMORRHAGIC FEVER VIRUSES

by

MARISSA DANIELLE ACCIANI

(Under the Direction of Melinda A. Brindley)

ABSTRACT

Lassa virus (LASV) and Ebolavirus (EBOV) are enveloped, negative sense, RNA viruses that can cause severe hemorrhagic fever disease in humans. These pathogens continually circulate in animal reservoirs and future zoonotic crossover events and outbreaks are a certainty. While 80% of patients diagnosed with LASV experience mild symptoms, this virus infects hundreds of thousands of people annually and causes severe disease in 20% of hospitalized cases. In contrast, EBOV outbreaks occur more sporadically but the case fatality rate ranges from 50-90%. An optimal way to prevent a virus from establishing infection in the human host is to inhibit virus-cell entry, which includes virus-cell surface attachment, internalization, and fusion, resulting in the release of the viral genome into the cell cytoplasm. Entry is predominantly mediated by viral glycoproteins (GPs), which coat the viral envelope and facilitate cell surface attachment and fusion. LASV and EBOV can also attach to cell surfaces by interacting with phosphatidylserine receptors (PSRs), which bind to host-derived phospholipid phosphatidylserine (PS) in the viral envelope. Therefore, targeting both GP and envelope-mediated mechanisms may be required to fully inhibit cellular uptake of these viruses. To

better understand and target LASV and EBOV entry mechanisms, we aim to 1) characterize the LASV receptor binding site within glycoprotein subunit 1 (GP1) using site-directed mutagenesis, 2) define specific cellular PS scramblases required for EBOV envelope PS, and 3) investigate the role of cellular PS flippases in EBOV replication.
INDEX WORDS: Lassa, Ebola, entry, glycoprotein, apoptotic mimicry, scramblases, flippases

INVESTIGATING GLYCOPROTEIN-DEPENDENT AND -INDEPENDENT CELL SURFACE ATTACHMENT MECHANISMS OF HEMORRHAGIC FEVER VIRUSES

by

MARISSA DANIELLE ACCIANI

B.S., The University of North Carolina, 2013

A Dissertation Submitted to the Graduate Faculty of The University of Georgia in Partial Fulfillment of the Requirements for the Degree

DOCTOR OF PHILOSOPHY

ATHENS, GEORGIA

2021

INVESTIGATING GLYCOPROTEIN-DEPENDENT AND -INDEPENDENT CELL SURFACE ATTACHMENT MECHANISMS OF HEMORRHAGIC FEVER VIRUSES

by

MARISSA DANIELLE ACCIANI

Major Professor: Melinda Brindley

Committee: Brian Cummings
Biao He
Julie Moore
Stephen M. Tompkins

Electronic Version Approved:

Ron Walcott
Dean of the Graduate School
The University of Georgia
December 2021

ACKNOWLEDGEMENTS

I'd like to acknowledge my mentor, Dr. Melinda Ann Brindley, who has empowered me as a scientist beyond my own expectations.

I'd also like to thank my sister Justine and my dad Michael for their support. I couldn't be more grateful we are a team. I dedicate this work to you and to my mom Sheila, whom we lost. Mom, my achievements are your achievements.

Thank you to my dogs Archie and Milo, who are snoozing soundly next to me at 1:50AM like they have for countless nights while I pursued my doctorate.

TABLE OF CONTENTS

CHAPTER 1: DISSERTATION OVERVIEW

Specific Aims Overview

Lassa virus (LASV) and Ebola virus (EBOV) are two of the most globally threatening emerging pathogens. LASV and EBOV are the causative agents of Lassa fever and Ebola virus disease in humans, and outbreaks of these diseases regularly devastate Western and Central Africa. Distinguishing between Lassa fever and Ebola virus disease cases is a major challenge for healthcare workers, as both diseases present with flu-like symptoms early in infection and can rapidly progress to fatal hemorrhagic fever in severe cases. It is estimated that approximately 300,000 to 500,000 Africans are infected by LASV annually. While 80% of LASV cases are mild, the case fatality rate for those hospitalized is 15-20% and has historically reached up to 50%. In contrast, Ebola outbreaks occur more sporadically, but the case fatality rate ranges from 25-90%. The largest EBOV outbreak occurred from 2014 to 2016, with 28,646 confirmed cases and 11,323 deaths, accounting for approximately three times more deaths than all previous outbreaks combined. Both LASV and EBOV demonstrate high epidemic potential. These pathogens continually circulate in animal reservoirs and future zoonotic crossover events are a certainty. Therefore, there is a critical need for rapidly adaptable vaccine and antiviral platforms to control ongoing and prevent future outbreaks.

An optimal way to prevent a virus from establishing infection in the human host is to inhibit virus-cell entry. This stage in the viral replication cycle is mediated by viral glycoproteins (GPs), which coat the viral envelope and are the only viral proteins

exposed to the extracellular environment. Viral glycoproteins attach virions to the cell surface, trigger internalization, and facilitate genome release into the cytoplasm. These functions are carried out by specific domains within the glycoprotein (i.e. receptor-binding domains [RBDs] and fusion domains), but also require host factors such as surface receptors, endosomal receptors, proteases, and/or environmental conditions such as low pH. Viral glycoprotein functional domains, particularly the RBDs, are ideal targets for therapeutics (e.g. neutralizing antibodies) because they are accessible outside of the cell and are essential for viral replication.

Many viruses, including LASV and EBOV, can also bind to cell surfaces through interaction with phosphatidylserine receptors (PSRs), which bind to phosphatidylserine (PS) in the viral envelope. This strategy is termed apoptotic mimicry. PSRs typically mediate the uptake and clearance of PS-coated apoptotic cells and debris. Viruses that mimic the apoptotic debris can become internalized through a similar pathway. Several groups demonstrated that exogenously producing PSRs on cell surfaces *in vitro* enhances viral entry or confers virus susceptibility to previously unsusceptible cells. PSR TIM-1 was also implicated in EBOV pathogenesis *in vivo* in mice. Less clear, however, is how viral envelopes acquire PS. Unlike viral glycoproteins, which are encoded in the viral genome, the lipid envelopes are pinched off directly from host cell membranes during budding. Therefore, for enveloped viruses budding from the cell surface, envelopes presumably reflect the composition of the plasma membrane. Because PS is typically sequestered in cells, oriented on the cytoplasmic side of the inner leaflet, a mechanism explaining viral envelope PS exposure and engagement of PSRs was needed. It was theorized that viruses benefitting from apoptotic mimicry induce endogenous cellular PS-

scrambling mechanisms, such as apoptosis, resulting in envelopes with externalized PS. However, the detailed process and host factors involved were not defined.

To better understand and target LASV and EBOV entry, we aimed to 1) characterize the LASV receptor binding site within glycoprotein subunit 1 (GP1) using site-directed mutagenesis, 2) define specific cellular PS scramblases required for external EBOV envelope PS, and 3) investigate the role of cellular PS flippases in EBOV replication.

CHAPTER 2: LITERATURE REVIEW

Lassa virus impact.

Lassa virus (LASV) is an Old-World (OW) arenavirus endemic to West Africa, causing an estimated 300,000 to 500,000 cases of Lassa fever (LF) and 5,000 to 10,000 deaths in this region every year. While 80% of infections result in mild flu-like symptoms, 20% of infections result in severe disease characterized by vomiting, mucosal and internal bleeding, seizures, coma, shock, and deafness. While the overall LF case fatality rate is estimated to be 1%, the case fatality rate of hospitalized patients is approximately 20%. LASV is particularly threatening to pregnant women, as those infected face a 95% possibility of spontaneous abortion and death (1). Studies have also noted significant sequelae in survivors such as hearing loss, ataxia, and encephalopathy (2, 3). Thus far, there are no approved vaccines or treatments to ease the burden caused by LASV (4). Due to LASV's widespread disease burden, zoonotic spillover potential, and the lack of adequate disease control methods, LASV is listed as a category A priority pathogen (5).

Lassa virus transmission and pathogenesis.

LASV is primarily transmitted to humans from the multimammate rodent *Mastomys natalensis* through inhalation or direct contact with rodent excreta (6). Human-human transmission has also occurred in hospital settings. Our current knowledge surrounding LASV pathogenesis in humans is limited; however, *in vitro* and non-human primate (NHP) models have provided insight into initial target cell types and viral spread

(7). LASV infection likely begins with the invasion of macrophages and dendritic cells, which are also the first targets of closely-related OW arenavirus LCMV (8) and New-World (NW) arenavirus Junín (9). With the discovery that these professional antigen-presenting cells fail to release antiviral cytokines when infected with LASV, it was proposed that these cells are key in suppressing the immune system, permitting LASV to spread throughout the body (10). In late stages of both human and NHP LASV infections, virus is detected in most organs throughout the body, including the liver, cerebellum, kidneys, adrenal glands, intestines, lungs, thymus, and pancreas, resulting in multiorgan failure and death (11).

Lassa virus morphology and replication.

Lassa virus particles consist of a negative-sense RNA genome encapsulated by a lipid envelope studded with glycoprotein (GP) trimers. The bi-segmented genome encodes four structural proteins; the S segment encodes the nucleoprotein (NP) and glycoprotein complex precursor (GPC), while the L segment encodes the viral RNA-dependent RNA polymerase (L) and matrix protein (Z). The single LASV GPC precursor polypeptide travels to the ER, where it is cleaved into a stable signal peptide (SSP) and subunits GP1 and GP2 (all non-covalently linked), trimerizes, and is glycosylated as it travels to the plasma membrane (12, 13). These GPs, classified as class I viral fusion proteins, are incorporated into particles during budding (14).

LASV GP1, the receptor-binding domain, directly attaches to alpha-dystroglycan (αDG) on the cell surface to initiate a macropinocytosis-like internalization mechanism (15). LASV can also interact with cell surface attachment factors such as heparan sulfate, C-type lectins dendritic cell-specific ICAM-3-grabbing non-integrin (DC-SIGN) and

lymph node sinusoidal endothelial cell C-type lectin (LSECTin), and apoptotic clearance phosphatidylserine receptors (PSRs) in the T-cell immunoglobulin mucin domain receptor (TIM) and TAM (Tyro3, Axl, Mer) protein families to trigger internalization (16-20). LASV is then trafficked to acidic late endosomes, where GP1 switches affinity from αDG to lysosome-associated membrane protein 1 (LAMP1). While LAMP1 is not essential for entry, GP1-LAMP1 interactions reduce GP low-pH fusion requirements and may anchor LASV particles close to the endosomal membrane (21-26). GP1 then dissociates from GP2, freeing this subunit to undergo conformational changes that fuse the viral envelope to the endosomal membrane, creating a fusion pore through which the viral genome is released (27-29). LASV L complexed with NP and genome are sufficient to initiate genome replication and mRNA transcription (30-32). Directed by LASV Z, newly translated viral proteins and genome copies then assemble into particles and bud through the plasma membrane (33).

Lassa virus cell surface receptor usage.

As was mentioned above, LASV can attach to cell surfaces using high-affinity receptor dystroglycan (DG). DG is an extracellular matrix receptor consisting of a transmembrane β subunit non-covalently linked to an extracellular glycosylated α subunit. It was first isolated from skeletal muscle and is critical for muscle fiber stability and numerous other developmental and signaling functions in mice (34). DG is ubiquitously expressed and widely conserved among vertebrates; thus, it was originally considered to be the major receptor for LASV (35). Additional DG research revealed that its biological function and role as a LASV receptor are dependent on the addition of matriglycans, specific glycosylation moieties, to αDG by like-

acetylglucosaminyltransferase (LARGE). Upon closer examination, the distribution of functional DG was highly variable in tissues and did not always correlate with LASV tropism (19, 34, 36-41). Therefore, scientists continued to explore alternative LASV attachment factors, later identifying PSRs TIM1, Axl, and Tyro3 (16, 18, 19). *In vitro* and *ex vivo* studies demonstrate that while LASV binds to αDG with a higher affinity than PSRs; PSRs can solely mediate LASV entry in its absence. The *in vivo* contributions of αDG, and PSRs to LASV pathogenesis remain unclear. Groups studying LCMV found that pathogenesis in LARGE (41) and Axl (42) knockout mice did not significantly differ from wild-type mice. This suggests there may be multiple LASV cell surface attachment factors sufficient for facilitating entry across target cell types, which makes it particularly challenging to 1) define the roles of each attachment factor individually and 2) effectively block LASV entry using specific anti-attachment strategies.

Ebola virus impact.

Ebola virus (EBOV) is a filamentous filovirus that causes sporadic but deadly outbreaks of Ebolavirus disease (EVD) in Western and Central Africa. Like LASV, early EBOV infections are characterized by non-specific flu-like symptoms; however, disease can progress to diarrhea, vomiting, and hemorrhaging, and death in 50-90% of cases. EBOV infection also causes long-term sequelae in survivors, who report arthralgias, uveitis, neurological, dermatological, gastrointestinal, and/or auditory symptoms. While these sequelae are typically attributed to inflammation during acute EBOV infection, viral RNA and infectious virus can also persist in immune privileged sites long after disease onset (43-45). Currently there is one FDA-approved vesicular stomatitis-based vaccine called Ervebo. In addition, Zabdeno® (adenovirus-based) and Mvabea® (vaccinia

virus-based) are authorized for use in Europe. All of these vaccines provide immunity to the Zaire EBOV species, which is one of four pathogenic species in humans (46).

Ebola virus transmission and pathogenesis.

Many human Ebola virus outbreaks are traced back to infected great apes and duikers, but these animals are not considered to be EBOV reservoirs due to their high mortality. Thus, the natural EBOV reservoir is still unclear. Considering scientists have isolated short EBOV genomic fragments and/or antibodies from bats, and bats are reservoirs for a closely related filovirus, Marburg virus, they are the most likely candidate (47, 48). Once EBOV spills into the human population, the virus can then spread from human-to-human through contact with infected tissues or bodily fluids. Major risk factors for human-to-human EBOV transmission include care of infected patients either by healthcare workers or members of the household, or during funeral practices where the deceased are washed and dressed (49). Of increasing concern is the ability of EBOV to transmit sexually, as infectious virus and/or RNA can persist in semen in survivors of non-fatal EBOV disease. Infectious virus has been isolated from semen >200 days after initial disease onset, and EBOV RNA can persist > 600 days after disease onset. While confirmed cases of sexual transmission are rare, with eight cases documented thus far, the ability of virus to persist in humans increases the likelihood of non-zoonotic EBOV reoccurrences (44).

The current model of EBOV pathogenesis (established using NHP models) begins with the infection of macrophages and dendritic cells at the site of infection. These cells disseminate virus to the spleen and lymph nodes and then to organs throughout the body (50). Unlike LASV, EBOV infection activates macrophages and dendritic cells, resulting

in additional macrophage recruitment, a pro-inflammatory “cytokine storm”, bystander lymphocyte apoptosis, and the breakdown of endothelial barriers (45, 50). The widespread cell and tissue damage from EBOV and EBOV-induced inflammation then ultimately leads to multiorgan dysfunction and death.

Ebola virus morphology and replication.

Ebola virus is an enveloped, negative-sense, single-stranded RNA virus known for its distinct worm-like morphology. Its genome encodes seven structural proteins including matrix virion protein VP40, full-length glycoprotein precursor (GP_0), and nucleocapsid components nucleoprotein (NP), VP24, VP30, VP35, and the RNA-dependent RNA polymerase (L). Due to L-mediated co-transcriptional RNA editing, the genome also encodes for truncated, secreted versions of GP called soluble GP (sGP, 70% of mRNA transcripts) and small soluble GP (ssGP, 5% of mRNA transcripts). Evidence suggests sGP may act as both a GP antibody decoy and anti-inflammatory immune modulator during EBOV pathogenesis (51). The role of ssGP remains unknown. During structural EBOV GP maturation, furin proteases in the Golgi cleave GP_0 into GP_1 and GP_2 to form a heterodimer linked by disulfide bonds. These dimers then form a heterotrimer and are glycosylated and trafficked to the plasma membrane (14).

EBOV uses several attachment factors on the cell surface to facilitate internalization. Glycans on GP_1 bind to glycosaminoglycans (GAGs) and many types of C-type lectin receptors such as DC-SIGN, LSECTin, liver/lymph node-specific ICAM-3 grabbing non-integrin (L-SIGN), asialoglycoprotein receptor 1 (ASGPRI), and human macrophage galactose- and acetylgalactosamine-specific C-type lectin (hMGL) (52). Lipid in the EBOV envelope can also bind particles to TIM and TAM-family PSRs in a

glycoprotein-independent manner (52). Once bound, EBOV particles are then macropinocytosed and trafficked deeper into cells as endosomal cargo. Early endosomal cathepsins B and L proteolytically process the GP and remove the mucin domain, revealing a new epitope that enables GP_1 to bind to late endosomal receptor Niemann-Pick C1 (NPC1). Binding to NPC1, along with a yet to be identified step, initiates conformational changes in GP_2, triggering GP_2-mediated viral-cell membrane fusion and ribonucleocapsid release. EBOV replication begins with viral mRNA transcription and translation. Genome replication occurs in cytoplasmic inclusion bodies, where new ribonucleocapsid complexes are assembled. VP40 then regulates ribonucleocapsid transport to the cell surface in addition to particle assembly and egress (53).

Ebola virus cell surface receptor usage.

Because EBOV lacks a high affinity cell surface receptor, scientists aiming to effectively block EBOV entry are tasked with prioritizing a multitude of attachment factors. In addition to GAGs (54) and C-type lectin receptors (55-58), EBOV can also enter cells using PSRs TIM-1, TIM-4, Tyro3, Axl, and Mer (59-65). Most studies examining PSRs and filovirus entry are in cell culture. Thus far, only two studies have shed light on EBOV PS receptor usage *in vivo* (66, 67). First, Younan et al observed improved survival in $TIM^{-/-}$ C57BL/6 mice infected with mouse-adapted EBOV. They found, however, that deleting TIM-1 did not affect viremia. Instead, infected $TIM^{-/-}$ mice exhibited reduced T-cell activation and inflammatory mediator production, suggesting that TIM-1 plays more of a role in inciting the characteristic cytokine storm than it does as an entry factor (66). In contrast, Brunton et al found both increased survival and reduced viremia in $TIM\text{-}1^{-/-}$ BALB/c IFN-αβ receptor-deficient (Ifnar-/-) mice infected

with recombinant vesicular stomatitis virus (VSV) encoding the EBOV GP (rVSV/EBOV-GP). Importantly, they did not observe reduced T-cell activation or a dampened cytokine response, and wild-type VSV was equally virulent in knockout and parental mice. Therefore, they concluded that these effects were more likely due to TIM-1 serving as a late-stage entry factor (67).

While *in vivo* studies investigating PSRs in both LASV and EBOV entry are somewhat contradictory, an abundance of *in vitro* data suggests continued exploration into PSR-mediated viral entry strategy is a worthwhile avenue to target and block viral entry.

Apoptotic mimicry.

Viral entry through PSRs is referred to as apoptotic mimicry, as these receptors typically mediate the clearance of apoptotic cells and debris (i.e. efferocytosis). During efferocytosis, PSRs on professional and non-professional phagocytes bind to plasma membrane lipid phosphatidylserine (PS), which is only present at high levels on apoptotic cell surfaces. In viral apoptotic mimicry, PS exposed on the outer leaflet of viral envelopes bind to PSRs, triggering particle internalization that leads to productive infection rather than clearance (68).

Beyond LASV and EBOV, apoptotic mimicry can enhance or fully orchestrate the entry of a diverse array of pathogenic enveloped viruses including dengue, West Nile, yellow fever, and Zika flaviviruses; chikungunya, Sindbis, and eastern equine encephalitis alphaviruses; Hantaan and Andes bunyaviruses; SARS-CoV-2 (a coronavirus); vaccinia (a poxvirus), and HIV (a retrovirus) (69-80). Even the infectivities of non-enveloped enteroviruses and hepatitis A virus are enhanced through PSRs because

naked particles and RNA can be delivered into cells as cargo in PS-rich exosomes (81, 82).

Viral entry via apoptotic mimicry presents several proviral advantages, which were recently reviewed (83). Firstly, PSRs and efferocytosis mechanisms are broadly expressed and highly conserved across species, expanding cell/tissue tropism and host range for viruses that can exploit PSR functionality. Secondly, non-specific cell surface attachment through viral envelope PS, rather than GP, reduces the risk of neutralization by anti-GP antibodies in the extracellular environment. Lastly, entry via apoptotic mimicry may bypass certain innate immune responses typically triggered by virus infection because efferocytosis promotes an anti-inflammatory state in phagocytes (84). To engage PSRs, viruses must contain PS on the exposed leaflet of the envelope bilayer. Confirmation of PS-rich viral envelopes has been obtained for many viruses (60, 69, 72, 73, 85-88). Wild-type LASV particles have not yet been directly stained for PS (typically achieved by using anti-PS antibody bavituximab or PS-binding protein annexin V [AnV]); however, a study using recombinant LMCV-LASVGP found that pretreating particles with AnV inhibits entry in cells lacking functional DG (19). An older study located PS on the surface of New World arenavirus, Pichinde, using bavituximab in an ELISA (88). For EBOV, exposed PS was found on wild-type virions and VP40-based VLPs using AnV staining (89, 90).

While numerous viral envelope PS-PSR relationships have been identified in the past 10-20 years, the mechanism by which virions acquire outer leaflet PS remains unclear. This phenotype is particularly puzzling for viruses containing plasma membrane-derived envelopes (i.e. arenaviruses, filoviruses, alphaviruses, retroviruses), because PS

is predominately restricted to the inner leaflet of the plasma membrane. Scientists proposed these viruses trigger apoptosis, resulting in PS exposure on both the plasma membrane and emerging viral particle envelopes. However, considering cells have multiple PS exposure mechanisms, virus-induced PS exposure may be complex and warrants detailed investigation.

Cellular PS distribution.

PS is an essential anionic phospholipid that accounts for 5-10% of the total cellular lipid content. PS synthesis occurs in the mitochondria-associated membranes of the endoplasmic reticulum (ER), after which it is non-uniformly transported throughout the cell via vesicular and non-vesicular transport pathways. It is most abundant in the plasma membrane (10-15% of total plasma membrane lipid content), but is also found in early (8.5%) and late endosomes (2.5-3.9%), the Golgi (5%), ER (3-5), and mitochondria (1%) (91). In the plasma membrane, PS distribution is heavily biased towards the cytoplasm. While it makes up about 15% of the total lipid in the plasma membrane, it accounts for about 30% of the inner/cytoplasmic leaflet. Due to its negatively charged polar head group, the concentration of inner leaflet PS can impact the localization of plasma membrane-associating proteins, including those required for endocytosis, and is important for promoting membrane curvature (92). Transmembrane P4-ATPases termed flippases maintain asymmetric PS distribution by binding to outer leaflet PS and flipping it to the inner leaflet (92, 93).

Cellular PS exposure is involved in several significant biological processes, including blood coagulation, muscle fiber development, bone mineralization, fertilization, and apoptotic cell removal (94). Spontaneous migration of the polar PS headgroup across

the hydrophobic bilayer, however, is highly energetically unfavorable and occurs at a very low rate (95). To overcome this energy barrier and achieve rapid PS exposure, cells inactivate flippases and activate phospholipid-shuffling scramblases, which provide hydrophilic transmembrane pathways for phospholipid headgroups (96). Several plasma membrane-localized scramblase families have been identified. The TMEM16 protein family includes calcium-dependent scramblases that facilitate temporary PS exposure in response to an increase in intracellular calcium (97). The XKR protein family includes scramblases activated by caspase cleavage. XKR8, the most well-characterized member, facilitates the non-reversible exposure of PS after apoptosis induction (98).

Because virus infection can impact intracellular calcium levels and/or induce apoptosis, there is a possibility that host cell flippases and scramblases also play a role in exposed viral envelope PS by altering PS asymmetry in infected cell plasma membranes.

Flippases.

Host cell P4-ATPases transport phospholipids across membrane leaflets, often against their concentration gradients, in an ATP-dependent manner (99, 100). Out of 14 human P4-ATPases, ATP11C, ATP11A, and ATP8A2 localize to the plasma membrane and demonstrate PS-specific flippase activity (101). These flippases form heterodimers with CDC50a, a protein subunit required for ATPase folding and trafficking to the plasma membrane (102). Both P4-ATPases and CDC50a are highly evolutionary conserved in eukaryotes (100). Structural analysis showed that ATP11C undergoes cyclical conformational changes enabling the protein to attract outer leaflet PS headgroups and funnel them through a transmembrane crevice to the inner leaflet. The ATP11C/CDC50a complex is constitutively active; however, its activity can be

temporarily downregulated by calcium or permanently inhibited by caspases (103). To date, the only evidence tying mammalian flippases to virus replication arose from CRISPR screens for Lujo virus and SARS-CoV-2 host cell factors, which identified CDC50a as being important for cell susceptibility to virus (104, 105).

Scramblases.

The Nagata group also identified TMEM16F and XKR8, transmembrane scramblases that localize to the plasma membrane and disrupt PS asymmetry in response to calcium signaling and apoptosis, respectively (106-108). TMEM16F is a member of the conserved transmembrane protein 16 (TMEM16) family, which consists of 10 total members including TMEM A-H, J, and K. While TMEM16 C, D, F, G, and J demonstrate calcium-dependent phospholipid scrambling activity, TMEM16F is the most prominent and well-characterized (109-112). During spikes in intracellular calcium, direct binding of calcium molecules to TMEM16F dimers opens a phospholipid transport cleft (113-115). In addition to mediating platelet PS exposure essential for blood coagulation (107, 116) and microvesicle formation during bone mineralization (117), TMEM16F was also implicated in HIV and SARS-CoV-2 fusion (118-120) and exposed PS on the EBOV envelope (89).

The human XKR family consists of 9 members (1-9), a subset of which localize to the plasma membrane and externalize PS (XKR4, XKR8, and XKR9). XKR8 is well conserved among vertebrates, ubiquitously expressed, and demonstrates the strongest PS scrambling activity (121). XKR8 forms a heterodimer with basigin or neuroplastin, which are required for XKR8 localization to the plasma membrane (122). XKR8 is activated during apoptosis following caspase 3/7 cleavage, leading to cell membrane PS exposure

and phagocyte engulfment (123). The Nagata group demonstrated that kinase phosphorylation can also activate XKR8 in murine Ba/F3 pro B cells; however, this mechanism has not been confirmed with human XKR8 (124). A study by Nanbo et al indicates that activated XKR8 is required for EBOV virus-like particle (VLP) envelope PS and internalization into Vero E6 cells (90).

The Nagata group also studied the roles of these flippases and scramblases in apoptotic cell uptake by macrophages. They employed murine W3 cells producing caspase cleavage resistant ATP11C that remained active during apoptosis. Upon treatment with apoptosis inducer FasL, these cells did not expose PS and were not engulfed my macrophages (125). This suggests that flippase inactivation and scramblase activation are both required for sufficient efferocytosis, and likely also required for viral envelope PS exposure and entry using PSRs.

Outstanding Questions.

Hemorrhagic fever viruses LASV and EBOV demonstrate flexible cell surface receptor usage, which likely contributes to their broad cell/tissue tropisms and cross-species transmission potential. This poses a particular challenge for those seeking to prevent LASV/EBOV disease pathogenesis by inhibiting viral entry. Sufficiently blocking cell surface attachment may require targeting the viral envelope and multiple epitopes on the glycoprotein at once, and glycoprotein epitopes involved in intracellular post-internalization entry steps are difficult for antibodies or antivirals to access. Therefore, defining viral factors essential for facilitating virus-cell surface attachment is crucial. For LASV, this will require characterizing both GP1-αDG and envelope-PSR interactions. For LASV attachment via αDG, we know that GP1 binds to the N terminal

mucin-like domain of αDG similarly to αDG's typical ligand laminin, but the αDG binding site on GP1 is not yet identified (40, 126).

Elucidating the viral factors required for LASV and EBOV PSR binding is complicated by the fact that these receptors interact with plasma membrane-derived viral envelope PS, rather than a virally-encoded and mutable protein like GP. Previous studies suggested that viral envelope PS can be altered by targeting host cell PS-distributing enzymes in the plasma membrane. They discovered that knocking down scramblases, which mediate cellular PS exposure, reduces PS exposure on EBOV-infected cells and EBOV envelopes (89, 90). However these studies propose differing underlying mechanisms, attributing EBOV-induced cell and virus PS exposure to either calcium signaling and scramblase TMEM16F (89) or apoptosis and scramblase XKR8 (90). Meanwhile, cell plasma membrane PS is also highly regulated by flippases; however, there are no studies thoroughly examining the relationship between flippases and viral envelope PS or virus replication in general.

To better understand and target LASV and EBOV entry, we aimed to 1) characterize the LASV αDG receptor binding site within GP1 using site-directed mutagenesis, 2) clarify specific cellular PS scramblases required for external EBOV envelope PS, and 3) investigate the role of cellular PS flippases in EBOV replication.

References

1. CDC. 2019. Lassa Fever. https://www.cdc.gov/vhf/lassa/. Accessed 10 October 2021.

2. Ficenec SC, Percak J, Arguello S, Bays A, Goba A, Gbakie M, Shaffer JG, Emmett SD, Schieffelin JS, Bausch D. 2020. Lassa Fever Induced Hearing Loss: The Neglected Disability of Hemorrhagic Fever. Int J Infect Dis 100:82-87.

3. Ezeomah C, Adoga A, Ihekweazu C, Paessler S, Cisneros I, Tomori O, Walker D. 2019. Sequelae of Lassa Fever: Postviral Cerebellar Ataxia. Open Forum Infect Dis 6:ofz512.

4. Hansen F, Jarvis MA, Feldmann H, Rosenke K. 2021. Lassa Virus Treatment Options. Microorganisms 9.

5. NIAID. NIAID Emerging Infectious Diseases/ Pathogens. https://www.niaid.nih.gov/research/emerging-infectious-diseases-pathogens. Accessed 10 October 2021.

6. Olayemi A, Fichet-Calvet E. 2020. Systematics, Ecology, and Host Switching: Attributes Affecting Emergence of the Lassa Virus in Rodents across Western Africa. Viruses 12.

7. Yun NE, Walker DH. 2012. Pathogenesis of Lassa fever. Viruses 4:2031-48.

8. Sevilla N, Kunz S, Holz A, Lewicki H, Homann D, Yamada H, Campbell KP, de La Torre JC, Oldstone MB. 2000. Immunosuppression and resultant viral persistence by specific viral targeting of dendritic cells. J Exp Med 192:1249-60.

9. Laguens RM, Chambo JG, Laguens RP. 1986. Splenic dendritic cells and Junin virus. Med Microbiol Immunol 175:187-9.

10. Baize S, Kaplon J, Faure C, Pannetier D, Georges-Courbot MC, Deubel V. 2004. Lassa virus infection of human dendritic cells and macrophages is productive but fails to activate cells. J Immunol 172:2861-9.

11. Baillet N, Reynard S, Perthame E, Hortion J, Journeaux A, Mateo M, Carnec X, Schaeffer J, Picard C, Barrot L, Barron S, Vallve A, Duthey A, Jacquot F, Boehringer C, Jouvion G, Pietrosemoli N, Legendre R, Dillies MA, Allan R, Legras-Lachuer C, Carbonnelle C, Raoul H, Baize S. 2021. Systemic viral spreading and defective host responses are associated with fatal Lassa fever in macaques. Commun Biol 4:27.

12. Loureiro ME, D'Antuono A, Lopez N. 2019. Virus(-)Host Interactions Involved in Lassa Virus Entry and Genome Replication. Pathogens 8.

13. Burri DJ, da Palma JR, Kunz S, Pasquato A. 2012. Envelope glycoprotein of arenaviruses. Viruses 4:2162-81.

14. White JM, Delos SE, Brecher M, Schornberg K. 2008. Structures and mechanisms of viral membrane fusion proteins: multiple variations on a common theme. Crit Rev Biochem Mol Biol 43:189-219.

15. Oppliger J, Torriani G, Herrador A, Kunz S. 2016. Lassa Virus Cell Entry via Dystroglycan Involves an Unusual Pathway of Macropinocytosis. J Virol 90:6412-29.

16. Shimojima M, Stroher U, Ebihara H, Feldmann H, Kawaoka Y. 2012. Identification of cell surface molecules involved in dystroglycan-independent Lassa virus cell entry. J Virol 86:2067-78.

17. Goncalves AR, Moraz ML, Pasquato A, Helenius A, Lozach PY, Kunz S. 2013. Role of DC-SIGN in Lassa virus entry into human dendritic cells. J Virol 87:11504-15.

18. Brouillette RB, Phillips EK, Patel R, Mahauad-Fernandez W, Moller-Tank S, Rogers KJ, Dillard JA, Cooney AL, Martinez-Sobrido L, Okeoma C, Maury W. 2018. TIM-1 Mediates Dystroglycan-Independent Entry of Lassa Virus. J Virol 92.

19. Fedeli C, Torriani G, Galan-Navarro C, Moraz ML, Moreno H, Gerold G, Kunz S. 2018. Axl Can Serve as Entry Factor for Lassa Virus Depending on the Functional Glycosylation of Dystroglycan. J Virol 92.

20. Fedeli C, Moreno H, Kunz S. 2020. The Role of Receptor Tyrosine Kinases in Lassa Virus Cell Entry. Viruses 12.

21. Jae LT, Raaben M, Herbert AS, Kuehne AI, Wirchnianski AS, Soh TK, Stubbs SH, Janssen H, Damme M, Saftig P, Whelan SP, Dye JM, Brummelkamp TR. 2014. Virus entry. Lassa virus entry requires a trigger-induced receptor switch. Science 344:1506-10.

22. Li S, Sun Z, Pryce R, Parsy ML, Fehling SK, Schlie K, Siebert CA, Garten W, Bowden TA, Strecker T, Huiskonen JT. 2016. Acidic pH-Induced Conformations and LAMP1 Binding of the Lassa Virus Glycoprotein Spike. PLoS Pathog 12:e1005418.

23. Cohen-Dvashi H, Israeli H, Shani O, Katz A, Diskin R. 2016. Role of LAMP1 Binding and pH Sensing by the Spike Complex of Lassa Virus. J Virol 90:10329-10338.

24. Hulseberg CE, Feneant L, Szymanska KM, White JM. 2018. Lamp1 Increases the Efficiency of Lassa Virus Infection by Promoting Fusion in Less Acidic Endosomal Compartments. mBio 9.

25. Cohen-Dvashi H, Cohen N, Israeli H, Diskin R. 2015. Molecular Mechanism for LAMP1 Recognition by Lassa Virus. J Virol 89:7584-92.

26. Bulow U, Govindan R, Munro JB. 2020. Acidic pH Triggers Lipid Mixing Mediated by Lassa Virus GP. Viruses 12.

27. Hastie KM, Igonet S, Sullivan BM, Legrand P, Zandonatti MA, Robinson JE, Garry RF, Rey FA, Oldstone MB, Saphire EO. 2016. Crystal structure of the prefusion surface glycoprotein of the prototypic arenavirus LCMV. Nat Struct Mol Biol 23:513-21.

28. Igonet S, Vaney MC, Vonrhein C, Bricogne G, Stura EA, Hengartner H, Eschli B, Rey FA. 2011. X-ray structure of the arenavirus glycoprotein GP2 in its postfusion hairpin conformation. Proc Natl Acad Sci U S A 108:19967-72.

29. Eschli B, Quirin K, Wepf A, Weber J, Zinkernagel R, Hengartner H. 2006. Identification of an N-terminal trimeric coiled-coil core within arenavirus glycoprotein 2 permits assignment to class I viral fusion proteins. J Virol 80:5897-907.

30. Hass M, Golnitz U, Muller S, Becker-Ziaja B, Gunther S. 2004. Replicon system for Lassa virus. J Virol 78:13793-803.

31. Lee KJ, Novella IS, Teng MN, Oldstone MB, de La Torre JC. 2000. NP and L proteins of lymphocytic choriomeningitis virus (LCMV) are sufficient for efficient transcription and replication of LCMV genomic RNA analogs. J Virol 74:3470-7.

32. Lopez N, Jacamo R, Franze-Fernandez MT. 2001. Transcription and RNA replication of tacaribe virus genome and antigenome analogs require N and L proteins: Z protein is an inhibitor of these processes. J Virol 75:12241-51.

33. Urata S, Yasuda J. 2012. Molecular mechanism of arenavirus assembly and budding. Viruses 4:2049-79.

34. Barresi R, Campbell KP. 2006. Dystroglycan: from biosynthesis to pathogenesis of human disease. J Cell Sci 119:199-207.

35. Spiropoulou CF, Kunz S, Rollin PE, Campbell KP, Oldstone MB. 2002. New World arenavirus clade C, but not clade A and B viruses, utilizes alpha-dystroglycan as its major receptor. J Virol 76:5140-6.

36. Kanagawa M, Saito F, Kunz S, Yoshida-Moriguchi T, Barresi R, Kobayashi YM, Muschler J, Dumanski JP, Michele DE, Oldstone MB, Campbell KP. 2004. Molecular recognition by LARGE is essential for expression of functional dystroglycan. Cell 117:953-64.

37. Goddeeris MM, Wu B, Venzke D, Yoshida-Moriguchi T, Saito F, Matsumura K, Moore SA, Campbell KP. 2013. LARGE glycans on dystroglycan function as a tunable matrix scaffold to prevent dystrophy. Nature 503:136-40.

38. Joseph S, Campbell KP. 2021. Lassa Fever Virus Binds Matriglycan-A Polymer of Alternating Xylose and Glucuronate-On alpha-Dystroglycan. Viruses 13.

39. Walker DH, McCormick JB, Johnson KM, Webb PA, Komba-Kono G, Elliott LH, Gardner JJ. 1982. Pathologic and virologic study of fatal Lassa fever in man. Am J Pathol 107:349-56.

40. Kunz S, Rojek JM, Perez M, Spiropoulou CF, Oldstone MB. 2005. Characterization of the interaction of lassa fever virus with its cellular receptor alpha-dystroglycan. J Virol 79:5979-87.

41. Imperiali M, Sporri R, Hewitt J, Oxenius A. 2008. Post-translational modification of {alpha}-dystroglycan is not critical for lymphocytic choriomeningitis virus receptor function in vivo. J Gen Virol 89:2713-2722.

42. Sullivan BM, Welch MJ, Lemke G, Oldstone MB. 2013. Is the TAM receptor Axl a receptor for lymphocytic choriomeningitis virus? J Virol 87:4071-4.

43. Vetter P, Kaiser L, Schibler M, Ciglenecki I, Bausch DG. 2016. Sequelae of Ebola virus disease: the emergency within the emergency. Lancet Infect Dis 16:e82-e91.

44. Schindell BG, Webb AL, Kindrachuk J. 2018. Persistence and Sexual Transmission of Filoviruses. Viruses 10.

45. Jacob ST, Crozier I, Fischer WA, 2nd, Hewlett A, Kraft CS, Vega MA, Soka MJ, Wahl V, Griffiths A, Bollinger L, Kuhn JH. 2020. Ebola virus disease. Nat Rev Dis Primers 6:13.

46. Wolfe DN, Sabourin CL, Merchlinsky MJ, Florence WC, Wolfraim LA, Taylor KL, Ward LA. 2021. Selection of Filovirus Isolates for Vaccine Development Programs. Vaccines (Basel) 9.

47. Di Paola N, Sanchez-Lockhart M, Zeng X, Kuhn JH, Palacios G. 2020. Viral genomics in Ebola virus research. Nat Rev Microbiol 18:365-378.

48. Koch LK, Cunze S, Kochmann J, Klimpel S. 2020. Bats as putative Zaire ebolavirus reservoir hosts and their habitat suitability in Africa. Sci Rep 10:14268.

49. Brainard J, Hooper L, Pond K, Edmunds K, Hunter PR. 2016. Risk factors for transmission of Ebola or Marburg virus disease: a systematic review and meta-analysis. Int J Epidemiol 45:102-16.

50. Geisbert TW, Hensley LE, Larsen T, Young HA, Reed DS, Geisbert JB, Scott DP, Kagan E, Jahrling PB, Davis KJ. 2003. Pathogenesis of Ebola hemorrhagic fever in cynomolgus macaques: evidence that dendritic cells are early and sustained targets of infection. Am J Pathol 163:2347-70.

51. Zhu W, Banadyga L, Emeterio K, Wong G, Qiu X. 2019. The Roles of Ebola Virus Soluble Glycoprotein in Replication, Pathogenesis, and Countermeasure Development. Viruses 11.

52. Davey RA, Shtanko O, Anantpadma M, Sakurai Y, Chandran K, Maury W. 2017. Mechanisms of Filovirus Entry. Curr Top Microbiol Immunol 411:323-352.

53. Rasmussen AL. 2018. Host Factors Involved in Ebola Virus Replication. Curr Top Microbiol Immunol 419:113-150.

54. O'Hearn A, Wang M, Cheng H, Lear-Rooney CM, Koning K, Rumschlag-Booms E, Varhegyi E, Olinger G, Rong L. 2015. Role of EXT1 and Glycosaminoglycans in the Early Stage of Filovirus Entry. J Virol 89:5441-9.

55. Baribaud F, Doms RW, Pohlmann S. 2002. The role of DC-SIGN and DC-SIGNR in HIV and Ebola virus infection: can potential therapeutics block virus transmission and dissemination? Expert Opin Ther Targets 6:423-31.

56. Alvarez CP, Lasala F, Carrillo J, Muniz O, Corbi AL, Delgado R. 2002. C-type lectins DC-SIGN and L-SIGN mediate cellular entry by Ebola virus in cis and in trans. J Virol 76:6841-4.

57. Takada A, Fujioka K, Tsuiji M, Morikawa A, Higashi N, Ebihara H, Kobasa D, Feldmann H, Irimura T, Kawaoka Y. 2004. Human macrophage C-type lectin specific for galactose and N-acetylgalactosamine promotes filovirus entry. J Virol 78:2943-7.

58. Pipirou Z, Powlesland AS, Steffen I, Pohlmann S, Taylor ME, Drickamer K. 2011. Mouse LSECtin as a model for a human Ebola virus receptor. Glycobiology 21:806-12.

59. Jemielity S, Wang JJ, Chan YK, Ahmed AA, Li W, Monahan S, Bu X, Farzan M, Freeman GJ, Umetsu DT, Dekruyff RH, Choe H. 2013. TIM-family proteins promote infection of multiple enveloped viruses through virion-associated phosphatidylserine. PLoS Pathog 9:e1003232.

60. Moller-Tank S, Kondratowicz AS, Davey RA, Rennert PD, Maury W. 2013. Role of the phosphatidylserine receptor TIM-1 in enveloped-virus entry. J Virol 87:8327-41.

61. Kondratowicz AS, Lennemann NJ, Sinn PL, Davey RA, Hunt CL, Moller-Tank S, Meyerholz DK, Rennert P, Mullins RF, Brindley M, Sandersfeld LM, Quinn K, Weller M, McCray PB, Jr., Chiorini J, Maury W. 2011. T-cell immunoglobulin and mucin domain 1 (TIM-1) is a receptor for Zaire Ebolavirus and Lake Victoria Marburgvirus. Proc Natl Acad Sci U S A 108:8426-31.

62. Shimojima M, Takada A, Ebihara H, Neumann G, Fujioka K, Irimura T, Jones S, Feldmann H, Kawaoka Y. 2006. Tyro3 family-mediated cell entry of Ebola and Marburg viruses. J Virol 80:10109-16.

63. Shimojima M, Ikeda Y, Kawaoka Y. 2007. The mechanism of Axl-mediated Ebola virus infection. J Infect Dis 196 Suppl 2:S259-63.

64. Brindley MA, Hunt CL, Kondratowicz AS, Bowman J, Sinn PL, McCray PB, Jr., Quinn K, Weller ML, Chiorini JA, Maury W. 2011. Tyrosine kinase receptor Axl

enhances entry of Zaire ebolavirus without direct interactions with the viral glycoprotein. Virology 415:83-94.

65. Bhattacharyya S, Zagorska A, Lew ED, Shrestha B, Rothlin CV, Naughton J, Diamond MS, Lemke G, Young JA. 2013. Enveloped viruses disable innate immune responses in dendritic cells by direct activation of TAM receptors. Cell Host Microbe 14:136-47.

66. Younan P, Iampietro M, Nishida A, Ramanathan P, Santos RI, Dutta M, Lubaki NM, Koup RA, Katze MG, Bukreyev A. 2017. Ebola Virus Binding to Tim-1 on T Lymphocytes Induces a Cytokine Storm. mBio 8.

67. Brunton B, Rogers K, Phillips EK, Brouillette RB, Bouls R, Butler NS, Maury W. 2019. TIM-1 serves as a receptor for Ebola virus in vivo, enhancing viremia and pathogenesis. PLoS Negl Trop Dis 13:e0006983.

68. Moller-Tank S, Maury W. 2014. Phosphatidylserine receptors: enhancers of enveloped virus entry and infection. Virology 468-470:565-80.

69. Meertens L, Carnec X, Lecoin MP, Ramdasi R, Guivel-Benhassine F, Lew E, Lemke G, Schwartz O, Amara A. 2012. The TIM and TAM families of phosphatidylserine receptors mediate dengue virus entry. Cell Host Microbe 12:544-57.

70. Carnec X, Meertens L, Dejarnac O, Perera-Lecoin M, Hafirassou ML, Kitaura J, Ramdasi R, Schwartz O, Amara A. 2016. The Phosphatidylserine and Phosphatidylethanolamine Receptor CD300a Binds Dengue Virus and Enhances Infection. J Virol 90:92-102.

71. Dejarnac O, Hafirassou ML, Chazal M, Versapuech M, Gaillard J, Perera-Lecoin M, Umana-Diaz C, Bonnet-Madin L, Carnec X, Tinevez JY, Delaugerre C, Schwartz O, Roingeard P, Jouvenet N, Berlioz-Torrent C, Meertens L, Amara A. 2018. TIM-1 Ubiquitination Mediates Dengue Virus Entry. Cell Rep 23:1779-1793.

72. Mercer J, Helenius A. 2008. Vaccinia virus uses macropinocytosis and apoptotic mimicry to enter host cells. Science 320:531-5.

73. Morizono K, Xie Y, Olafsen T, Lee B, Dasgupta A, Wu AM, Chen IS. 2011. The soluble serum protein Gas6 bridges virion envelope phosphatidylserine to the TAM receptor tyrosine kinase Axl to mediate viral entry. Cell Host Microbe 9:286-98.

74. Wei X, Li R, Qiao S, Chen XX, Xing G, Zhang G. 2020. Porcine Reproductive and Respiratory Syndrome Virus Utilizes Viral Apoptotic Mimicry as an Alternative Pathway To Infect Host Cells. J Virol 94.

75. Meertens L, Labeau A, Dejarnac O, Cipriani S, Sinigaglia L, Bonnet-Madin L, Le Charpentier T, Hafirassou ML, Zamborlini A, Cao-Lormeau VM, Coulpier M, Misse D, Jouvenet N, Tabibiazar R, Gressens P, Schwartz O, Amara A. 2017. Axl Mediates ZIKA Virus Entry in Human Glial Cells and Modulates Innate Immune Responses. Cell Rep 18:324-333.

76. Li M, Ablan SD, Miao C, Zheng YM, Fuller MS, Rennert PD, Maury W, Johnson MC, Freed EO, Liu SL. 2014. TIM-family proteins inhibit HIV-1 release. Proc Natl Acad Sci U S A 111:E3699-707.

77. Mayor J, Torriani G, Rothenberger S, Engler O. 2020. T-cell immunoglobulin and mucin (TIM) contributes to the infection of human airway epithelial cells by pseudotype viruses containing Hantaan virus glycoproteins. Virology 543:54-62.

78. Richard AS, Zhang A, Park SJ, Farzan M, Zong M, Choe H. 2015. Virion-associated phosphatidylethanolamine promotes TIM1-mediated infection by Ebola, dengue, and West Nile viruses. Proc Natl Acad Sci U S A 112:14682-7.

79. Morizono K, Chen IS. 2014. Role of phosphatidylserine receptors in enveloped virus infection. J Virol 88:4275-90.

80. Bohan D, Ert HV, Ruggio N, Rogers KJ, Badreddine M, Aguilar Briseno JA, Rojas Chavez RA, Gao B, Stokowy T, Christakou E, Micklem D, Gausdal G, Haim H, Minna J, Lorens JB, Maury W. 2021. Phosphatidylserine Receptors Enhance SARS-CoV-2 Infection: AXL as a Therapeutic Target for COVID-19. bioRxiv doi:10.1101/2021.06.15.448419.

81. Chen YH, Du W, Hagemeijer MC, Takvorian PM, Pau C, Cali A, Brantner CA, Stempinski ES, Connelly PS, Ma HC, Jiang P, Wimmer E, Altan-Bonnet G, Altan-Bonnet N. 2015. Phosphatidylserine vesicles enable efficient en bloc transmission of enteroviruses. Cell 160:619-630.

82. Costafreda MI, Abbasi A, Lu H, Kaplan G. 2020. Exosome mimicry by a HAVCR1-NPC1 pathway of endosomal fusion mediates hepatitis A virus infection. Nat Microbiol 5:1096-1106.

83. Bohan D, Maury W. 2021. Enveloped RNA virus utilization of phosphatidylserine receptors: Advantages of exploiting a conserved, widely available mechanism of entry. PLoS Pathog 17:e1009899.

84. Birge RB, Boeltz S, Kumar S, Carlson J, Wanderley J, Calianese D, Barcinski M, Brekken RA, Huang X, Hutchins JT, Freimark B, Empig C, Mercer J, Schroit AJ, Schett G, Herrmann M. 2016. Phosphatidylserine is a global immunosuppressive signal in efferocytosis, infectious disease, and cancer. Cell Death Differ 23:962-78.

85. Callahan MK, Popernack PM, Tsutsui S, Truong L, Schlegel RA, Henderson AJ. 2003. Phosphatidylserine on HIV envelope is a cofactor for infection of monocytic cells. J Immunol 170:4840-5.

86. Sutherland MR, Raynor CM, Leenknegt H, Wright JF, Pryzdial EL. 1997. Coagulation initiated on herpesviruses. Proc Natl Acad Sci U S A 94:13510-4.

87. Pryzdial EL, Wright JF. 1994. Prothrombinase assembly on an enveloped virus: evidence that the cytomegalovirus surface contains procoagulant phospholipid. Blood 84:3749-57.

88. Soares MM, King SW, Thorpe PE. 2008. Targeting inside-out phosphatidylserine as a therapeutic strategy for viral diseases. Nat Med 14:1357-62.

89. Younan P, Iampietro M, Santos RI, Ramanathan P, Popov VL, Bukreyev A. 2018. Role of Transmembrane Protein 16F in the Incorporation of Phosphatidylserine Into Budding Ebola Virus Virions. J Infect Dis 218:S335-S345.

90. Nanbo A, Maruyama J, Imai M, Ujie M, Fujioka Y, Nishide S, Takada A, Ohba Y, Kawaoka Y. 2018. Ebola virus requires a host scramblase for externalization of phosphatidylserine on the surface of viral particles. PLoS Pathog 14:e1006848.

91. Leventis PA, Grinstein S. 2010. The distribution and function of phosphatidylserine in cellular membranes. Annu Rev Biophys 39:407-27.

92. Kay JG, Fairn GD. 2019. Distribution, dynamics and functional roles of phosphatidylserine within the cell. Cell Commun Signal 17:126.

93. van Meer G, Voelker DR, Feigenson GW. 2008. Membrane lipids: where they are and how they behave. Nat Rev Mol Cell Biol 9:112-24.

94. Bevers EM, Williamson PL. 2016. Getting to the Outer Leaflet: Physiology of Phosphatidylserine Exposure at the Plasma Membrane. Physiol Rev 96:605-45.

95. Bai J, Pagano RE. 1997. Measurement of spontaneous transfer and transbilayer movement of BODIPY-labeled lipids in lipid vesicles. Biochemistry 36:8840-8.

96. Pomorski TG, Menon AK. 2016. Lipid somersaults: Uncovering the mechanisms of protein-mediated lipid flipping. Prog Lipid Res 64:69-84.

97. Kalienkova V, Clerico Mosina V, Paulino C. 2021. The Groovy TMEM16 Family: Molecular Mechanisms of Lipid Scrambling and Ion Conduction. J Mol Biol doi:10.1016/j.jmb.2021.166941:166941.

98. Nagata S, Segawa K. 2021. Sensing and clearance of apoptotic cells. Curr Opin Immunol 68:1-8.

99. Hankins HM, Baldridge RD, Xu P, Graham TR. 2015. Role of flippases, scramblases and transfer proteins in phosphatidylserine subcellular distribution. Traffic 16:35-47.

100. Andersen JP, Vestergaard AL, Mikkelsen SA, Mogensen LS, Chalat M, Molday RS. 2016. P4-ATPases as Phospholipid Flippases-Structure, Function, and Enigmas. Front Physiol 7:275.

101. Segawa K, Kurata S, Nagata S. 2016. Human Type IV P-type ATPases That Work as Plasma Membrane Phospholipid Flippases and Their Regulation by Caspase and Calcium. J Biol Chem 291:762-72.

102. Segawa K, Kurata S, Nagata S. 2018. The CDC50A extracellular domain is required for forming a functional complex with and chaperoning phospholipid flippases to the plasma membrane. J Biol Chem 293:2172-2182.

103. Nakanishi H, Irie K, Segawa K, Hasegawa K, Fujiyoshi Y, Nagata S, Abe K. 2020. Crystal structure of a human plasma membrane phospholipid flippase. J Biol Chem 295:10180-10194.

104. Baggen J, Persoons L, Vanstreels E, Jansen S, Van Looveren D, Boeckx B, Geudens V, De Man J, Jochmans D, Wauters J, Wauters E, Vanaudenaerde BM, Lambrechts D, Neyts J, Dallmeier K, Thibaut HJ, Jacquemyn M, Maes P, Daelemans D. 2021. Genome-wide CRISPR screening identifies TMEM106B as a proviral host factor for SARS-CoV-2. Nat Genet 53:435-444.

105. Raaben M, Jae LT, Herbert AS, Kuehne AI, Stubbs SH, Chou YY, Blomen VA, Kirchhausen T, Dye JM, Brummelkamp TR, Whelan SP. 2017. NRP2 and CD63 Are Host Factors for Lujo Virus Cell Entry. Cell Host Microbe 22:688-696 e5.

106. Nagata S, Suzuki J, Segawa K, Fujii T. 2016. Exposure of phosphatidylserine on the cell surface. Cell Death Differ 23:952-61.

107. Suzuki J, Umeda M, Sims PJ, Nagata S. 2010. Calcium-dependent phospholipid scrambling by TMEM16F. Nature 468:834-8.

108. Suzuki J, Denning DP, Imanishi E, Horvitz HR, Nagata S. 2013. Xk-related protein 8 and CED-8 promote phosphatidylserine exposure in apoptotic cells. Science 341:403-6.

109. Suzuki J, Fujii T, Imao T, Ishihara K, Kuba H, Nagata S. 2013. Calcium-dependent phospholipid scramblase activity of TMEM16 protein family members. J Biol Chem 288:13305-16.

110. Pedemonte N, Galietta LJ. 2014. Structure and function of TMEM16 proteins (anoctamins). Physiol Rev 94:419-59.

111. Fujii T, Sakata A, Nishimura S, Eto K, Nagata S. 2015. TMEM16F is required for phosphatidylserine exposure and microparticle release in activated mouse platelets. Proc Natl Acad Sci U S A 112:12800-5.

112. Brooks MB, Catalfamo JL, MacNguyen R, Tim D, Fancher S, McCardle JA. 2015. A TMEM16F point mutation causes an absence of canine platelet TMEM16F and ineffective activation and death-induced phospholipid scrambling. J Thromb Haemost 13:2240-52.

113. Ishihara K, Suzuki J, Nagata S. 2016. Role of Ca(2+) in the Stability and Function of TMEM16F and 16K. Biochemistry 55:3180-8.

114. Gyobu S, Ishihara K, Suzuki J, Segawa K, Nagata S. 2017. Characterization of the scrambling domain of the TMEM16 family. Proc Natl Acad Sci U S A 114:6274-6279.

115. Bethel NP, Grabe M. 2016. Atomistic insight into lipid translocation by a TMEM16 scramblase. Proc Natl Acad Sci U S A 113:14049-14054.

116. Castoldi E, Collins PW, Williamson PL, Bevers EM. 2011. Compound heterozygosity for 2 novel TMEM16F mutations in a patient with Scott syndrome. Blood 117:4399-400.

117. Ehlen HW, Chinenkova M, Moser M, Munter HM, Krause Y, Gross S, Brachvogel B, Wuelling M, Kornak U, Vortkamp A. 2013. Inactivation of anoctamin-6/Tmem16f, a regulator of phosphatidylserine scrambling in osteoblasts, leads to decreased mineral deposition in skeletal tissues. J Bone Miner Res 28:246-59.

118. Zaitseva E, Zaitsev E, Melikov K, Arakelyan A, Marin M, Villasmil R, Margolis LB, Melikyan GB, Chernomordik LV. 2017. Fusion Stage of HIV-1 Entry Depends on Virus-Induced Cell Surface Exposure of Phosphatidylserine. Cell Host Microbe 22:99-110 e7.

119. Braga L, Ali H, Secco I, Chiavacci E, Neves G, Goldhill D, Penn R, Jimenez-Guardeno JM, Ortega-Prieto AM, Bussani R, Cannata A, Rizzari G, Collesi C, Schneider E, Arosio D, Shah AM, Barclay WS, Malim MH, Burrone J, Giacca M. 2021. Drugs that inhibit TMEM16 proteins block SARS-CoV-2 spike-induced syncytia. Nature 594:88-93.

120. Chua BA, Ngo JA, Situ K, Morizono K. 2019. Roles of phosphatidylserine exposed on the viral envelope and cell membrane in HIV-1 replication. Cell Commun Signal 17:132.

121. Suzuki J, Imanishi E, Nagata S. 2014. Exposure of phosphatidylserine by Xk-related protein family members during apoptosis. J Biol Chem 289:30257-67.

122. Suzuki J, Imanishi E, Nagata S. 2016. Xkr8 phospholipid scrambling complex in apoptotic phosphatidylserine exposure. Proc Natl Acad Sci U S A 113:9509-14.

123. Nanbo A, Kawaoka Y. 2019. Molecular Mechanism of Externalization of Phosphatidylserine on the Surface of Ebola Virus Particles. DNA Cell Biol 38:115-120.

124. Sakuragi T, Kosako H, Nagata S. 2019. Phosphorylation-mediated activation of mouse Xkr8 scramblase for phosphatidylserine exposure. Proc Natl Acad Sci U S A 116:2907-2912.

125. Segawa K, Kurata S, Yanagihashi Y, Brummelkamp TR, Matsuda F, Nagata S. 2014. Caspase-mediated cleavage of phospholipid flippase for apoptotic phosphatidylserine exposure. Science 344:1164-8.

126. Kunz S, Rojek JM, Kanagawa M, Spiropoulou CF, Barresi R, Campbell KP, Oldstone MB. 2005. Posttranslational modification of alpha-dystroglycan, the cellular receptor for arenaviruses, by the glycosyltransferase LARGE is critical for virus binding. J Virol 79:14282-96.

CHAPTER 3

MUTATIONAL ANALYSIS OF LASSA VIRUS GLYCOPROTEIN HIGHLGHTS REGIONS REQUIRED FOR ALPHA-DYSTROGLYCAN UTILIZATION[1]

[1]Acciani M*, Alston JT*, Zhao G, et al. Mutational Analysis of Lassa Virus Glycoprotein Highlights Regions Required for Alpha-Dystroglycan Utilization. *J Virol.* 2017;91(18):e00574-17. Published 2017 Aug 24. doi:10.1128/JVI.00574-17. Reprinted here with permission of the publisher. *Authors contributed equally to this work

Abstract

Lassa virus (LASV) is an enveloped RNA virus endemic to West Africa and responsible for severe cases of hemorrhagic fever. Virus entry is mediated by the glycoprotein complex consisting of a stable signal peptide, a receptor-binding subunit GP1, and a viral-host membrane fusion subunit GP2. Several cellular receptors can interact with the GP1 subunit and mediate viral entry, including alpha-dystroglycan (αDG) and lysosomal associated membrane protein 1 (LAMP1). In order to define the regions within GP1 that interact with the cellular receptors, we implemented insertional mutagenesis, carbohydrate shielding, and alanine scanning mutagenesis. Eighty GP constructs were engineered and evaluated for GP1-GP2 processing, surface expression, and the ability to mediate cell-to-cell fusion after low-pH exposure. To examine virus-to-cell entry, 49 constructs were incorporated onto VSV pseudo-particles and transduction efficiencies were monitored in HAP1 and HAP1-ΔDAG1 cells that differentially produce the αDG cell surface receptor. Seven constructs retained efficient transduction in HAP1-ΔDAG1 cells, yet poorly transduced HAP1 cells, suggesting they are involved in αDG utilization. Residues H141, N146, F147, and Y150 cluster at the predicted central core of the trimeric interface, and are important for GP-αDG interaction. Additionally, H92A-H93A, 150HA, 172HA, and 230HA displayed reduced transduction in both HAP1 and HAP1-ΔDAG1 cells, despite efficient cell-to-cell fusion activity. These mutations may interfere with interactions with the endosomal receptor LAMP1 or interfere at another stage in entry that is in common in both cell lines. Insight gained from these data can aid in the development of more effective entry inhibitors by blocking receptor interactions.

Importance

Countries with endemic Lassa virus such as Nigeria, Sierra Leone, Guinea and Liberia usually experience a seasonal outbreak of the virus from December to March. Currently, there is neither a preventative vaccine nor therapeutic available to effectively treat severe Lassa fever. One way to thwart virus infection is to inhibit interaction with cellular receptors. It is known that the GP1 subunit of the Lassa glycoprotein complex plays a critical role in receptor recognition. Our results highlight a region within the Lassa virus GP1 protein that interacts with the cellular receptor alpha-dystroglycan. This information may be used for future development of new Lassa virus antivirals.

Introduction

Lassa fever is a hemorrhagic disease caused by an Old World arenavirus known as Lassa virus (LASV). The virus was first isolated in Nigeria in 1969 and is currently endemic in West Africa (1). Serological studies suggest hundreds of thousands of people are infected each year (2). While most infections are mild or asymptomatic, 15-20% of cases require hospitalization and result in approximately 5000 deaths annually (3-5). The rodent host for LASV is the multimammate rat, *Mastomys natalenis* (6). Recently, the virus has been isolated from *Hylomyscus pamfi* and *Mastomys erythroleucus,* potentially increasing its geographic range (7). Human exposure occurs through direct contact with the infected rodents, rodent excrement, or close contact with infected patients (8). Due to the high morbidity and mortality associated with Lassa hemorrhagic fever, LASV is classified as a category A pathogen (9).

Lassa virus is an enveloped ambisense RNA virus with a bi-segmented genome. Viral particles are covered in mature glycoprotein (GP) trimeric spikes, which mediate

viral entry. Like other class 1 viral fusion proteins, the envelope glycoprotein precursor (GPC) is translated as a single polypeptide and is proteolytically cleaved into three subunits. Processing occurs first in the ER by a cellular signal peptidase. GPC is then trafficked to the cis-Golgi and processed by cellular proprotein convertase subtilisin kexin isozyme-1/site-1 protease (SKI-1/S1P) to produce a non-covalent stable signal peptide SSP/GP1/GP2 hetero-trimer (Fig 1A-B) (10-13). Unlike other class I fusion proteins, the relatively long signal peptide of GPC is not degraded; it serves a chaperone-like function necessary for the correct trafficking and processing of GP (14-16). SSP interacts with the cytoplasmic domain of GP2 and is involved in pH sensing (17-19). GP1 is responsible for binding to cellular receptors (20, 21), while GP2 mediates membrane fusion during viral entry (22-24).

Cellular entry of LASV is a multistep process involving multiple GP1-receptor interactions. First, GP1 interacts with a cell surface receptor on the plasma membrane, mainly alpha-dystroglycan (αDG) (21). Additional surface receptors can mediate LASV entry in the absence of αDG, including heparin sulfate, DC-SIGN and TAM family members (20, 25, 26). This initial GP1-receptor interaction induces viral internalization through a clathrin, caveolin, and dynamin independent process (20, 27, 28). Once within the low-pH environment of the endo-lysosomal compartment, GP undergoes conformational changes that reduce its affinity for αDG and increase its affinity to a second receptor, lysosomal associated membrane protein 1 (LAMP1) (29, 30). Engagement of LAMP1 by LASV GP1 is hypothesized to lower the activation energy needed to mediate GP2 conformational changes that fuse the viral and cellular membranes, completing the entry pathway (31).

Previous studies have provided new structural information for both the pre-fusion conformation and pH-induced changes in the LASV glycoprotein. Recently, the trimeric pre-fusion GP1/GP2 crystal of LASV was solved (32). This structure provides novel insight into the LASV GP complex including trimer organization, glycosylation, and potential receptor binding sites. The LASV GP1 monomeric protein was previously crystalized under low-pH conditions (pH 5) (33). The low-pH purified protein was unable to interact with αDG, but interacted with LAMP1, suggesting that the crystal structure resembles GP1 in the lysosome (33). Comparison of the pre-fusion GP1 crystal (isolated at pH 8) and the pH 5 GP1 crystal structure highlights several low pH-induced conformational changes required for LAMP-1 interactions (32).

In addition to the crystallization studies, a cryo-electron tomography (cryo-ET) study was able to construct three-dimensional structures of LASV GP trimers under increasingly acidic pH conditions (pH 7, 5, and 3) (31). Tomographic reconstructions suggest the GP1 subunit undergoes conformational changes at pH 5, opening a putative LAMP1 binding crevice at the GP1 trimeric interface (31, 33). Pseudoatomic models fit both pre-fusion GP1/GP2 and low-pH GP1 crystal structures into the low resolution cryo-ET densities, providing three-dimensional models of GP trimer organization (22, 31-33).

LASV entry is most efficient when GP1 interacts with αDG and LAMP1. While the GP1 binding interface has been mapped in both αDG and LAMP1, the corresponding receptor-binding sites in GP1 have yet to be elucidated. Utilizing the new crystal structure as a model, we used carbohydrate shielding, insertional mutagenesis, and alanine scanning mutagenesis to identify regions within GP1 important for receptor interactions (Fig 1D).

Results

With the overarching goal of understanding the functional and spatial organization of the arenavirus pre-fusion glycoprotein structure, we utilized the trimeric GP pre-fusion crystal structure (32) to identify residues involved in receptor interactions.

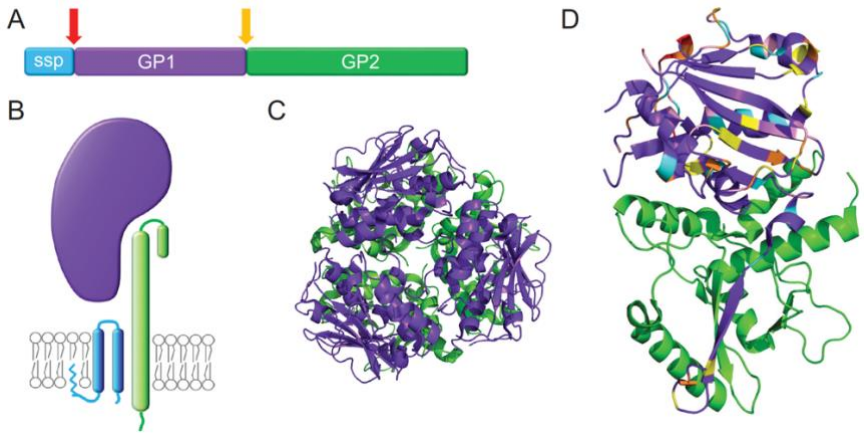

Fig 1. The subunits and structure of the Lassa virus glycoprotein complex. (A) The LASV glycoprotein complex consists of the membrane-integrated stable signal peptide (SSP) (blue), GP1 subunit (purple) and the non-covalently attached GP2 subunit (green). The GPC is cleaved by signal peptidase (red arrow) and SKI-1/S1P (yellow arrow) during protein processing. (B) Cartoon of the SSP, GP1 and GP2 heterotrimer complex in the lipid bilayer. (C) Trimeric LASV GP1-GP2 crystal structure, top down view, GP1 is in purple and GP2 in green (PDB 5vk2) (32). (D) The LASV GP1-GP2 crystal structure, side view, (PDB 5vk2) The engineered GP1 constructs are color-coded as follows: glycosylation site removals and additions (pink); HA-tagged sites (orange), alanine scanning of charged residues (yellow), alanine scanning of hydrophobic residues (blue), additional targeted residues (red). Note many of the targeted residues were found in regions of the structure that did not crystalize. All structures were rendered with PyMol.

Function of GPC N-Linked Glycans. Arenavirus GP N-linked glycans play significant biochemical roles in virus-cell interactions (34, 35). Previous studies found that specific N-linked glycans in LCMV GP1 were necessary for GP trafficking, fusion activity, and infectivity (34). LASV GP1 contains seven conserved N-linked glycosylation sites. Removing glycans at positions 81, 91, 101, and 121 was previously shown to inhibit GPC processing into GP1 and GP2 (35), although receptor binding and

fusion activity were not evaluated. We reproduced the seven N-glycan mutants by changing glycosylation site motifs from N-X-S/T to N-X-A. To examine the level of processed GP on the cell surface, surface proteins were biotinylated, concentrated using streptavidin sepharose beads, and subjected to immunoblot analysis (Fig 2A). All mutated GP's migrated faster than parental GP, confirming that all seven sites are glycosylated. We similarly found that removing the N-linked sites at T81 and S91 resulted in GPC processing defects (Fig 2A and C). However, we found the remaining five N-glycan mutations result in detectable levels of GP1-GP2 processing, including T101 and S121. Our use of a codon optimized expression construct and examining surface material 36 hours after transfection, rather than 24, may have enabled T101A and S121A to reach a detectable steady state levels of processed GP1-GP2 at the cell surface (35).

To determine if the constructs lacking N-glycans produce functional GP, we determined if they could produce syncytia, or multinucleated cells, in a cell-to-cell based fusion assay. Incubating LASV GP transfected cells with a low-pH buffer results in efficient GP activation and robust syncytia formation (Fig 2B). By comparing the extent of syncytium formation between mutant and parental GP, we can determine the fusion efficiency of each mutant. The fusion activity of the N-glycan mutants closely correlated with the cleavage efficiency (Fig 2C), suggesting the glycans are not required for productive cell-to-cell fusion.

Cell-to-cell fusion assays do not completely recapitulate the process that occurs when a viral particle fuses with an endosomal membrane. Virus-to-cell entry requires the viral glycoprotein to facilitate interactions with cellular receptors to initiate endocytosis.

Once trafficking to the proper cellular compartment occurs, LASV virus must undergo a receptor switch in the endo-lysosome before membrane fusion. In order to determine if the GP1 constructs can mediate viral entry, VSV pseudotyped particles were produced containing LASV GP on their surface. Particle transduction was monitored in two haploid cell lines, HAP1 and HAP1-ΔDAG1. LASV entry into HAP1 cells and HAP1-ΔDAG1, a cell line deficient in αDG, has been thoroughly documented by recent genetic screens (20, 36). Gene-trap screening of HAP1 cells re-confirmed LASV GP's interaction with properly glycosylated αDG significantly enhances cell entry (36). A second gene-trap screen in HAP1-ΔDAG1 cells identified an additional, lysosomal receptor, LAMP1 (20). Because efficient HAP1 entry of LASV occurs through αDG interactions, and HAP1-ΔDAG1 cell entry occurs through other cell surface receptors, such as heparin sulfate receptors (20), we propose that constructs exclusively demonstrating reduced transduction efficiency into HAP1 cells are inefficiently engaging αDG. In order to demonstrate the entry enhancement by αDG, we added the same volume of pseudotyped particles coated with LASV GP on both cell lines (Fig 2D). LASV GP entry into HAP1 cells produced 8.4 ± 0.83 times more GFP positive cells than the same volume of particles added to HAP1-ΔDAG1 cells. To compensate for the decreased entry into HAP1-ΔDAG1 cells, we increased the volume of particles used to transduce this cell type. When examining the transduction efficiencies, each mutant was compared to parental GP in each cell type. Therefor specific defects in HAP1 cell entry would highlight mutations that facilitated viral uptake through αDG interactions.

Because GP can only fuse if GP1-GP2 processing occurs, we examined transduction efficiency for constructs with at least 50% cleavage efficiency. Five

glycosylation removal GP1 constructs were examined in transduction assays, T101A, S111A, S121A, S169A and T226A. All five constructs efficiently transduced both cell types, suggesting GP missing a single N-glycan retains cell entry (Fig 2E).

Engineering N-linked glycosylation sites onto GP1. Carbohydrate shielding, or glycosylation site additions, can be used to map glycoprotein structural domains (37-39). We engineered seven additional glycosylation sites throughout GP1 (Fig 3). All glycosylation sites were predicted to be present on the surface of the GP1 model, although H141N, N148S, V187T, and Y253N had potential to impede trimer formation based on the new trimeric structure (32).

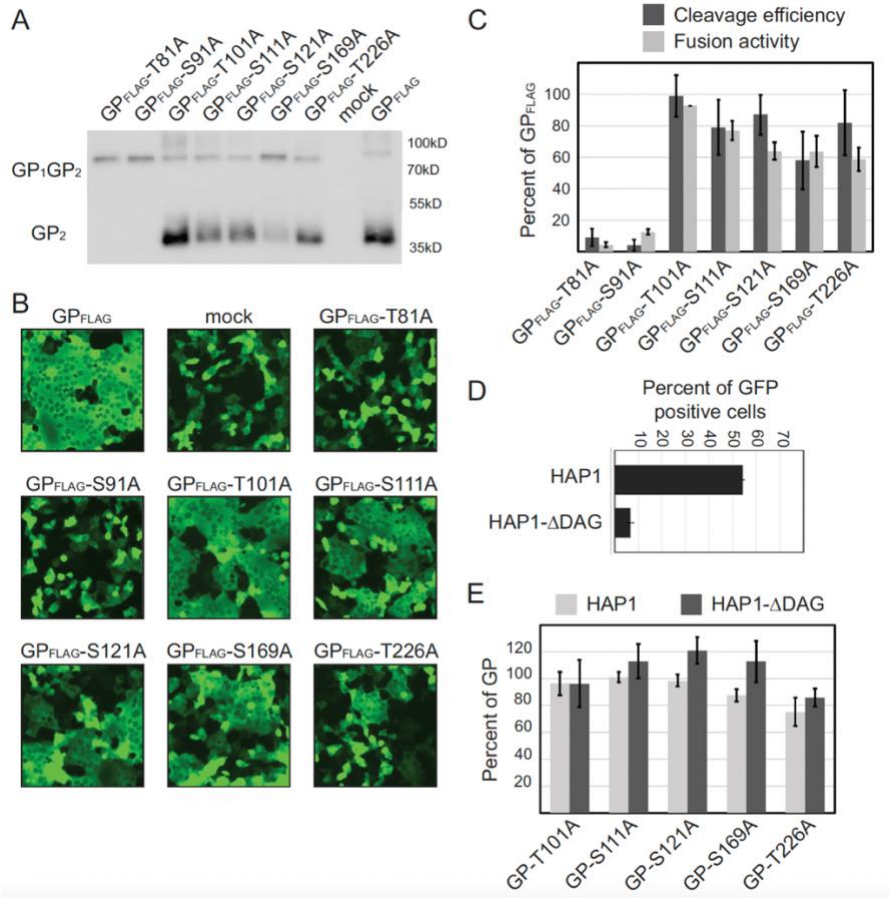

Fig 2. Processing and functional characteristics of surface-expressed GP1 N-glycosylation sites. (A) Vero cells were transfected with the indicated FLAG-tagged LASV GP variant or negative control. After 36 hours, cells were subjected to surface

biotinylation. Surface expressed biotinylated proteins were concentrated using streptavidin sepharose beads. Precipitated proteins were separated by SDS-PAGE. Immunoblots were carried out to detect LASV GP surface expressed protein using an anti-FLAG antibody, M2. Immunoblot is a representative of four trials. (B) Microphotographs of Vero cells co-transfected with plasmid DNA encoding LASV GP construct and GFP. Cell-to-cell fusion was assessed 3 h following low pH media shock; magnification ×20. Representative fields of view are shown. (C) Fusion data for each construct was quantified via counting unfused cells and comparing to mock transfected wells. Quantified fusion data for each construct was normalized to LASV wt-GPC-3xFLAG. Cleavage efficiency was normalized to FLAG tagged GP using densitometry analysis. (D) Parental GP transduction efficiency in HAP1 and HAP1-ΔDAG1 cells. VSVΔG-GFP pseudo-particles containing LASV GP were added to both cells and the number of GFP positive cells were enumerated in a flow cytometer. The percentage of the cell population that was GFP positive is shown. (E) VSVΔG-GFP pseudo-particles containing LASV GP or N-glycosylation mutants were used to transduce HAP1 and HAP1-ΔDAG1 cells. The number of GFP positive cells were enumerated in a flow cytometer. Transduction efficiencies were normalized to parental LASV GP particle transduction values in each respective cell type. All data are based on the average and standard error of the mean of at least three replicate experiments.

The mutants were evaluated for the incorporation of the glycan, as well as processing with surface biotinylation assays (Fig 3A). Glycosylation additions were confirmed by the slower mobility pattern of GP1-GP2 on an immunoblot compared to parental GP, which was observed for mutants H141N, V187T, D211S, and Q232N (Fig 3A). The remaining constructs K116S, N148S, and Y253N were not glycosylated, suggesting these motifs were not recognized by cellular glycotransferases. The trimeric structure predicts N148 and Y253 to be located at the center of the trimer, possibly making these residues inaccessible. K116 was also not glycosylated, despite its predicted location on top of the trimer with clear access to glycotransferases. The natural glycosylation site at N119 may sterically prevent neighboring glycan additions.

Cleavage was reduced for all glycosylated constructs except for D211S, indicating the additional glycans reduced SKI-1/S1P recognition or efficient GP trafficking to the Golgi in most cases. Cell-to-cell fusion activity was proportional to

cleavage efficiency, suggesting the additional glycans did not prevent GP2 activation at low pH if GP1-GP2 processing occurred (Fig 3B). Although Y253N did not appear to be glycosylated, the mutation decreased fusion relative to the amount of cleaved GP suggesting that the point mutation alone may decrease the efficiency of GP refolding and completing the fusion process.

Transduction assays were performed with K116S, N148S, D211S, and Y253N, which demonstrated >50% GP processing (Fig 3C). Both D211S and Y253N reduced transduction compared to parental GP, yet transduction levels between HAP1 and HAP1-ΔDAG1 cells were similar. This suggests mutations were not altering interactions with αDG, but inhibiting an entry step common in both cell types. The Y253 construct's reduced fusion activity may account for reduced transduction levels, while the additional glycan on D211S may have decreased transduction efficiency in both cell lines.

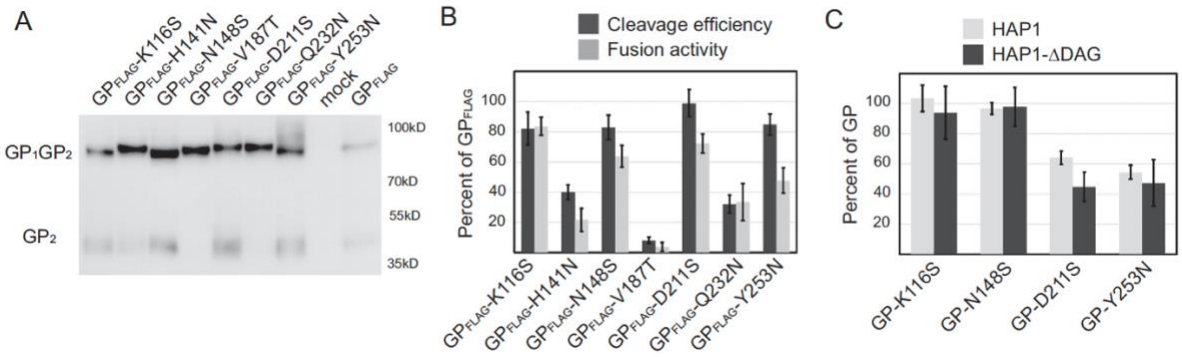

Fig 3. Functional analysis of GP1 containing engineered N-linked glycosylation sites. (A) Surface expressed GP of N-glycan mutants and immunoblot analysis using anti-FLAG antibody M2 for detection. (B) Cleavage efficiency and cell-to-cell fusion data. (C) Transduction of HAP1 and HAP1-ΔDAG1 cells using VSV pseudotyped particles. All data are based on the average and standard error of the mean of at least three replicate experiments.

Characterization of GP1 using insertional mutagenesis. Few of the additional N-linked glycosylation sites that we engineered were efficiently glycosylated (Fig 3). Therefore we employed insertional mutagenesis to add bulky epitope tags throughout

GP1 to impede receptor binding (Fig 4). The nine amino acid HA epitope tag (YPYDVPDYA) was inserted at 21 positions along the length of GP1. Insertion sites were chosen to avoid perturbation or disruption of protein tertiary structures. To increase the flexibility of the HA tag, 14 insertions included Gly-Gly-Ser linkers (lHA) flanking the insertion.

Surface expression of HA insertion constructs varied. Most constructs were produced, but the majority of insertions resulted in processing defects, evidenced by the lack of cleaved GP2 in surface biotinylated material (Fig 4A). Although the HA insertion sites were added to unstructured surface loops, the insertions appeared to alter protein folding in the majority of the constructs, preventing GPC processing by SKI-1/S1P. Overall, only seven of the twenty-one mutants displayed appreciable cleavage compared to parental GP (Fig 4A).

To test for GP fusion activity, the mutant constructs were expressed in Vero cells and incubated with a low pH buffer to trigger conformational changes. As expected, mutations that inhibited GPC cleavage did not display any fusion activity (Fig 4B). Constructs that retained GPC processing all produced syncytia, suggesting the HA insertions did not prevent the low-pH conformational changes when SKI-1/S1P recognition occurred (Fig 4B).

Transductions were carried out for seven of the 21 insertion constructs. Only one construct, 61HA, was able to transduce both cell lines (Fig 4C). The GP1/GP2 crystal structure found the N-terminal region of GP1 produces an extended β-sheet that interacts with GP2 (32) (Fig 1D). Therefore, the HA epitope tag addition after residue 61 would be near the viral membrane and separated from main body of GP1. Three constructs,

146HA, 227HA and 250HA, were able to transduce HAP1-ΔDAG1 cells but were unable to efficiently transduce HAP1 cells, suggesting that these insertions inhibit αDG utilization (Fig 4C). As expected, HAP1 transduction was not completely eliminated. Lassa entry into HAP1 can occur through an alternative pathway that does not require αDG (20, 36). Therefore, particles that have reduced affinity for αDG may still be able to enter HAP1 cells through the alternative, albeit less efficient pathway. The remaining three constructs; 150HA, 172HA and 230HA showed low to no transduction in both HAP1 cell lines, suggesting the inserts inhibited a step in the entry process that is in common between both cell lines, such as LAMP1 interaction (Fig 4C).

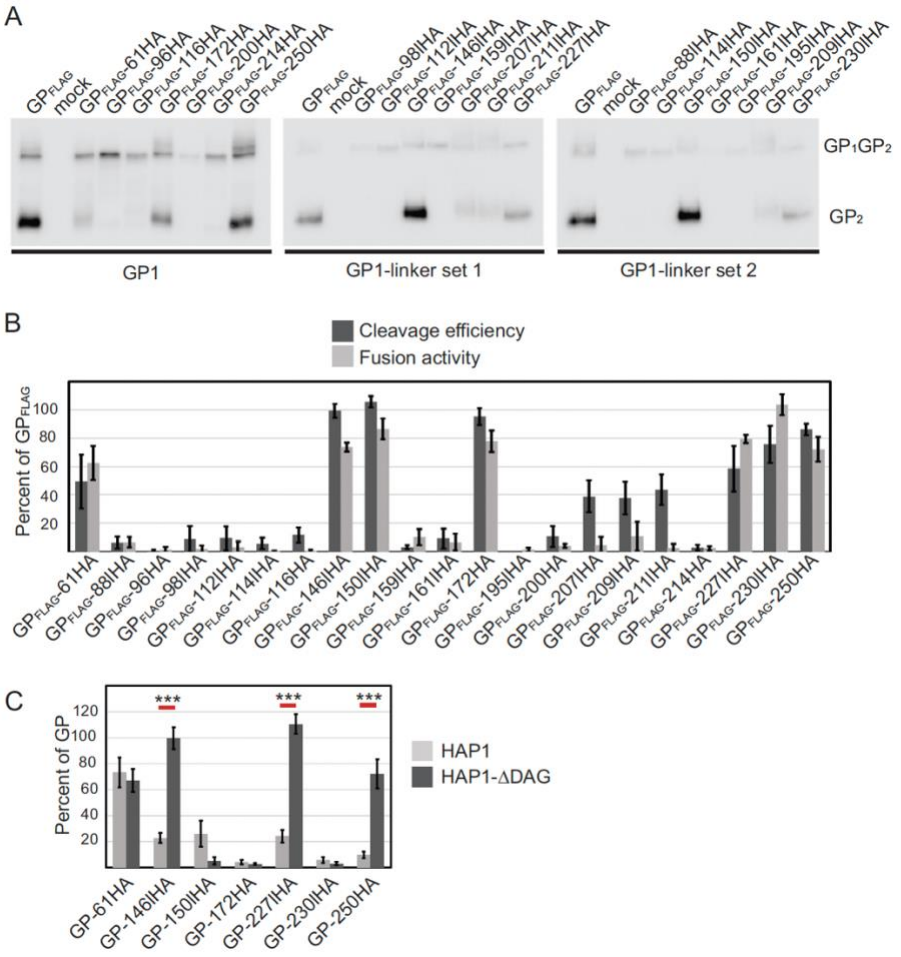

Fig 4. Insertional mutagenesis of LASV GPC blocks entry in specific cell lines. (A) Surface expressed HA-tagged mutants and immunoblot analysis detected with

anti-FLAG antibody M2. (B) Cleavage efficiency and cell-to-cell fusion data. (C) Transduction of HAP1 and HAP1-ΔDAG1 cells using VSV pseudotyped particles. All data are based on the average and standard error of the mean of at least three replicate experiments. ***, p-value < 0.001.

Alanine scanning of hydrophobic and charged residues. Large insertions and glycan additions tended to block GP cleavage, preventing full GP characterization. To increase the chances of producing GP trimers that are trafficked to the cell surface in a processed state, we introduced single amino acid substitutions. Hydrophobic and charged residues can be critical for virus glycoprotein-receptor interactions and entry (40-44). To locate possible αDG binding sites in LASV GP1, alanine scanning was used to mutate conserved hydrophobic and charged residues. Out of 16 hydrophobic mutants, 11 demonstrated more than a 50% reduction in cleavage efficiency, and/or fusion activity compared to parental GP (Fig 5 A-B). Several of the hydrophobic residues were located in secondary structures of GP1, and presumably alanine substitutions resulted in protein misfolding. For the remaining mutants, those that produced cleaved GP2 were able to form syncytia. The L133A mutant produced little protein, and along with the decreased cleavage efficiency (60% of parental GP), resulted in very low fusion activity.

Six hydrophobic mutants were examined in transduction assays. The majority of the hydrophobic mutations transduced both cell lines as well as wild-type GP (Fig 5C). The low protein level seen with L133A did not significantly impact transduction efficiency. While F147A was able to transduce HAP1-ΔDAG1 cells at a similar level as wild-type GP, transduction in HAP1 cells was reduced to 42%. The transduction defect in HAP1 cells with no defect in HAP1 ΔDAG1 cells suggests F147 is important for efficient αDG utilization.

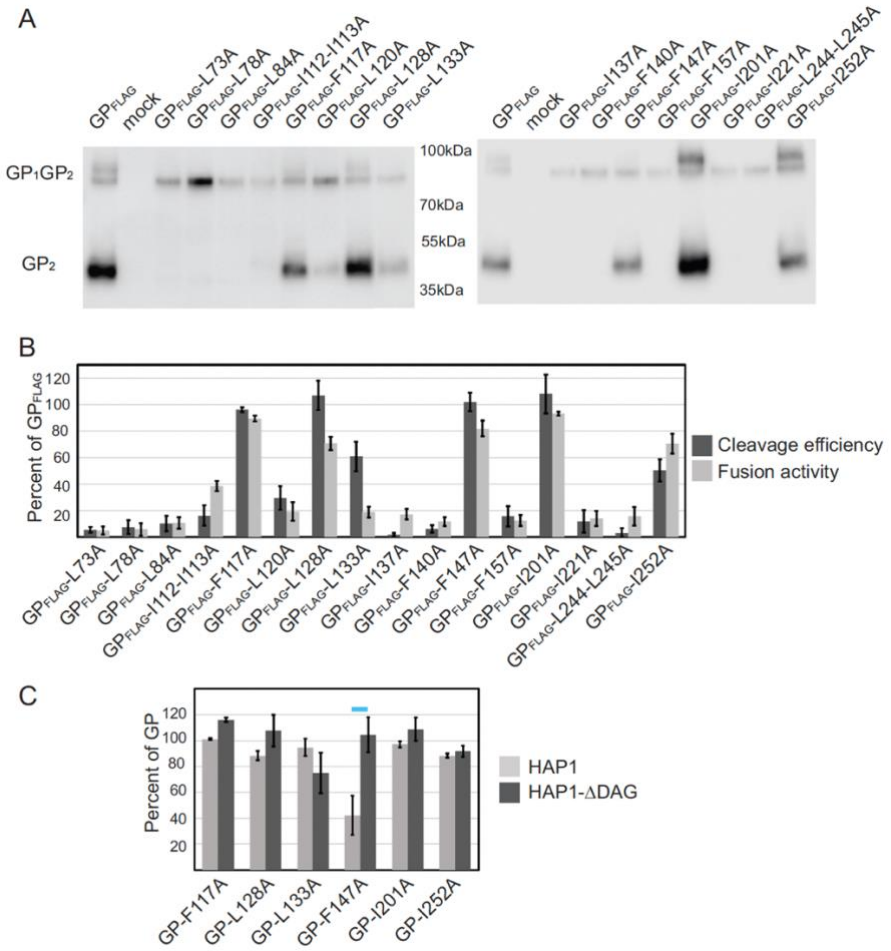

Fig 5. Mutating hydrophobic GP1 residues impedes protein processing. (A) Surface expressed hydrophobic mutants and immunoblot analysis using anti-FLAG antibody M2. (B) Cleavage efficiency and cell-to-cell fusion data. (C) Transduction of HAP1 and HAP1-ΔDAG1 cells using VSV pseudotyped particles. All data are based on the average and standard error of the mean of at least three replicate experiments. Blue dash highlights the constructs that transduced HAP1-ΔDAG1 similar to parental GP, yet show a defect in HAP1 entry.

Fourteen conserved charged residues were mutated to alanine, including a described histidine triad (H92, H93, and H230), which has been implicated in LAMP1 interaction (30, 33). All mutated GPs were cleaved and transported to the cell membrane at levels greater than 60% of parental GP (Fig 6A). The charged residue mutants also displayed high levels of cell-to-cell fusion activity (Fig 6B). Only GP mutant R248A-R250A demonstrated reduced fusion.

We produced VSV pseudoparticles expressing all fourteen charged mutations and tested their ability to transduce HAP1 and HAP1-ΔDAG1 cells (Fig 6C). Mutant H92A-H93A was unable to transduce either cell type tested. H230A, the third residue of the described histidine triad, showed relatively high levels of transduction. Mutants K125A-K126A, H141A, and R248A-R250A demonstrated a reduced transduction in HAP1 cells compared to HAP1-ΔDAG1 cells. Although transduction into HAP1 cells was not completely inhibited, the data suggest the mutations may decrease efficient interaction with αDG.

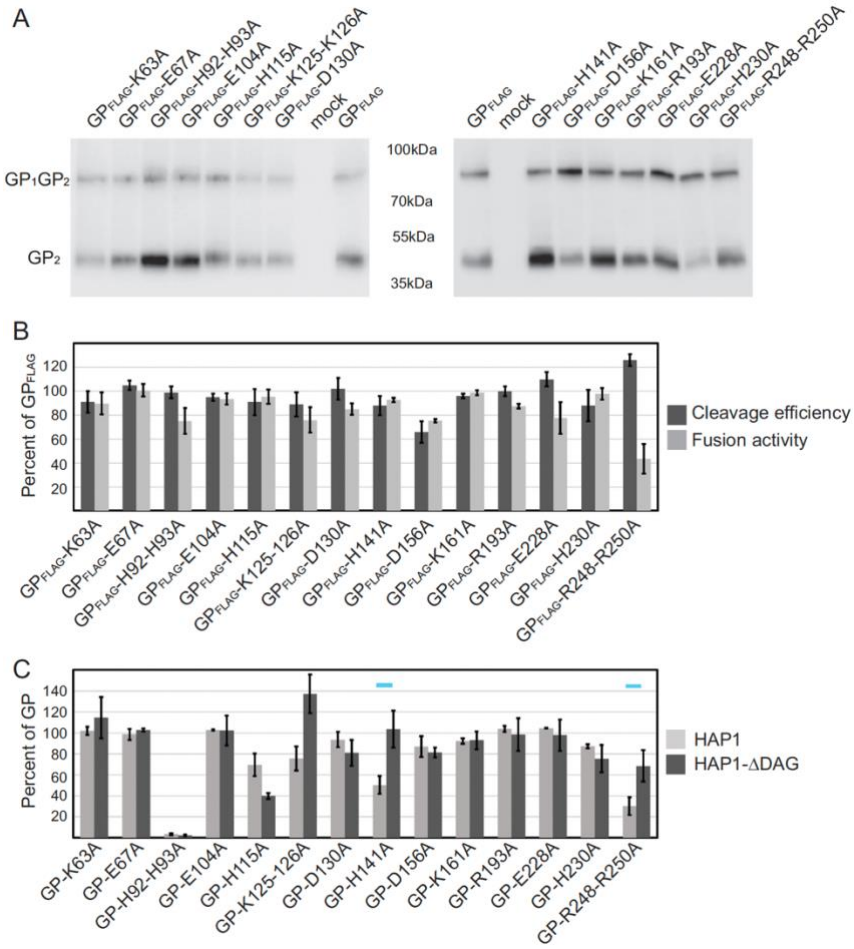

Fig 6. Charged GP1 residues are required for efficient HAP1 entry. (A) Surface expressed charged mutants and immunoblot analysis using anti-FLAG antibody M2. (B) Cleavage efficiency and fusion ability data. (C) Transduction of HAP1 and HAP1-ΔDAG1 cells using VSV pseudotyped particles. All data are based on the average

and standard error of the mean of at least three replicate experiments. Blue dash highlights the constructs that transduced HAP1-ΔDAG1 more than twice as efficiently as HAP1 cells.

Additional Targeted Mutations. The transduction data suggested residues located near the center of the GP1 trimer were key for efficient αDG entry. To more fully examine this region, an additional fifteen point mutations were created that focused on the regions surrounding the top of the GP1 trimer and residues adjacent to mutations that reduced transduction in HAP1 cells (Fig 7). To determine if combining some of the individual mutations that modestly decreased HAP1 entry would synergistically eliminate αDG binding, two double

mutants that incorporated mutations at GP residues 141 and 147 were made. Constructs H92Y-H93Y and H230Y were also made to compare the effects of alanine versus tyrosine substitutions and to reproduce similar constructs tested in the study by Cohen-Dvashi et al (30, 33). Overall, surface expression and processing of the additional targeted mutants were near wild-type LASV GP levels with the exception of H92Y-H93Y and H141N-F147A. Both of these double mutants were produced but were poorly processed (Fig 7A). When the asparagine at position H141 in the double mutant was changed to alanine, surface expression, processing, and fusion increased. Histidines at position 92 and 93, when changed to alanines, retain processing and fusion activity (Fig 6B), but tyrosine substitution lead to GPC processing defects (Fig 7A). Previous work by Cohen-Dvashi et al tested individual mutations H92Y, H93Y, and H230Y for processing, surface expression, and fusion activity (30). When they individually changed each histidine to tyrosine, they found a reduction in the level of cleaved, surface expressed GP, but no significant changes in cell-cell fusion. Our double mutant, H92Y-H93Y,

completely inhibited GP processing as well as fusion (Fig 7A and B). Similar to the previous study, H230Y was efficiently processed and induced cell-to-cell fusion at levels greater than wild-type GP. In general fusion activity, with the exception of A177S, again closely correlated with cleavage efficiency (Fig 7B).

Of the 15 constructs made, 13 were tested in transduction assays. Only two constructs; Y150A and H141A/F147A showed reduced transduction in HAP1 cells compared to HAP1-ΔDAG1 cells (Figure 7C). The combination of H141A and F147A had an additive effect. Individual changes dropped HAP1 transduction to 40% of parental GP, and the double mutant dropped HAP1 transduction to 10% of parental GP while retaining near wild-type levels of HAP1-ΔDAG1 transduction. All other constructs were able to transduce HAP1 and HAP1-ΔDAG1 cells with similar efficiencies (Fig 7C). While H230Y did not result in cell type specific transduction defects, this mutation moderately reduced transduction in both cell lines, similar to the previous study (30).

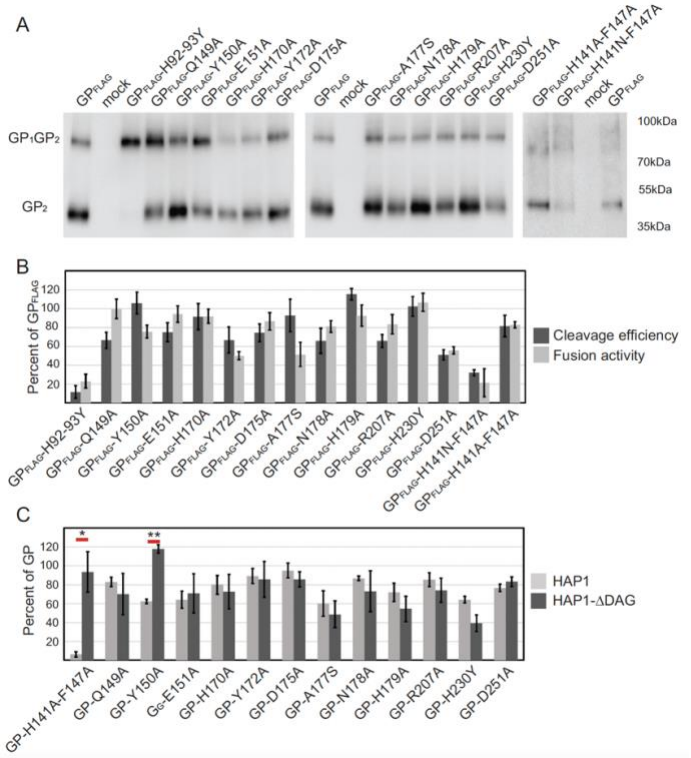

Fig 7. Residues involved with the GP1 trimer core are critical for αDG interaction. (A) Surface expressed targeted GP1 mutants and immunoblot analysis using anti-FLAG antibody M2. (B) Cleavage efficiency and fusion ability data. (C) Transduction of HAP1 and HAP1-ΔDAG1 cells using VSV pseudotyped particles. All data are based on the average and standard error of the mean of at least three replicate experiments. *, p-value <0.05; 88, p-value <0.01.

GP incorporation onto VSV particles. While many of the constructs produced particles that transduced both cell types, some constructs did not efficiently transduce either cell line, or displayed a deficiency in a specific cell type. To ensure the low transducing constructs incorporated sufficient levels GP on the particle, immunoblots were performed (Fig 8). All particles incorporated the mutated GP constructs, including those constructs that failed to transduce both cell lines. K125A-K126A and Y150A, two mutants that demonstrated a reduction in HAP1 transduction and an enhancement in HAP1-ΔDAG1 cells, were consistently found on VSV particles at higher levels than wild-type GP. Similarly, R248-R250A was found on particles at a higher rate that parental GP, although it did not transduce better than wild-type.

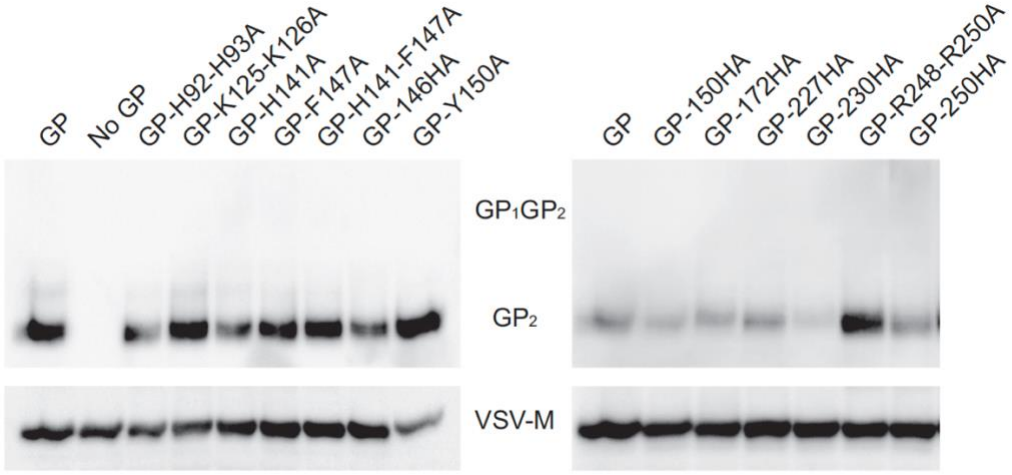

Fig 8. GP constructs are efficiently incorporated onto VSV particles. Vero cells were used to produce VSV pseudo-particles. Cell supernatants, containing pseudotyped particles, were collected and precipitated with TCA to determine the level of LASV GP incorporation into VSV envelopes. GP constructs demonstrating low HAP1

transduction, or GP constructs that were unable to transduce both cell types were tested. Precipitated proteins were separated by SDS-PAGE and immunoblotted for LASV GP2 (monoclonal 12.4D) and VSV-M (monoclonal 23H12).

Residues H141-F147 and R248-R250 are critical for αDG interaction. In order to directly assess the ability of GP mutants to bind with αDG, we performed a co-immunoprecipitation experiment. Beads coated with αDG were incubated with VSV pseudotyped particles containing either parental or mutant GP. We examined GP-H141A-F147A and GP-R248A-R250A, because they each contained point mutations that resulted in HAP1 entry defects. In addition, we evaluated GP-H230Y, a construct implicated in LAMP1 binding. Parental GP and GP-H230Y were efficiently precipitated by αDG, whereas we were unable to biochemically detect GP-H141A-F147A and GP-R248A-R250A (Fig 9A). This data further supports our conclusions that the central core of GP mediates interaction with αDG (Fig 9B).

Discussion

Here we provide data highlighting LASV GP1 residues important for receptor interactions. We produced and characterized a library of 80 constructs. Transduction was monitored in cell lines that differentially express the LASV receptor αDG. Biochemical characterization grouped GP1 mutants into various categories based on their transduction phenotypes (Table 1). The data implicate regions of GP1 that facilitate entry through αDG, as well as residues involved with LAMP1 interaction. We tested all of the constructs in cell-to-cell fusion assays, and those that were efficiently processed, in pseudotype particle entry assays. A number of mutants including, H92A-H93A, 150lHA, 172HA, and 230lHA, produced large syncytia in cell-to-cell fusion assays, yet were unable to facilitate entry when incorporated onto VSV particles. This suggests the

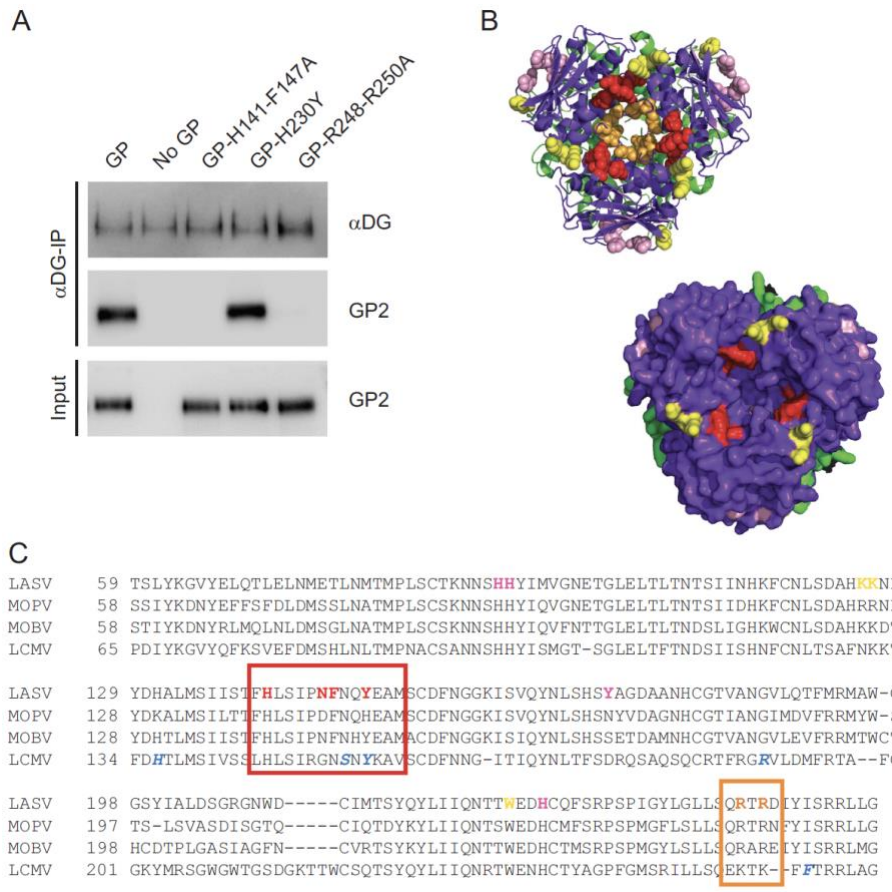

Fig 9. Identification and mapping residues implicated in LASV receptor-binding and viral entry. (A) To directly examine GP1 mutant binding, or lack of binding, to αDG, we performed a co-immunoprecipitation assay. αDG coated beads were incubated with VSV pseudotyped particles containing either parental or mutant LASV GP. All proteins interacting with the αDG coated beads were concentrated and separated by SDS-PAGE. While parental GP and GP-H230Y were able to bind to αDG, GP-H141A-F147A and GP-R248A-R250A were not. (B) LASV GP constructs exhibiting reduced entry into HAP1 cells were mapped onto the LASV pre-fusion crystal structure (PDB 5vk2; GP1 is shown in purple and GP2 is shown in green). Regions that are significantly involved in αDG interactions are shown in red (H141, N146, F147, and Y150). Regions that also demonstrated reduced HAP1 entry are shown in orange (R248 and R250) and yellow (K125, K126 and W227). The histidine triad is shown in pink (H92, H93, and H230). Residues are color coded to match Table 1. Both a cartoon structure and surface rendering of the structure demonstrates that the αDG binding site is located in a cavity on the top of the trimer. (C) Sequence alignment of Old World arenaviruses that use αDG. Regions in LCMV involved in αDG binding are shown in blue, while the regions we have implicated for LASV entry are shown in red. R248 and R250 are highlighted in orange. The histidine triad implicated in LAMP1 interaction are in pink.

requirements for cell-to-cell fusion and virus-to-cell fusion are different. The luminal pH of most lysosomes ranges from 4.5-5 (45). In contrast, we utilized PBS at pH 4 in the cell-to-cell fusion assay because this pH produced the most syncytia (data not shown and (46, 47)). We speculate LAMP1 may facilitate fusion pore formation at a more alkaline pH, thereby increasing the efficiency of LASV entry (30). The fusion assay may be able to circumvent the LAMP1 requirement with a more acidic environment, triggering fusion pore formation without LAMP1 interaction. This would explain why mutants can produce large syncytia when exogenous buffer is added, yet are unable to productively enter cells on a pseudotyped particle. Removal of LAMP1 from cells dramatically decreases LASV entry efficiency, but does not eliminate it (20). Perhaps some virions encounter lysosomes with lower pH ranges, and the extra acidic environment overcomes the LAMP1 requirement similar to the cell-to-cell fusion assay.

LASV entry requires interactions with both cell surface receptors and an internal receptor, LAMP1 (20). As previously mentioned, we identified a number of constructs that blocked entry into both cell types tested: H92A-H93A, 150lHA, 172HA, and 230lHA. Both H92-H93 and H230 have been previously implicated in GP1-LAMP1 interaction (33). Protonation of the histidine residues may facilitate conformational changes that expose the LAMP1 binding site (30), which cryo-ET reconstructions suggest occurs in grooves between GP1 monomers that form under low-pH conditions (31). While histidines at positions 92, 93, and 230 may facilitate the low-pH conformational changes, 150lHA and 172HA fall on the opposite face of the crystal structure. If LAMP1 binding is occurring in a low-pH induced groove, both 150lHA and 172HA may sterically prevent LAMP1 binding, or cause premature shedding of GP1 from the

glycoprotein complex. We did not identify any individual point mutations that prevented entry into both cell lines that were not previously associated with inducing low-pH conformational changes, suggesting further work is required to locate the specific residues directly involved in LAMP1 interaction.

While most constructs efficiently entered both cell lines, those containing mutations between amino acids 141-150 and 248-250 of GP1 demonstrated reduced transduction in HAP1 cells expressing αDG. A co-immunoprecipitation using VSV pseudotyped particles confirmed the role of residues H141, F147, R248, and R250 in direct αDG binding. Residues H141, N146, F147, and Y150 face the three-fold axis of the trimer, forming a putative receptor binding site (Fig 9B, shown in red). A similar region within LCMV has been implicated in LCMV GP1-αDG interaction (22). Previous biochemical studies show OW arenavirus monomeric GP1 is unable to interact with αDG, which supports a binding site that requires an intact trimer (20, 22, 33). Residues R248 and R250 also face this center axis, but are located deeper in the core (Fig 9B, shown in orange). Presumably, αDG would not be interacting with the buried center of the trimer, but removal of the charged residues may alter the conformation of the domain above. K125A-K126A and 227HA modestly reduced HAP1 transduction and are located further away from the trimeric center. These mutations may exert long-range conformational changes that alter the αDG binding site (Fig 9B, shown in yellow). For example, K125 and K126 line the GP1-GP1 interface within the trimer, and therefore may play a role in maintaining the center conformation.

In 2015, the largest screen of LASV genomes revealed that isolates are highly heterogeneous and group by geographic distribution (48). The GP1 subunit had the

highest sequence diversity of the four viral proteins, presumably due to continuous immune selection. When comparing the GP1 subunit among the 180 sequences collected, 68% of the amino acid sequence was conserved. However, the regions we identified in this study that mediate αDG entry were 98-100% conserved, suggesting these residues are important for the structure or function of GP1. The few residues that differed contained conservative amino acid substitutions. Several additional Old World arenaviruses including LCMV, Mopeia (MOPV), and Mobala (MOBV) use αDG as their primary surface receptor (49). A GP1 sequence alignment of these four viruses reveals the regions we identified in LASV-αDG engagement are similar among these Old World arenaviruses (Fig 9C). Furthermore, LCMV shares 63% sequence identity with LASV, and similar regions on GP1 have been implicated in LCMV's GP1-αDG binding site (22). Five residues have been identified which enhance LCMV GP1 binding to αDG; H136, S153, Y155, R190, and L260 (22, 50-54). Residues S153, Y155, R190, and L260 are located in the same region on GP1 that faces the three-fold trimer axis (22), further supporting this region's importance in αDG binding.

In summary, our data suggests that the αDG binding site on LASV GP1 is found at the top central core of the GP trimer. These data correlate with the hypothesized αDG binding regions within LCMV GP1 (22). Our data supports the hypothesis that the histidine triad plays a role in the pH conformational changes required for LAMP1 interaction. In addition, we identify two HA insertion mutants, 150HA and 172HA, that may sterically block LAMP1 binding. Knowledge gained by this study will aid the development of small molecule inhibitors to block LASV entry through its receptors αDG and LAMP1.

Table 1. Summary of Fusion, GP cleavage and Transductions

Mutant	Classification	Fusion Activity	Cleavage Efficiency	Transduction Efficiency		Class
				HAP1	HAP1-	
L61HA	HA insertion	62.4 ±	49.4 ± 19	73.6 ±	67.9 ±	III
K63A	Charged	89.8 ±	91.3 ± 9.3	102.1	114.5	III
E67A	Charged	100.8 ±	104.9 ±	98.7 ±	102.9	III
H92A-	Charged	75.0 ±	99.1 ± 5.0	3.4 ±	2.3 ±	I
T101A	N-gly	92.8 ±	98.9 ±	96.5 ±	96.3 ±	III
E104A	Charged	93.7 ±	95.5 ± 3.4	102.8	102.4	III
S111A	N-gly	77.1 ±	79.4 ±	101.2	112.9	III
H115A	Charged	95.5 ±	91.3 ±	69.6 ±	39.9 ±	III
K116S	N-gly	83.6 ±	82.1 ±	103.5	93.9 ±	III
F117A	Hydrophobic	89.4 ±	96.3 ± 1.8	101.1	116.1	III
S121A	N-gly	64.0 ±	86.8 ±	98.6 ±	121.0	III
K125A-	Charged	76.0 ±	89.5 ±	75.6 ±	137.2	II
L128A	Hydrophobic	70.8 ±	107.0 ±	88.3 ±	107.8	III
D130A	Charged	85.0 ±	102.3 ±	93.7 ±	81.0 ±	III
L133A	Hydrophobic	19.0 ±	61.0 ±	94.7 ±	75.0 ±	III
H141A	Charged	92.7 ±	87.8 ± 8.3	50.3 ±	103.7	II
F147A	Hydrophobic	82.0 ±	102.1 ±	42.2 ±	104.5	II
H141A-	Targeted	82.8 ±	81.6 ±	17.4 ±	93.5 ±	II
N146lHA	HA + linker	73.7 ±	99.4 ± 4.8	23.0 ±	100.5	II
N148S	N-gly	63.8 ±	83.3 ± 7.9	96.7 ±	97.9 ±	III
Q149A	Targeted	99.6 ±	66.5 ± 8.5	83.1 ±	70.1 ±	III
Y150A	Targeted	75.5 ±	105.9 ±	62.2 ±	117.9	II
Y150lHA	HA + linker	86.6 ±	105.8 ±	26.0 ±	5 ± 0.8	I
E151A	Targeted	94.1 ±	75.1 ±	64.1 ±	70.9 ±	III
D156A	Charged	75.4 ±	66.1 ± 8.5	87.0 ±	81.4 ±	III
K161A	Charged	98.6 ±	96.1 ± 1.8	92.2 ±	93.0 ±	III
S169A	N-gly	63.7 ±	58.4 ±	87.6 ±	112.8	III
H170A	Targeted	91.2 ±	91.5 ±	80.0 ±	72.7 ±	III
Y172A	Targeted	50.0 ±	66.6 ±	89.3 ±	85.5 ±	III
Y172HA	HA insertion	77.9 ±	95.4 ± 5.9	4.3 ±	4.6 ±	I
D175A	Targeted	86.6 ±	74.4 ± 9.5	95.1 ±	85.6 ±	III
A177S	Targeted	51.4 ±	92.7 ±	60.1 ±	48.6 ±	III
N178A	Targeted	81.1 ±	65.9 ±	86.9 ±	73.2 ±	III
H179A	Targeted	92.6 ±	115.3 ±	71.9 ±	54.5 ±	III
R193A	Charged	87.5 ±	99.7 ± 3.7	103.9	98.5 ±	III
I201A	Hydrophobic	93.3 ±	108.0 ±	97.1 ±	108.8	III
R207A	Targeted	83.4 ±	65.8 ± 6.7	85.4 ±	74.2 ±	III
D211S	N-gly	72.3 ±	99.5 ± 8.9	64.1 ±	44.7 ±	III
T226A	N-gly	58.6 ±	82.4 ±	75.3 ±	85.9 ±	III
W227lHA	HA + linker	79.5 ±	58.5 ± 16	24.3 ±	103.7	II

E228A	Charged	77.7 ±	109.7 ±	104.6	97.8 ±	III
H230A	Charged	97.7 ±	87.6 ±	87.3 ±	75.4 ±	III
H230Y	Targeted	106.7 ±	102.3 ±	64.1 ±	39.4 ±	III
H230lHA	HA + linker	103.8 ±	75.8 ± 13	5.9 ±	5.3 ±	I
R250HA	HA insertion	72.3 ±	86.2 ± 4	10.2 ±	82.5 ±	II
D251A	Targeted	55.7±3.9	50.9 ± 5.4	76.6 ±	83.2 ±	III
R248A-	Charged	43.4 ±	128.9 ±	30.2 ±	68.5 ±	II
I252A	Hydrophobic	70.5 ±	50.5 ± 8.3	88.3 ±	91.8 ±	III
Y253N	N-gly	47.7 ±	84.9 ± 7.2	54.4 ±	47.2 ±	III

I: Transduction reduced in both cell types; II: Transduction reduced in HAP1 cells compared to HAP1-ΔDAG cells; III: No receptor binding defects

Materials and Methods

Cell lines and transfections. Vero (African green monkey kidney) cells stably expressing human SLAM were maintained in Dulbecco's modified Eagle's medium (DMEM) supplemented with 5% (vol/vol) fetal bovine serum (FBS) at 37°C and 5% CO_2 (55). HAP1 and HAP1-ΔDAG1 cells (Horizon Discovery) were maintained in Iscove's media supplemented with 10% (vol/vol) FBS at 37°C and 5% CO_2. All transient transfections were performed using GeneJuice (Millipore) as per manufacturer's instructions.

Molecular biology. The LASV GPC protein coding sequence was codon optimized for mammalian expression and cloned into a pcDNA3.1intron vector. Gene expression was initiated by a CMV promotor and the β-globin intron was engineered in the 5' untranslated region (UTR) to increase protein production. A carboxy-terminal 3xFLAG tag was added to the cytoplasmic tail of the GP2 subunit for biochemical detection. HA tag coding sequence (YPYDVPDYA) was added to the plasmid at the indicated locations using PCR-based insertional mutagenesis with Q5 polymerase (NEB). Point mutations were introduced with QuikChange mutagenesis and PfuTurbo-HS

polymerase (Agilent). The plasmid DNA of each construct was sequenced, and the presence of each mutation was confirmed. Complete sequence information is available upon request.

Surface biotinylation. Vero cells were transfected with plasmid DNA encoding the indicated Lassa GPC mutants. Thirty-six hours following transfection, cells were washed with cold PBS and biotinylated with 0.5 mg/mL sulfosuccinimidyl-2-(biotinamido) ethyl-1,3-dithiopropionate (Thermo) for 30 min on ice. The reaction was quenched using Tris-HCl, and cells were lysed in M2 lysis buffer (50 mM Tris, pH 7.4, 150 mM NaCl, 1 mM EDTA, 1% Triton X-100) at 4°C and clarified with centrifugation (20,000xg, 15 min). Lysate was incubated with streptavidin sepharose beads (GE Healthcare) for 60 min while rotating. Following incubation, the streptavidin sepharose beads were washed in buffer 1 (100 mM Tris (44), 500 mM lithium chloride, 0.1% Triton X-100) and then in buffer 2 (20 mM HEPES [pH 7.2], 2 mM EGTA, 10 mM magnesium chloride, 0.1% Triton X-100), incubated in urea buffer (200 mM Tris, pH 6.8, 8 M urea, 5% sodium dodecyl sulfate [SDS], 0.1 mM EDTA, 0.03% bromophenol blue, 1.5% dithiothreitol) for 30 min at 55°C, and subjected to immunoblot analysis.

Antibodies and immunoblots. Surface biotinylated material was fractionated by gel electrophoresis on 10% Tris-glycine gels (ThermoFisher) and transferred to polyvinylidene difluoride (PVDF) membranes (GE Healthcare). GP was detected with specific antibodies directed against the Flag epitope tag (M2; Sigma). Immunoblots were developed using mouse IgG horseradish peroxidase (HRP)-conjugated secondary antibodies (Jackson) and a ChemiDoc digital imaging system (Bio-Rad). Each experiment was repeated at least three independent times and a representative image is

shown. Trichloroacetic acid (TCA) precipitated pseudotyped particles were fractionated as described for biotinylated material. Protein was detected with specific antibodies directed against LASV GP2 (22.5D), kindly provided by Dr. James Robinson (Tulane University), and against VSV matrix (23H12, courtesy of Dr. Douglas Lyles; Kerafast) (56, 57). Alpha dystroglycan was detected with IIH6 monoclonal antibody (EMD Millipore). Immunoblots were developed using HRP-conjugated human IgG and mouse IgG (Jackson) secondary antibodies, respectively, and a ChemiDoc digital imaging system (Bio-Rad). Immunoblots were quantified using ImageLab software.

Cell-to-cell fusion assay. Vero cells were co-transfected with Lassa GP mutants and pmaxGFP (4:1 ratio). Forty hours following transfection, media was removed and replaced with DPBS (pH 4) and incubated (37°C and 5% CO_2) for 30 min to allow glycoprotein triggering. The DPBS was replaced with DMEM and cells were incubated for an additional 3 hours to enable membrane rearrangement and clear syncytia formation. Four representative pictures of the fusion were taken using the Zoe microscope (Bio-Rad) (20x magnification) and unfused cells were counted. Quantification of fusion was calculated using the following equation:

$$Fusion = \frac{(unfused\ cells\ in\ mock\ transfected - unfused\ cells\ in\ mutant\ transfected)}{(unfused\ cells\ in\ mock\ transfected - unfused\ cells\ in\ WT\ GPC\ transfected)} \times 100$$

Each mutant was assessed in the fusion assay in three independent experiments.

VSV pseudotype production and transductions. GP constructs lacking the c-terminal 3xFlag tag were used to make the vesicular stomatitis virus (VSV) pseudotyped particles. Vero cells were transfected with LASV GP DNA. Thirty-six hours following

transfection the cells were transduced with VSVΔG-GFP particles pseudotyped with VSV-G (MOI 1) for one hour (courtesy of Dr. Michael Whitt; KeraFAST) (58). The particle-containing media was then replaced with fresh DMEM. VSVΔG-GFP particles displaying the LASV GP were collected 12 hours following the transduction. These particles were applied onto HAP1 and HAP1-ΔDAG1 cells in volumes of 0.25 mL and 1 mL, respectively. A higher volume of particles was used to transduce HAP1- ΔDAG1 cells in order to overcome the decreased transduction efficiency when the cells are missing the primary receptor (20). The number of GFP positive cells was enumerated in a flow cytometer. Results are displayed as the percent of GFP positive cells present in a population of 10,000 live cell events compared to GP wild-type transduction. To monitor GP incorporation onto the VSV particles, 1 mL of pre-cleared VSV transduction particles were precipitated using 10% wt/vol TCA. The TCA treated proteins were pelleted (20,000xg, 30 min, 4°C), washed with acetone, dried, and denatured using SDS-Urea buffer (200 mM Tris, pH 6.8, 8 M urea, 5% sodium dodecyl sulfate [SDS], 0.1 mM EDTA, 0.03% bromophenol blue). Particles were subjected to immunoblot analysis for both VSV matrix levels and incorporated GP2.

Co-immunoprecipitation. Sheep polyclonal anti-human dystroglycan antibodies (R&D Systems) were bound to protein G beads (BioRad) and incubated with αDG purified from rabbit muscle (59). The prepared beads were then divided equally into VSV pseudotyped particles containing a normalized about of GP and incubated for 1 hour. Protein complexes were precipitated and washed three times with PBS. Bound proteins were eluted by incubating beads with urea-SDS plus DTT, heat denatured (56°C for 30

min), and separated on SDS-PAGE. Immunoblot analysis examined the amount of precipitated αDG and associated GP2.

Acknowledgements

We thank the CVM Cytometry Core Facility for technical assistance, members of the Brindley lab for helpful comments on the manuscript, and Dr. James Robinson at Tulane University for providing antibodies against LASV GP.

This work was supported by the National Institutes of Health [AI104800, 2015].

References

1. Frame JD, Baldwin JM, Jr., Gocke DJ, Troup JM. 1970. Lassa fever, a new virus disease of man from West Africa. I. Clinical description and pathological findings. Am J Trop Med Hyg 19:670-6.

2. Gunther S, Lenz O. 2004. Lassa virus. Crit Rev Clin Lab Sci 41:339-90.

3. Mofolorunsho KC. 2016. Outbreak of lassa fever in Nigeria: measures for prevention and control. Pan Afr Med J 23:210.

4. Fichet-Calvet E, Rogers DJ. 2009. Risk maps of Lassa fever in West Africa. PLoS Negl Trop Dis 3:e388.

5. Ogbu O, Ajuluchukwu E, Uneke CJ. 2007. Lassa fever in West African sub-region: an overview. J Vector Borne Dis 44:1-11.

6. Monath TP, Newhouse VF, Kemp GE, Setzer HW, Cacciapuoti A. 1974. Lassa virus isolation from Mastomys natalensis rodents during an epidemic in Sierra Leone. Science 185:263-5.

7. Olayemi A, Cadar D, Magassouba N, Obadare A, Kourouma F, Oyeyiola A, Fasogbon S, Igbokwe J, Rieger T, Bockholt S, Jerome H, Schmidt-Chanasit J, Garigliany M, Lorenzen S, Igbahenah F, Fichet JN, Ortsega D, Omilabu S, Gunther S, Fichet-Calvet E. 2016. New Hosts of The Lassa Virus. Sci Rep 6:25280.

8. Ajayi NA, Ukwaja KN, Ifebunandu NA, Nnabu R, Onwe FI, Asogun DA. 2014. Lassa fever - full recovery without ribavarin treatment: a case report. Afr Health Sci 14:1074-7.

9. Yun NE, Walker DH. 2012. Pathogenesis of Lassa fever. Viruses 4:2031-48.

10. Burri DJ, Pasqual G, Rochat C, Seidah NG, Pasquato A, Kunz S. 2012. Molecular characterization of the processing of arenavirus envelope glycoprotein precursors by subtilisin kexin isozyme-1/site-1 protease. J Virol 86:4935-46.

11. Kunz S, Edelmann KH, de la Torre JC, Gorney R, Oldstone MB. 2003. Mechanisms for lymphocytic choriomeningitis virus glycoprotein cleavage, transport, and incorporation into virions. Virology 314:168-78.

12. Beyer WR, Popplau D, Garten W, von Laer D, Lenz O. 2003. Endoproteolytic processing of the lymphocytic choriomeningitis virus glycoprotein by the subtilase SKI-1/S1P. J Virol 77:2866-72.

13. Lenz O, ter Meulen J, Klenk HD, Seidah NG, Garten W. 2001. The Lassa virus glycoprotein precursor GP-C is proteolytically processed by subtilase SKI-1/S1P. Proc Natl Acad Sci U S A 98:12701-5.

14. Bederka LH, Bonhomme CJ, Ling EL, Buchmeier MJ. 2014. Arenavirus stable signal peptide is the keystone subunit for glycoprotein complex organization. MBio 5:e02063.

15. Messina EL, York J, Nunberg JH. 2012. Dissection of the role of the stable signal peptide of the arenavirus envelope glycoprotein in membrane fusion. J Virol 86:6138-45.

16. Eichler R, Lenz O, Strecker T, Garten W. 2003. Signal peptide of Lassa virus glycoprotein GP-C exhibits an unusual length. FEBS Lett 538:203-6.

17. Briknarova K, Thomas CJ, York J, Nunberg JH. 2011. Structure of a zinc-binding domain in the Junin virus envelope glycoprotein. J Biol Chem 286:1528-36.

18. York J, Nunberg JH. 2007. A novel zinc-binding domain is essential for formation of the functional Junin virus envelope glycoprotein complex. J Virol 81:13385-91.

19. York J, Nunberg JH. 2006. Role of the stable signal peptide of Junin arenavirus envelope glycoprotein in pH-dependent membrane fusion. J Virol 80:7775-80.

20. Jae LT, Raaben M, Herbert AS, Kuehne AI, Wirchnianski AS, Soh TK, Stubbs SH, Janssen H, Damme M, Saftig P, Whelan SP, Dye JM, Brummelkamp TR. 2014. Virus entry. Lassa virus entry requires a trigger-induced receptor switch. Science 344:1506-10.

21. Cao W, Henry MD, Borrow P, Yamada H, Elder JH, Ravkov EV, Nichol ST, Compans RW, Campbell KP, Oldstone MB. 1998. Identification of alpha-dystroglycan as a receptor for lymphocytic choriomeningitis virus and Lassa fever virus. Science 282:2079-81.

22. Hastie KM, Igonet S, Sullivan BM, Legrand P, Zandonatti MA, Robinson JE, Garry RF, Rey FA, Oldstone MB, Saphire EO. 2016. Crystal structure of the prefusion surface glycoprotein of the prototypic arenavirus LCMV. Nat Struct Mol Biol doi:10.1038/nsmb.3210.

23. Igonet S, Vaney MC, Vonrhein C, Bricogne G, Stura EA, Hengartner H, Eschli B, Rey FA. 2011. X-ray structure of the arenavirus glycoprotein GP2 in its postfusion hairpin conformation. Proc Natl Acad Sci U S A 108:19967-72.

24. Eschli B, Quirin K, Wepf A, Weber J, Zinkernagel R, Hengartner H. 2006. Identification of an N-terminal trimeric coiled-coil core within arenavirus glycoprotein 2 permits assignment to class I viral fusion proteins. J Virol 80:5897-907.

25. Shimojima M, Stroher U, Ebihara H, Feldmann H, Kawaoka Y. 2012. Identification of cell surface molecules involved in dystroglycan-independent Lassa virus cell entry. J Virol 86:2067-78.

26. Goncalves AR, Moraz ML, Pasquato A, Helenius A, Lozach PY, Kunz S. 2013. Role of DC-SIGN in Lassa virus entry into human dendritic cells. J Virol 87:11504-15.

27. Rojek JM, Sanchez AB, Nguyen NT, de la Torre JC, Kunz S. 2008. Different mechanisms of cell entry by human-pathogenic Old World and New World arenaviruses. J Virol 82:7677-87.

28. Oppliger J, Torriani G, Herrador A, Kunz S. 2016. Lassa virus cell entry via dystroglycan involves an unusual pathway of macropinocytosis. J Virol doi:10.1128/JVI.00257-16.

29. Nunberg JH, York J. 2012. The curious case of arenavirus entry, and its inhibition. Viruses 4:83-101.

30. Cohen-Dvashi H, Israeli H, Shani O, Katz A, Diskin R. 2016. Role of LAMP1 Binding and pH Sensing by the Spike Complex of Lassa Virus. J Virol 90:10329-10338.

31. Li S, Sun Z, Pryce R, Parsy ML, Fehling SK, Schlie K, Siebert CA, Garten W, Bowden TA, Strecker T, Huiskonen JT. 2016. Acidic pH-Induced Conformations and LAMP1 Binding of the Lassa Virus Glycoprotein Spike. PLoS Pathog 12:e1005418.

32. Hastie KM, Zandonatti MA, Kleinfelter LM, Heinrich ML, Rowland MM, Chandran K, Branco LM, Robinson JE, Garry RF, Saphire EO. 2017. Structural basis for antibody-mediated neutralization of Lassa virus. Science 356:923-928.

33. Cohen-Dvashi H, Cohen N, Israeli H, Diskin R. 2015. Molecular Mechanism for LAMP1 Recognition by Lassa Virus. J Virol 89:7584-92.

34. Bonhomme CJ, Capul AA, Lauron EJ, Bederka LH, Knopp KA, Buchmeier MJ. 2011. Glycosylation modulates arenavirus glycoprotein expression and function. Virology 409:223-33.

35. Eichler R, Lenz O, Garten W, Strecker T. 2006. The role of single N-glycans in proteolytic processing and cell surface transport of the Lassa virus glycoprotein GP-C. Virol J 3:41.

36. Jae LT, Raaben M, Riemersma M, van Beusekom E, Blomen VA, Velds A, Kerkhoven RM, Carette JE, Topaloglu H, Meinecke P, Wessels MW, Lefeber DJ, Whelan SP, van Bokhoven H, Brummelkamp TR. 2013. Deciphering the glycosylome of dystroglycanopathies using haploid screens for lassa virus entry. Science 340:479-83.

37. Gallagher P, Henneberry J, Wilson I, Sambrook J, Gething MJ. 1988. Addition of carbohydrate side chains at novel sites on influenza virus hemagglutinin can modulate the folding, transport, and activity of the molecule. J Cell Biol 107:2059-73.

38. Tsuchiya E, Sugawara K, Hongo S, Matsuzaki Y, Muraki Y, Li ZN, Nakamura K. 2002. Effect of addition of new oligosaccharide chains to the globular head of influenza A/H2N2 virus haemagglutinin on the intracellular transport and biological activities of the molecule. J Gen Virol 83:1137-46.

39. Paal T, Brindley MA, St Clair C, Prussia A, Gaus D, Krumm SA, Snyder JP, Plemper RK. 2009. Probing the spatial organization of measles virus fusion complexes. J Virol 83:10480-93.

40. Zavorotinskaya T, Albritton LM. 1999. A hydrophobic patch in ecotropic murine leukemia virus envelope protein is the putative binding site for a critical tyrosine residue on the cellular receptor. J Virol 73:10164-72.

41. Apte-Sengupta S, Navaratnarajah CK, Cattaneo R. 2013. Hydrophobic and charged residues in the central segment of the measles virus hemagglutinin stalk mediate transmission of the fusion-triggering signal. J Virol 87:10401-4.

42. Bae Y, Kingsman SM, Kingsman AJ. 1997. Functional dissection of the Moloney murine leukemia virus envelope protein gp70. J Virol 71:2092-9.

43. Wang WK, Dudek T, Essex M, Lee TH. 1999. Hypervariable region 3 residues of HIV type 1 gp120 involved in CCR5 coreceptor utilization: therapeutic and prophylactic implications. Proc Natl Acad Sci U S A 96:4558-62.

44. Radoshitzky SR, Longobardi LE, Kuhn JH, Retterer C, Dong L, Clester JC, Kota K, Carra J, Bavari S. 2011. Machupo virus glycoprotein determinants for human transferrin receptor 1 binding and cell entry. PLoS One 6:e21398.

45. Johnson DE, Ostrowski P, Jaumouille V, Grinstein S. 2016. The position of lysosomes within the cell determines their luminal pH. J Cell Biol 212:677-92.

46. Cosset FL, Marianneau P, Verney G, Gallais F, Tordo N, Pecheur EI, ter Meulen J, Deubel V, Bartosch B. 2009. Characterization of Lassa virus cell entry and neutralization with Lassa virus pseudoparticles. J Virol 83:3228-37.

47. Klewitz C, Klenk HD, ter Meulen J. 2007. Amino acids from both N-terminal hydrophobic regions of the Lassa virus envelope glycoprotein GP-2 are critical for pH-dependent membrane fusion and infectivity. J Gen Virol 88:2320-8.

48. Andersen KG, Shapiro BJ, Matranga CB, Sealfon R, Lin AE, Moses LM, Folarin OA, Goba A, Odia I, Ehiane PE, Momoh M, England EM, Winnicki S, Branco LM, Gire SK, Phelan E, Tariyal R, Tewhey R, Omoniwa O, Fullah M, Fonnie R, Fonnie M, Kanneh L, Jalloh S, Gbakie M, Saffa S, Karbo K, Gladden AD, Qu J, Stremlau M, Nekoui M, Finucane HK, Tabrizi S, Vitti JJ, Birren B, Fitzgerald M, McCowan C, Ireland A, Berlin AM, Bochicchio J, Tazon-Vega B, Lennon NJ, Ryan EM, Bjornson Z, Milner DA, Jr., Lukens AK, Broodie N, Rowland M, Heinrich M, Akdag M, et al. 2015. Clinical Sequencing Uncovers Origins and Evolution of Lassa Virus. Cell 162:738-50.

49. Kunz S. 2009. Receptor binding and cell entry of Old World arenaviruses reveal novel aspects of virus-host interaction. Virology 387:245-9.

50. Sullivan BM, Emonet SF, Welch MJ, Lee AM, Campbell KP, de la Torre JC, Oldstone MB. 2011. Point mutation in the glycoprotein of lymphocytic choriomeningitis virus is necessary for receptor binding, dendritic cell infection, and long-term persistence. Proc Natl Acad Sci U S A 108:2969-74.

51. Sevilla N, Kunz S, Holz A, Lewicki H, Homann D, Yamada H, Campbell KP, de La Torre JC, Oldstone MB. 2000. Immunosuppression and resultant viral persistence by specific viral targeting of dendritic cells. J Exp Med 192:1249-60.

52. Kunz S, Sevilla N, Rojek JM, Oldstone MB. 2004. Use of alternative receptors different than alpha-dystroglycan by selected isolates of lymphocytic choriomeningitis virus. Virology 325:432-45.

53. Teng MN, Borrow P, Oldstone MB, de la Torre JC. 1996. A single amino acid change in the glycoprotein of lymphocytic choriomeningitis virus is associated with the ability to cause growth hormone deficiency syndrome. J Virol 70:8438-43.

54. Smelt SC, Borrow P, Kunz S, Cao W, Tishon A, Lewicki H, Campbell KP, Oldstone MB. 2001. Differences in affinity of binding of lymphocytic choriomeningitis virus strains to the cellular receptor alpha-dystroglycan correlate with viral tropism and disease kinetics. J Virol 75:448-57.

55. Ono N, Tatsuo H, Hidaka Y, Aoki T, Minagawa H, Yanagi Y. 2001. Measles viruses on throat swabs from measles patients use signaling lymphocytic activation molecule (CDw150) but not CD46 as a cellular receptor. J Virol 75:4399-401.

56. Robinson JE, Hastie KM, Cross RW, Yenni RE, Elliott DH, Rouelle JA, Kannadka CB, Smira AA, Garry CE, Bradley BT, Yu H, Shaffer JG, Boisen ML, Hartnett JN, Zandonatti MA, Rowland MM, Heinrich ML, Martinez-Sobrido L, Cheng B, de la Torre JC, Andersen KG, Goba A, Momoh M, Fullah M, Gbakie M, Kanneh L, Koroma VJ, Fonnie R, Jalloh SC, Kargbo B, Vandi MA, Gbetuwa M, Ikponmwosa O, Asogun DA, Okokhere PO, Follarin OA, Schieffelin JS, Pitts KR, Geisbert JB, Kulakoski PC, Wilson RB, Happi CT, Sabeti PC, Gevao SM, Khan SH, Grant DS, Geisbert TW, Saphire EO, Branco LM, Garry RF. 2016. Most neutralizing human monoclonal antibodies target novel epitopes requiring both Lassa virus glycoprotein subunits. Nat Commun 7:11544.

57. Lefrancois L, Lyles DS. 1982. The interaction of antibody with the major surface glycoprotein of vesicular stomatitis virus. I. Analysis of neutralizing epitopes with monoclonal antibodies. Virology 121:157-67.

58. Whitt MA. 2010. Generation of VSV pseudotypes using recombinant DeltaG-VSV for studies on virus entry, identification of entry inhibitors, and immune responses to vaccines. J Virol Methods 169:365-74.

59. Imperiali M, Thoma C, Pavoni E, Brancaccio A, Callewaert N, Oxenius A. 2005. O Mannosylation of alpha-dystroglycan is essential for lymphocytic choriomeningitis virus receptor function. J Virol 79:14297-308.

CHAPTER 4

EBOLA VIRUS REQUIRES PHOSPHTIDYLSERINE SCRAMBLING ACTIVITY FOR EFFICIENCT BUDDING AND OPTIMAL INFECTIVITY[2]

[2] Acciani MD, Lay Mendoza MF, Havranek KE, et al. Ebola Virus Requires Phosphatidylserine Scrambling Activity for Efficient Budding and Optimal Infectivity. *J Virol*. 2021;95(20): e0116521. doi:10.1128/JVI.01165-21. Reprinted here with permission of the publisher.

Abstract

Ebola virus (EBOV) attaches to target cells using two categories of cell surface receptors, C-type lectins and phosphatidylserine (PS) receptors. PS receptors typically bind to apoptotic cell membrane PS and orchestrate the uptake and clearance of apoptotic debris. Many enveloped viruses also contain exposed PS and can therefore exploit these receptors for cell entry. Viral infection can induce PS externalization in host cells, resulting in increased outer PS levels on budding virions. Scramblase enzymes carry out cellular PS externalization, thus, we targeted these proteins in order to manipulate viral envelope PS levels. We investigated two scramblases previously identified to be involved in EBOV PS levels, transmembrane protein 16F and Xk-related protein 8 (XKR8), as possible mediators of cellular and viral envelope surface PS levels during the replication of recombinant vesicular stomatitis virus containing its native glycoprotein (rVSV/G) or the EBOV glycoprotein (rVSV/EBOV-GP). We found that rVSV/G and rVSV/EBOV-GP virions produced in XKR8 knockout cells contain decreased levels of PS on their surfaces, and the PS-deficient rVSV/EBOV-GP virions are 70% less efficient at infecting cells through PS receptors. We also observed reduced rVSV and EBOV virus-like particle (VLP) budding in ΔXKR8 cells. Deleting XKR8 in HAP1 cells reduced rVSV/G and rVSV/EBOV-GP budding by 60% and 65% respectively, and reduced Ebola VLP budding more than 60%. We further demonstrated that caspase cleavage of XKR8 is required to promote budding. This suggests that XKR8, in addition to mediating virion PS levels, may also be critical for enveloped virus budding at the plasma membrane.

Importance

Within the last decade, countries in western and central Africa have experienced the most widespread and deadly Ebola outbreaks since the virus was identified in 1976. While outbreaks are primarily attributed to zoonotic transfer events, new evidence is emerging that outbreaks may be caused by a combination of spillover events and viral latency or persistence in survivors. The possibility that Ebola can remain dormant then re-emerge in survivors highlights the critical need to prevent the virus from entering and establishing infection in human cells. Thus far, host-cell scramblases TMEM16F and XKR8 have been implicated in Ebola envelope surface phosphatidylserine (PS) and cell entry using PS receptors. We assessed the contributions of these proteins using CRISPR knockout cells and two EBOV models: rVSV/EBOV-GP and EBOV VLPs. We observed that XKR8 is required for optimal EBOV envelope PS levels and infectivity, and particle budding across all viral models.

Introduction

Ebola virus (EBOV) is an enveloped, non-segmented, negative-sense RNA filovirus that can cause severe hemorrhagic fever disease in those infected. Africa has endured multiple devastating EBOV outbreaks since the virus's identification in 1976 (1). While there are two licensed EBOV vaccines, rVSV-ZEBOV-GP (Merck) and Ad26.ZEBOV/MVA-BN-Filo (Janssen), Ebola outbreaks continue to occur and spread (2). With case fatality rates historically reaching up to 90%, continuous virus reemergence, and evidence of viral persistence in EBOV survivors, the risk of further high-mortality-associated EBOV outbreaks remains (3, 4).

EBOV transmission occurs via direct contact of the virus with broken skin or mucous membranes, where virions encounter their initial target cell types, myeloid dendritic cells and macrophages (5, 6). EBOV enters these cells through a dynamin-dependent macropinocytosis pathway (7, 8), followed by cathepsin-EBOV glycoprotein (GP) proteolysis, GP interaction with endosomal receptor Niemann–Pick C1 (NPC1), and virus-cell membrane fusion within the endosome (9, 10). EBOV's broad cell tropism has been attributed, in part, to its use of a variety of cell-surface receptors. C-type lectins, T-cell immunoglobulin and mucin domain (TIM) proteins, and Tyro-3/Axl/Mer (TAM) receptor tyrosine kinases can facilitate EBOV cell-surface attachment and internalization (11-17). TIM and TAM family proteins share a common ligand, an anionic phospholipid with a serine head group called phosphatidylserine (PS). Professional and non-professional phagocytes expressing TIMs or TAMs use these receptors to detect and clear apoptotic bodies, which are rich in outer leaflet PS. Viral envelopes can also contain outer leaflet PS, and therefore viruses can gain access to cells by binding to their PS receptors, an entry strategy referred to as apoptotic mimicry (18). Several studies have confirmed the importance of apoptotic mimicry in EBOV (13-19), Lassa virus (20-22), dengue virus (19, 25-27), Zika virus (23), and vaccinia virus (24) target cell attachment and internalization in vitro. Groups examining EBOV pathogenesis in $TIM^{-/-}$ mice also found TIM1 to be critical for viral loads in the liver, kidneys, spleen, and lymph nodes, and serum cytokine induction, which are characteristic of human EBOV infection (25, 26).

Enveloped viruses obtain PS from host cells during viral budding, wherein virions are enshrouded in a portion of lipid bilayer from an internal organelle membrane or the

plasma membrane (27-30). In healthy cells, plasma membrane phospholipid distribution is highly asymmetric, with the majority of PS restricted to the inner leaflet (31). Because this orientation would be unfavorable for PS receptor engagement if incorporated onto the viral envelope, it has been suggested that viral infection induces host-cell phospholipid scrambling, resulting in viral progeny with envelopes rich in externalized PS (18, 32). Several groups have reported PS externalization in wild-type (WT) EBOV-infected Huh7 cells (33), CD14+ monocytes, CD4+ T cells, and CD8+ T cells (34), in HEK293T and Cos-7 cells producing Ebola matrix protein (VP40) (27, 35), and in Vero E6 cells producing VP40 and GP (36). Interestingly, *inner* leaflet PS is required for VP40 plasma membrane localization and particle assembly and egress. VP40 dimers directly bind to inner leaflet PS, resulting in higher order oligomers with increased stability that form the matrix layer of the particle (27). Therefore, it was proposed that PS scrambling occurs after VP40 oligomerization, generating a positive plasma membrane curvature that promotes the egress of newly assembled particles. The mechanism by which this intricately timed PS scrambling is achieved, however, is unknown.

Disruptions in plasma membrane or internal membrane PS asymmetry are mediated by transmembrane scramblases that nonspecifically transfer phospholipids between leaflets of the bilayer (37). While specific scramblase proteins have only recently been identified, studies have already linked several of these proteins to enveloped virus replication. For example, ER scramblase transmembrane protein 41B (TMEM41B) (38, 39) was shown to be integral for the formation of flavivirus and coronavirus replication complexes on the ER (40, 41). Plasma membrane scramblase TMEM16F facilitates envelope-membrane fusion for HIV-1 and SARS-CoV2 (42, 43).

Furthermore, TMEM16F and Xk-related protein 8 (XKR8, another plasma membrane scramblase) have both been implicated in EBOV infectivity via apoptotic mimicry.

Of all the identified proteins demonstrating phospholipid scramblase activity at the plasma membrane, TMEM16F and XKR8 are the most well-characterized (44). TMEM16F, a member of the TMEM16 family of chloride channels and scramblases, activity is stimulated by large increases in cellular cytosolic calcium and is reversible (45-48), whereas XKR8 is permanently activated during apoptosis via caspase-3/7 cleavage (49-51). In recent publications by Nanbo et al. (36) and Younan et al. (33), the authors proposed that XKR8 or TMEM16F is required for EBOV-induced cellular PS scrambling, EBOV envelope surface PS acquisition, and EBOV infectivity. Younan et al. observed widespread calcium-induced TMEM16F-dependent cellular PS scrambling in Huh7 cells following WT EBOV infection. While knocking down TMEM16F reduced EBOV surface PS and virus cell–cell spread, knocking down XKR8 did not inhibit EBOV-induced PS scrambling. Alternatively, Nanbo et al. attributed Ebola virus-like particle (VLP) envelope PS levels and VLP internalization efficiency to XKR8 activation. This group further suggested that the expression of EBOV VP40 and GP proteins at the plasma membrane of Vero E6 cells induces caspase cleavage and XKR8-mediated PS scrambling at EBOV VLP budding sites. They did not investigate TMEM16F in their study.

In this study, we sought to clarify the contributions of TMEM16F and XKR8 to EBOV envelope surface PS levels by producing recombinant vesicular stomatitis viruses expressing native glycoprotein (rVSV/G) or the Zaire EBOV glycoprotein (rVSV/EBOV-GP) in human haploid (HAP1) cells knocked-out for TMEM16F (ΔTMEM16F) and

XKR8 (ΔXKR8). rVSV/EBOV-GP cell–cell spread, virion infectivity, and viral envelope PS levels were reduced when the virus was produced in ΔXKR8 cells. While deleting XKR8 also reduced rVSV/G envelope PS levels, this did not impact virion infectivity. We also observed a glycoprotein-independent reduction in rVSV budding by 60% in ΔXKR8 cells, leading us to examine the relationship between EBOV VLP budding and XKR8. We found that caspase-cleaved XKR8-mediated PS scrambling promotes efficient VLP budding in HAP cells. Specific XKR8 activity was not required because activation of calcium dependent scramblases could rescue budding activity in cells lacking XKR8. Therefore, we propose that PS scrambling is needed not only for viral surface PS, but also for viral particle assembly and/or egress.

Results

XKR8 is required for apoptosis-induced PS externalization in HAP1 cells. HAP1 cells have been used to screen and identify cellular genes critical for EBOV entry (9, 52). In order to investigate the specific contributions of TMEM16F and XKR8 scramblases to EBOV replication, ΔTMEM16F and ΔXKR8 knockout HAP1 cell lines were first tested for scramblase activity. XKR8 is activated during apoptosis by caspase cleavage; therefore, we infected parental and knockout cells with rVSV/G, a strong apoptosis inducer (53, 54), and stained for PS in the outer leaflet using an AnnexinV-PacificBlue conjugate (AnV-PacBlue) (Fig. 1A and B). Virus-infected HAP1 and ΔTMEM16F cells showed a marked increase in surface PS, whereas uninfected and infected ΔXKR8 surface PS levels were similarly low, indicating that XKR8 is the primary mediator of apoptosis-induced PS scrambling in HAP1 cells. We also treated HAP1 cell lines with calcium ionophore A23187 to test for calcium-dependent

scramblase activity (Fig. 1A and B). A23187 treatment resulted in higher AnV fluorescence in all three cell lines, indicating that both scramblase-deficient cells retain calcium-mediated PS scrambling activity. We performed immunoblot analysis on cell lysates and confirmed that TMEM16F protein was not detected in ΔTMEM16F cells (Fig. 1C). Thus, while XKR8 is a primary mediator of apoptosis-induced PS externalization, TMEM16F is not essential for calcium-induced PS externalization in HAP1 cells.

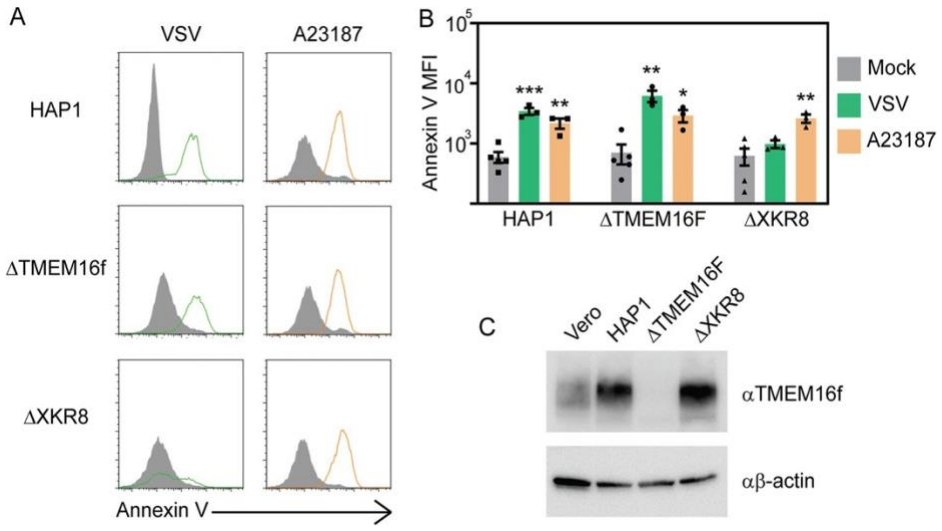

Fig 1. PS scrambling abilities of WT and knockout (KO) HAP1 cells. HAP1, DTMEM16F, and DXKR8 cells were infected with rVSV/G for 16 h or treated with a calcium ionophore A23187 (5 mM) for 5 min, double stained with AnV-PacBlue and PI, and analyzed using a BD LSRII flow cytometer. Anv-PacBlue fluorescence of live, single, nonnecrotic cells is shown as (A) histograms and (B) average mean fluorescence intensities (MFIs). (C) Immunoblot probing for b-actin and TMEM16F confirming the absence of TMEM16F in DTMEM16F cells. The values shown are averages from at least three independent experiments ± SEM. *, $P < 0.05$, **, $P < 0.01$, and ***, $P < 0.001$, by Student's t test.

rVSV/EBOV-GP replication is impaired in ΔXKR8 cells. In order to elucidate the importance of scramblases in EBOV-GP-mediated replication, we performed multistep replication curves using rVSV encoding EBOV-GP (rVSV/EBOV-GP) or its native glycoprotein (rVSV/G), as well as measles virus (MeV) in parental and knockout

HAP1 cell lines (Fig. 2). The entry pathways of both rVSV/G and MeV are initiated by specific cell surface protein interactions and are not strongly associated with apoptotic mimicry (13, 55-57). All viruses were titrated on Vero-hSLAM cells that naturally produce PS receptors (TIM-1 and Axl) as well as MeV and rVSV-G receptors, but do not produce EBOV-enhancing C-type lectins (58, 59). Titers of rVSV/EBOV-GP produced in ΔXKR8 cells were significantly reduced compared to titers generated in HAP1 and ΔTMEM16f cells at most time points following infection (Fig 2A). The greatest differences occurred 72 hours post-infection, where we observed a 4.6-log reduction of infectious virions present in ΔXKR8 cell supernatant. However, by day 5 of infection, ΔXKR8 cells produced similar levels of rVSV/EBOV-GP virus, suggesting that EBOV-GP-mediated replication is significantly delayed rather than strictly inhibited in these cells. rVSV/G and MeV spread similarly in all cell types (Fig. 2B and C), suggesting that cells lacking XKR8 scrambling activity are uniquely defective in entry or spread of particles utilizing EBOV-GP for entry. Because we did not detect a functional defect in ΔTMEM16F cells with AnV staining, it was unsurprising that all viruses were able to propagate in these cells as efficiently as parental HAP1 cells.

In order to visualize rVSV/EBOV-GP cell–cell spread in HAP1 and ΔXKR8 cells, we infected cells and monitored the cellular production of virus-encoded GFP via fluorescence microscopy (Fig. 2D and E). The earliest time points after infection revealed comparable numbers of GFP-producing (GFP+) cells, suggesting that the initial entry of rVSV/EBOV-GP viral stock into ΔXKR8 cells was uninhibited. However, we observed fewer GFP+ rVSV/EBOV-GP-infected ΔXKR8 cells over time (particularly at 24- and 48-hours following infection), indicating a cell-cell spread defect (Fig. 2D). Late in

infection, the level of GFP+ ΔXKR8 cells reached those of HAP1 cells, mirroring the recovery of viral replication seen in the viral titers (Fig. 2A). As expected, rVSV/G propagated through HAP1 and ΔXKR8 cells with similar efficiencies as was demonstrated by no detectable differences in the level of GFP+ cells in either cell type (Fig 2E).

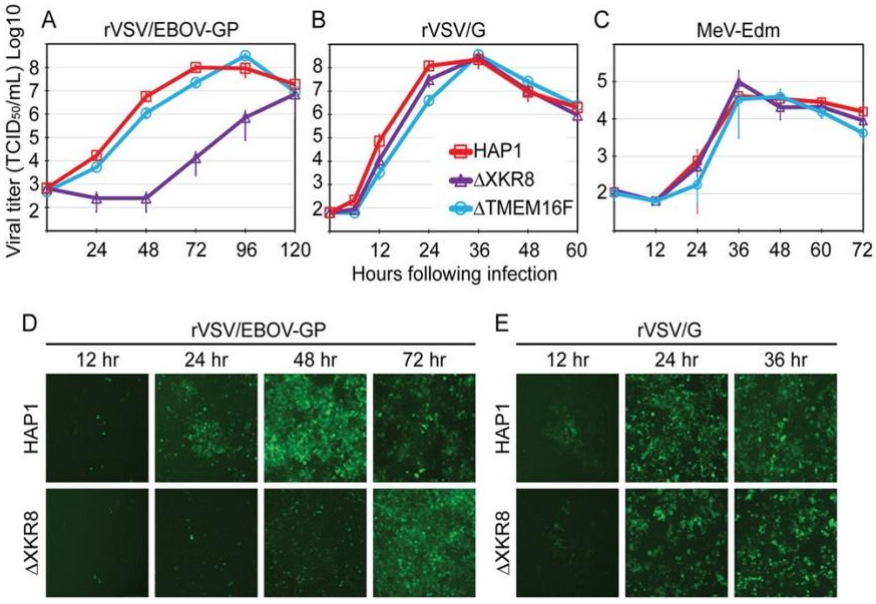

Fig 2. rVSV/EBOV-GP replication and cell-cell spread are delayed in cells lacking XKR8. HAP1, ΔTMEM16F, and ΔXKR8 cells were infected with rVSV/EBOV-GP (A), rVSV/G (B), or MeV (C). Cell supernatants (A and B) or cell- associated virus (C) was collected at the indicated time points and titrated on Vero cells. The values shown are the average $\log_{10}$ $TCID_{50}$/mL from at least three independent experiments ± SEM. To observe cell-cell viral spread, cells were infected with rVSV/EBOV-GP (D) or rVSV/G (E), and viral spread was monitored by GFP fluorescence over time. Three representative images were taken at the indicated time points (magnification, x20).

Knocking out XKR8 does not inhibit viral entry or genome replication. The rVSV/EBOV-GP replication delay observed in ΔXKR8 cells could be caused by inefficiencies at a number of steps in the virus replication cycle. Because the phenotype correlated exclusively with EBOV-GP, we first examined the ability of ΔXKR8 cells to support rVSV/EBOV-GP entry. XKR8 is inactive in homeostatic cells, therefore we did

not expect XKR8 deletion to impact early stages in the viral replication cycle. We quantified rVSV/EBOV-GP viral genomes internalized within HAP1 and ΔXKR8 cells following a 2-hour entry period (Fig. 3A). We also infected cells with rVSV/EBOV-GP and measured the proportion of GFP-producing cells after one round of replication (Fig. 3B). We were unable to detect significant differences in genomes internalized into the cells (Fig. 3A), and we observed a slightly higher number of GFP positive cells (Fig. 3B) when cells were lacking XKR8.

We next assessed the ability of ΔXKR8 cells to support viral replication. While initial entry and fusion of our rVSV particles is facilitated by PS and/or the viral glycoprotein, the remaining steps in the viral replication cycle are mediated solely by VSV machinery. Because rVSV/G replication was only slightly impacted by XKR8 deletion (Fig 2B), we did not expect differences in post-entry replication efficiencies in ΔXKR8 cells. We quantified RNA copy numbers in cell lysates 12 hours following rVSV/G or rVSV/EBOV-GP infection and observed no significant differences in the number of RNA genomes and transcripts produced by either cell line (Fig. 3C).

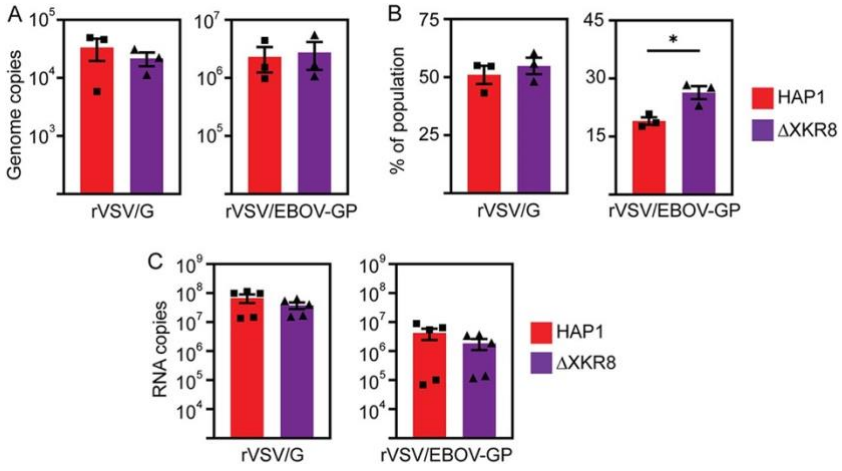

Fig 3. XKR8 is not required for rVSV/EBOV-GP entry or replication. (A) HAP1 and ΔXKR8 cells were infected with rVSV/G or rVSV/EBOV-GP. After 2 h,

early viral entry was determined by quantifying the number of viral genomes within the cell lysate using qRT-PCR. (B) rVSV/G and rVSV/EBOV-GP entry was assessed by counting the number of cells producing the virally encoded GFP reporter by flow cytometry. Cells were infected with rVSV/G or rVSV/EBOV-GP for 12 h, after which cells were harvested, fixed, and analyzed for GFP fluorescence. To assess viral replication, cells were infected with rVSV/G or rVSV/EBOV-GP, and viral RNA was quantified in the cell lysates 12 h (rVSV/G) or 24 h (rVSV/EBOV-GP) post infection. The values shown are averages from at least three independent experiments ± SEM. *, $P < 0.05$ by Student's t test.

ΔXKR8 cells decrease rVSV budding efficiency. The final step in rVSV replication is virion budding at the plasma membrane, resulting in cell-free infectious particles. We produced rVSV virions containing nano-luciferase by cloning nano-luciferase into the VSV matrix protein (MnLuc). These MnLuc particles can be easily quantified, and the ratio of particles released into the cell supernatants versus those inside each cell line can be compared to determine budding efficiency. As shown in Fig 4A, ΔXKR8 cells released approximately 60% fewer rVSV-MnLuc/G and rVSV-MnLuc/EBOV-GP particles into the supernatant. Using immunoblot analysis, we observed similar viral protein levels in parental and ΔXKR8 cell lysates after one round of replication; however, the levels of VSV-M present in the supernatant further suggested that rVSV particle budding in ΔXKR8 cells is inefficient (Fig. 4B).

In order to visualize budding of rVSV/EBOV-GP or rVSV/G particles, we performed transmission electron microscopy (TEM) on infected HAP1 (Fig. 4C and D) and ΔXKR8 (Fig. 4E and F) cells. We did not observe any morphological differences in rVSV particles budding from cells with or without XKR8. While it was consistently difficult to locate rVSV budding events in HAP1 cells, presumably because particles were quickly released into cell supernatant, we found many particles near or emerging from ΔXKR8 cell plasma membranes. In many instances, it appeared that budded

particles were immobilized on the surface of the ΔXKR8 cells. Previous work find a defect in late-stage VSV particle release presents similarly in TEM (60-62). While we did not observe an obvious defect in particle-membrane fission, more detailed imaging is needed to confirm whether the particles remaining on the surface of ΔXKR8 cells have completely separated from the plasma membrane. Despite evidence of decreased viral budding in the absence of XKR8, this defect only slightly altered rVSV/G replication in ΔXKR8 cells (Fig. 2B); thus, defective budding does not completely account for the dramatic EBOV-GP-specific replication delay (Fig 2A).

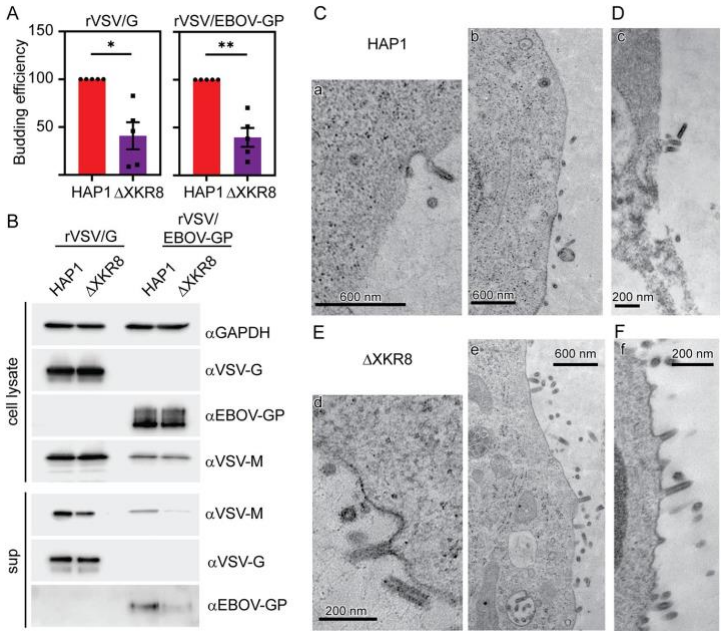

Fig 4. XKR8 is required for efficient rVSV budding. (A) Cells were infected with rVSV-MnLuc/G or rVSV-MnLuc/ EBOV-GP for 12 h, after which cell lysate and supernatant nano-luciferase (nLuc) activity was measured. Budding efficiency was calculated by dividing supernatant nLuc activity by lysate nLuc activity, and values were normalized to HAP1 budding efficiency. The values shown are averages from five independent experiments ± SEM. *, $P < 0.05$, and **, $P < 0.01$, by Student's t test. (B) Immunoblot probing for VSV-M and VSV-G or EBOV- GP in rVSV/G- or rVSV/EBOV-GP-infected HAP1 and ΔXKR8 cell lysates and supernatants after one round of replication. GAPDH levels are shown as a cell lysate loading control. (C to F) Transmission electron microscopy analysis of rVSV/EBOV-GP particles budding from the surfaces of HAP1 cells (C) or ΔXKR8 cells (E) and rVSV/G particles budding from the surfaces of HAP1 cells (D) or ΔXKR8 cells (F). Images in panels C to F were

captured at the following magnifications: 6,000x (a), 5,000x (b), 12,000x (c), 15,000x (d), 6,000x (e), and 15,000x (f).

ΔXKR8-produced rVSV/EBOV-GP virions are less infectious and contain lower levels of PS. We hypothesized that rVSV/EBOV-GP cell-to-cell spread was delayed in ΔXKR8 cells due to low levels of virion surface PS, which would decrease particle infectivity due to a lack of affinity for PS receptors. In order to address infectivity, we produced rVSV/G and rVSV/EBOV-GP in parental and ΔXKR8 cells and compared the number of viral genomes to the number of plaque-forming units in each sample (Fig. 5A and B). This ratio determines the number of viral genomes required to produce one plaque; therefore, a lower genome:PFU value means particles are more infectious, whereas high values suggest that many more viral particles are required to establish infection. The rVSV/G genome:PFU ratio was unaffected by the absence of XKR8; for approximately every 30 particles detected via qPCR, one particle was infectious (Fig. 5B). For rVSV/EBOV-GP, 1 in 111 HAP1-made particles were infectious, and only 1 in 380 ΔXKR8-made particles were infectious, a 3.4-fold reduction in infectivity. rVSV/EBOV-GP particles were generally not as infectious as rVSV/G particles, which may be attributed to less efficient incorporation of non-native EBOV-GP into VSV particles.

In order to confirm that viral particles produced in ΔXKR8 cells contain lower levels of outer leaflet PS, we coated latex beads with rVSV particles produced in parental and ΔXKR8 cells and examined viral envelope AnV-PacBlue fluorescence intensity using flow cytometry (Fig 5C-E). Incubating beads with 1.5×10^9 genomes of rVSV/G or rVSV/EBOV-GP ensured that beads were uniformly and completely coated in viral particles, indicated by robust G or GP staining (Fig. 5C and D). Producing rVSV in

ΔXKR8 cells significantly reduced outer leaflet PS levels in a glycoprotein-independent manner, resulting in an approximately two-fold decrease in the AnV mean fluorescence intensity on rVSV/G particles and a three-fold decrease on rVSV/EBOV-GP particles (Fig. 5E).

Because we observed slightly lower levels of EBOV GP immunofluorescence on beads coated in ΔXKR8-made rVSV/EBOV-GP (Fig 5D), we further analyzed virions for GP incorporation using immunoblot analysis and densitometry (Fig 5F). Supernatant VSV genome copy numbers were quantified using qRT-PCR, and equivalent genome copies were concentrated and probed for VSV M and EBOV GP. We found some evidence that ΔXKR8 cells may produce particles that incorporate more GP, although not significant (P=0.1529), thus we did not attribute the reduction in ΔXKR8-made rVSV/EBOV-GP infectivity to lower GP levels. The differences in rVSV EBOV-GP incorporation observed in the flow cytometry and immunoblot assays may be due to distinct primary antibodies used to detect GP in flow cytometry versus immunoblotting. In order to demonstrate that reduced rVSV/EBOV-GP infectivity was the direct result of decreased PS content in the ΔXKR8-made viral envelopes, we passaged the viruses generated in Fig. 5A in Vero cells and determined the genome:PFU ratio of the viral progeny (Fig. 6A and B). The rVSV/G and rVSV/EBOV-GP progeny genome:PFU ratios were similar with respect to viral GP after Vero passage, regardless of the original producing cell lines. These data support our hypothesis that host-cell scramblase deletion reduces rVSV/EBOV-GP infectivity due to alterations in the viral envelope and that these alterations are irrelevant for rVSV/G, a virus that does not utilize apoptotic mimicry.

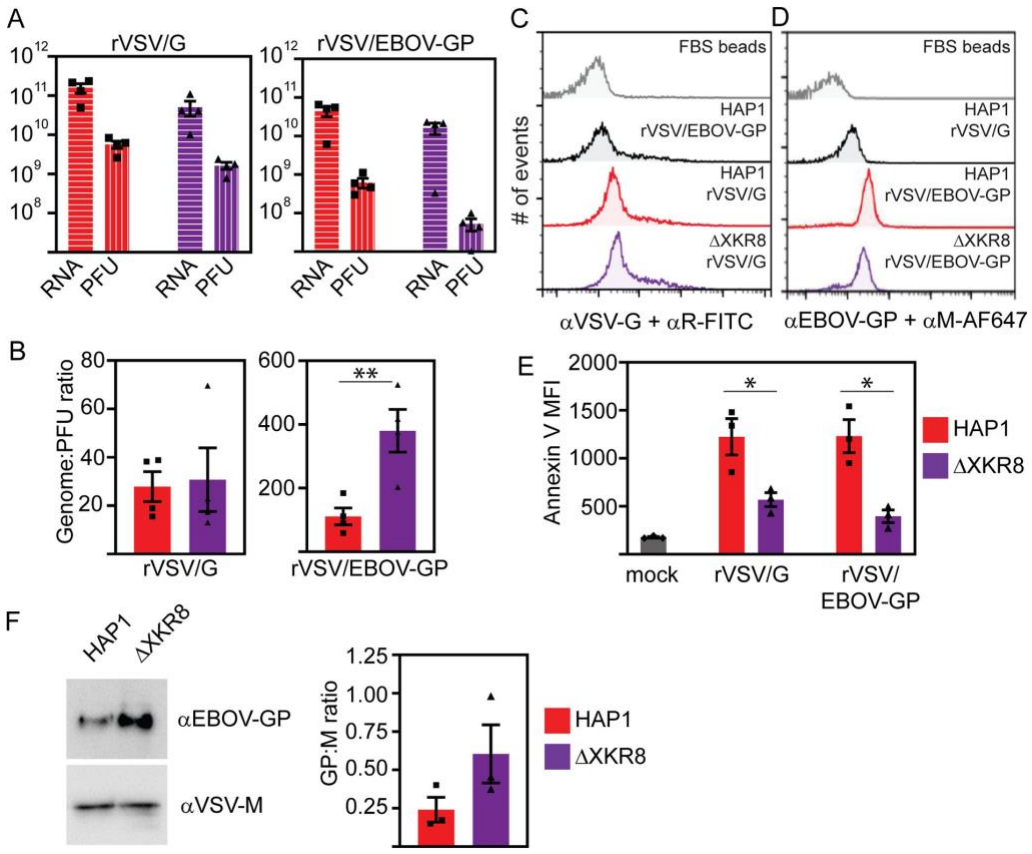

Fig 5. Knocking out XKR8 reduces rVSV/EBOV-GP infectivity and PS levels. (A) rVSV/G and rVSV/EBOV-GP were propagated in HAP1 and ΔXKR8 cells for 24 h. Supernatants were collected, concentrated, and titrated via plaque assay, and viral genomes were quantified by qRT- PCR. (B) Viral genome/PFU ratios were determined by calculating the ratio of viral genome copy numbers to infectious particle numbers (PFU/mL) for each sample. (C to E) Equal amounts of rVSV/G and rVSV/EBOV-GP particles produced in HAP1 and ΔXKR8 cells were bound to aldehyde-sulfate latex beads and immunostained for VSV-G (C) or EBOV-GP (D). E) Viral particles were stained for surface PS levels with AnV-PacBlue, and MFIs were quantified. (F) Equivalent genome copies of rVSV/EBOV-GP particles produced by HAP1 and ΔXKR8 cells were TCA precipitated and analyzed for VSV-M and EBOV-GP protein content by immunoblot. Ratios of EBOV-GP to VSV-M were quantified using densitometry analysis. The values shown are averages from at least three independent experiments ± SEM. *, $P < 0.05$, and **, $P < 0.01$, by Student's t test.

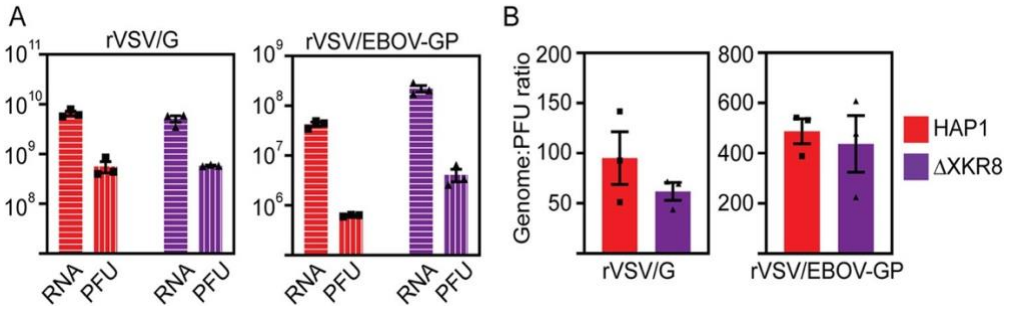

Fig 6. rVSV/EBOV-GP infectivity is restored following one passage in Vero cells. HAP1-made or ΔXKR8-made rVSV/G or rVSV/EBOV-GP virus examined in Fig. 5A and B was passaged once in Vero cells. (A) After 24 h, supernatants were collected and titrated via plaque assay. Viral genomes were quantified by qRT-PCR. (B) Viral genome/PFU ratios were determined by calculating the ratio of viral genome copy numbers to infectious particle numbers (PFU/ml) for each sample. The values shown are averages from at least three independent experiments ± SEM.

XKR8 promotes efficient EBOV VLP budding. We next investigated the role of XKR8 in EBOV replication using Ebola virus-like particles (VLPs), which are morphologically similar to authentic EBOV and can be generated when cells produce Ebola matrix (VP40), glycoprotein (GP), and nucleoprotein (NP) (63). Nanbo et al previously demonstrated that EBOV VLPs made in XKR8-knockdown HEK293T cells contain less surface PS and are internalized into Vero-E6 cells less efficiently (36). Therefore, we sought to determine if EBOV VLP budding would be similarly inhibited in the absence of XKR8 as was observed with rVSV/EBOV-GP in Fig 4. We produced VLP components in HAP1 and ΔXKR8 cells and probed lysates and pelleted VLPs for VP40 to monitor VLP budding efficiency (Fig. 7A). While we observed prominent GP and VP40 bands in pellets from HAP1 cells, ΔXKR8 produced VLP bands were weak. Tetherin, a protein known to inhibit EBOV budding (64), was co-transfected into HAP1 to serve as a budding control, and as expected produced nearly undetectable levels of VP40 in the supernatant (Fig. 7A). To examine VLP GP incorporation, we made VLPs containing nano-luciferase tagged VP40 (nLuc-VLPs) in HAP and ΔXKR8 cells. NLuc-

VLPs were normalized using luciferase levels and then subjected to immunoblot and densitometry analysis for VP40 and EBOV GP (Fig. 7B). We did not detect a statistically significant difference in VLP GP incorporation when produced in cells with or without XKR8.

We also monitored nLuc-VLP budding efficiency by comparing luciferase levels in transfected HAP1 and ΔXKR8 cell lysates and pelleted cell supernatants (Fig. 7C). VLP budding efficiency was reduced more than 60% in ΔXKR8 cells compared to HAP1 cells, and approximately 75% in the presence of tetherin. Co-transfecting ΔXKR8 cells with VLP proteins and $XKR8_{FLAG}$ restored VLP budding in ΔXKR8 cells (Fig. 7D). We did not observe a statistically significant VLP budding enhancement by adding exogenous XKR8 to WT HAP1 cells (P=0.1493).

While production of VP40 alone is sufficient for the formation of filamentous VLPs, co-transfecting cells with EBOV GP and NP enhances VLP release (63). Therefore, we asked if GP and/or NP enhances VLP budding in an XKR8-dependent manner. HAP1 and ΔXKR8 cells were transfected with nLuc-VP40 alone or in combination with GP and/or NP, and VLP budding efficiencies were determined by monitoring released nLuc-VLPs (Fig. 7E and Table 1). Our data confirmed that VLPs budded most efficiently when VP40 is co-transfected with GP. However, we saw a similar pattern of budding enhancement in both the HAP1 and ΔXKR8 cells. VLPs budded from HAP1 cells 6- to 7-fold more efficiently than ΔXKR8 cells for every transfection condition, including cells co-transfected with SARS-CoV-2 S, indicating there is no synergistic effect of XKR8 and viral glycoproteins or EBOV NP in enhancing VLP budding.

EBOV VLPs require caspase-activated XKR8 for efficient budding. In order to mediate cell PS externalization, XKR8 must become activated by caspase-3/7 cleavage (50). Therefore, we hypothesized that EBOV proteins can trigger apoptosis in HAP1 cells, resulting in XKR8 cleavage, PS externalization, and increased VLP budding. Studies investigating EBOV-

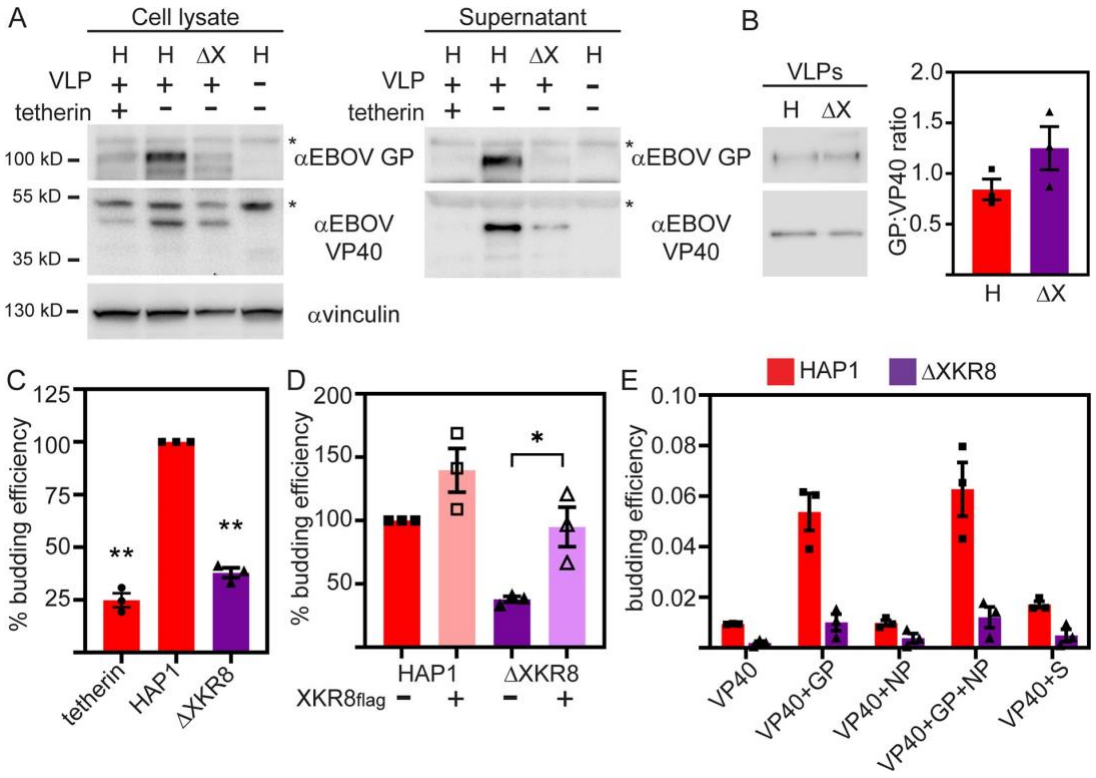

Fig 7. XKR8 enhances VLP budding. (A) HAP1 and ΔXKR8 cells were transfected with plasmids encoding EBOV VLP components NP, GP, and VP40 and plasmids encoding either tetherin or empty vector. After 48 h, lysates and pelleted supernatants were subjected to immunoblot analysis for vinculin, VP40, and GP. Asterisks (*) indicate nonspecific protein bands. (B) Supernatants from HAP1 and DXKR8 cells producing nLuc-VLPs were collected and pelleted 24 h following transfection. nLuc-VLPs were normalized using luciferase levels, denatured, and subjected to immunoblot analysis for VP40 and GP content. EBOV-GP/VP40 ratios were quantified using densitometry analysis. (C and D) HAP1 and DXKR8 cells were transfected with plasmids encoding NP, GP, and VP40-nLuc, and either tetherin (C), $XKR8_{FLAG}$ (D), or empty vector. After 24 h, VLP budding efficiencies were quantified by measuring luciferase levels in lysates and pelleted supernatants. (E) HAP1 and ΔXKR8 cells were transfected with plasmids encoding VP40-nLuc and empty vector, GP, NP, GP plus NP, or SARS-CoV-2 $S_{Met1}\Delta 21$. nLuc-VLP budding efficiencies were determined by measuring luciferase levels in cell lysates and pelleted supernatants 24 h following

transfection. The values shown are averages from at least three independent experiments ± SEM. Additional statistics are summarized in Table 1.

TABLE 1 Pairwise comparisons of VLP budding efficiency

Pairwise comparison	*P* value[a]
HAP1 vs ΔXKR8	
VP40 vs VP40	0.0005***
VP40+GP vs VP40+GP	0.0056**
VP40+NP vs VP40+NP	0.0505 (NS)
VP40+GP+NP vs VP40+GP+NP	0.0113*
VP40+S vs VP40+S	0.0117*
HAP1 vs HAP1	
VP40 vs VP40+GP	0.0038**
VP40 vs VP40+NP	0.7316 (NS)
VP40 vs VP40+GP+NP	0.0074**
VP40 vs VP40+S	0.0043**
ΔXKR8 vs ΔXKR8	
VP40 vs VP40+GP	0.0735 (NS)
VP40 vs VP40+NP	0.4062 (NS)
VP40 vs VP40+GP+NP	0.0738 (NS)
VP40 vs VP40+S	0.3152 (NS)

[a]Significance: *, $P < 0.05$, **, $P < 0.01$, and ***, $P < 0.001$, by Student's *t* test.

NS, not significant.

infected or transfected cells, however, have reported varying levels of apoptosis hallmarks including limited (36, 65) or robust (27, 33, 34) cellular PS externalization and little (65) or significant (34) caspase activation. To determine if caspase activity enhances EBOV VLP budding, we treated nLuc-VLP-producing HAP1 cells with pan-caspase inhibitor Z-VAD-FMK (Fig. 8A). Similar to the effect of deleting XKR8, VLP budding in treated HAP1 cells was reduced by 52%.

We then asked if caspase cleavage of XKR8 directly improves VLP budding. XKR8 contains a highly conserved caspase recognition site in its C-terminus, and

introducing mutations D352A and D355A to XKR8 inhibits caspase cleavage and cell PS externalization (51). Thus, we produced a caspase-resistant XKR8 plasmid, XKR8-2DA$_{FLAG}$, and examined nLuc-VLP budding in the presence or absence of proteolytically processed XKR8. We produced VLPs in ΔXKR8 cells with either XKR8$_{FLAG}$ or XKR8-2DA$_{FLAG}$, and probed cell lysates and pelleted VLPs for VP40 and full-length or cleaved XKR8 $_{FLAG}$ (Fig 8B). We confirmed the caspase-resistance of XKR8-2DA$_{FLAG}$ in VLP pellets, indicated by one full-length band at ~48kda, while a smaller ~42kda band was detected in XKR8 $_{FLAG}$ VLP pellets. We could not detected high levels of cleaved XKR8 in XKR8 $_{FLAG}$ cell lysates, which is consistent with the findings from Nanbo et al (36). Furthermore, supernatant VLP VP40 and FLAG bands were weak from cells producing XKR8-2DA$_{FLAG}$, indicating that caspase-resistant XKR8 does not support efficient VLP budding. We then measured lysate and pellet luciferase levels in nLuc-VLP-producing ΔXKR8 cells transfected with either XKR8$_{FLAG}$ or XKR8-2DA$_{FLAG}$, and found that XKR8-2DA$_{FLAG}$ did not enhance VLP budding compared to XKR8$_{FLAG}$ (Fig 8C). These data indicate that caspase-cleaved XKR8 promotes efficient VLP release from HAP1 cells.

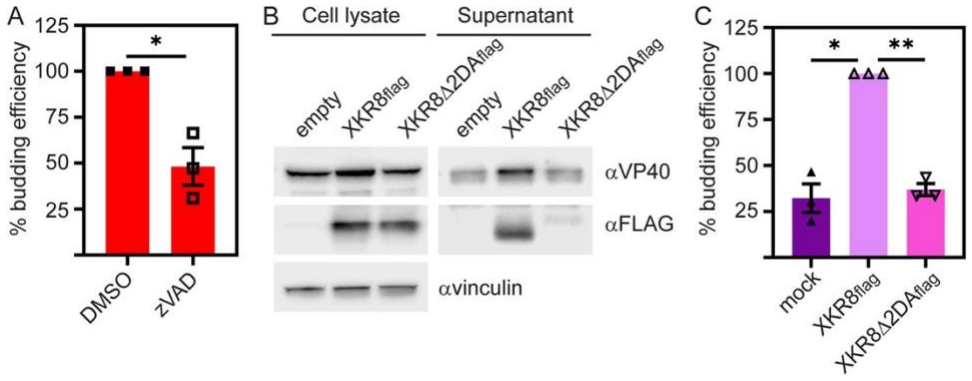

Fig 8. Caspase-cleaved XKR8 is required for VLP budding enhancement. (A) nLuc-VLPs were produced in HAP1 cells treated with DMSO or 20 μM pan-caspase inhibitor Z-VAD-FMK. nLuc-VLP budding efficiencies were determined by measuring

luciferase levels in cell lysates and pelleted supernatants 24 h following transfection. (B) ΔXKR8 cells were transfected with plasmids encoding EBOV-NP, -GP, and -VP40-nLuc, and plasmids encoding either $XKR8_{FLAG}$, caspase-resistant $XKR8(2DA)_{FLAG}$, or empty vector. After 24 h, cell lysates and pelleted supernatants were subjected to immunoblot analysis to detect VP40-nLuc and full-length (~48 kDa) or cleaved (~42 kDa) $XKR8_{FLAG}$. Vinculin levels are shown as a cell lysate loading control. (C) ΔXKR8 cells were transfected with plasmids encoding VP40-nLuc, GP, NP, and either $XKR8_{FLAG}$, $XKR8(2DA)_{FLAG}$, or empty vector for 24 h. VLP budding efficiency was quantified by measuring luciferase levels in lysates and pelleted supernatants. The values shown are averages from at least three independent experiments ± SEM. *, $P < 0.05$, and **, $P < 0.01$, by Student's t test.

PS scrambling is sufficient for VLP budding enhancement. In HAP1 cells we demonstrate that XKR8 activity is critical for apoptosis-induced PS scrambling and increases in VLP budding. To determine if XKR8-independent PS scrambling can also enhance VLP budding, we activated the TMEM16 family of scramblases in cells with or without endogenous XKR8. We treated VLP-producing HAP1 and ΔXKR8 cells with 0.5μM A23187, a compound that triggers calcium dependent PS scrambling (Fig 1), and examined VLP budding (Fig 9). Pharmacologically activating TMEM16 scramblases in ΔXKR8 cells improved VLP budding efficiency by 42%, suggesting that 1) TMEM16 scramblases are likely not endogenously activated during HAP1 VLP production and 2) PS scrambling in general, regardless of specific scramblase activation, is required for efficient VLP budding. Notably, VLP budding was still more efficient in mock-treated HAP1 cells and ΔXKR8 cells expressing exogenous $XKR8_{FLAG}$ (Fig 7D). Additionally, treating HAP1 cells with A23187 enhanced VLP budding by 204%, while over-producing XKR8 in these cells did not impact budding. Thus, caspase-activated XKR8-mediated PS scrambling strongly promotes efficient VLP budding in HAP1 cells, however, budding can be further enhanced by artificially inducing calcium-activated TMEM16 PS scramblases.

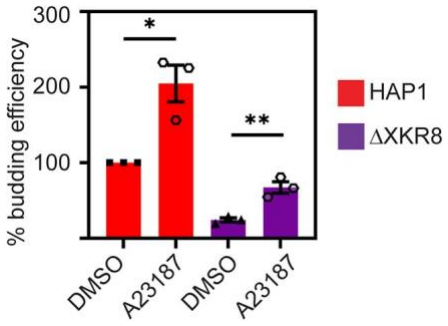

Fig 9. Pharmacological activation of PS scrambling enhances VLP budding. HAP1 and ΔXKR8 cells were transfected with plasmids encoding VP40-nLuc, GP, and NP. Twelve hours following transfection, cells were treated with 0.5 μM calcium ionophore A23187 or DMSO. After an additional 36 h, VLP budding efficiencies were quantified by measuring luciferase levels in lysates and pelleted supernatants. The values shown are averages from at least three independent experiments + SEM. * $P < 0.05$, and **, $P < 0.01$, by Student's t test.

Discussion

Although previous paradigms suggest that all viral GPs orchestrate enveloped viral attachment to host cells in a lock-and-key-like manner, evidence now suggests that less-specific mechanisms of virion attachment can be utilized to facilitate internalization. Attachment factors such as lectins and PS receptors effectively bind and internalize viral particles without specific GP interaction (8, 16, 17, 19, 25). In order to interact with cellular PS receptors, viral particles must contain PS in the outer leaflet of their envelopes. However, normal-state cells strictly sequester PS in the inner leaflet of the plasma membrane. Therefore, it has been speculated in previous works on apoptotic mimicry that viruses budding from the plasma membrane trigger cellular PS externalization through endogenous pathways, such as apoptosis, to obtain surface PS-rich viral envelopes (18, 32). To determine whether cellular scramblases, proteins required to move phospholipids between the inner and outer leaflets of cell membranes, are involved in viral PS acquisition, we monitored EBOV-GP-mediated spread in CRISPR knockout HAP1 cells deficient in XKR8 or TMEM16F scramblases. Here, we

demonstrate that XKR8, a transmembrane scramblase required for apoptotic cell PS externalization, is required for elevated PS levels on rVSV envelopes. The envelope PS levels achieved by XKR8 scrambling are also critical for rVSV/EBOV-GP infectivity. Additionally, our data suggests that caspase-cleaved activated XKR8 enhances rVSV and EBOV VLP budding. Activation of alternative cellular scramblases using small molecules rescued the budding defect observed in ΔXKR8, suggesting that PS scrambling is required for efficient VLP budding activity rather than specific incorporation of XKR8.

Previous studies confirm that VSV induces apoptosis and PS scrambling in infected cells, and that PS is detected on the viral envelope; however, the specific cellular mediator of VSV-induced PS scrambling was unknown (14, 53, 54, 66). Here we find that rVSV/G and rVSV/EBOV-GP PS levels are primarily attributed to XKR8 when viruses are produced in HAP1 cells. Our data are consistent with findings from Nanbo et al, which showed that caspase-activated XKR8 in Vero cells and Vero-made EBOV VLPs is required for increased VLP PS levels (36). Another recent study by Younan et al demonstrated that in Huh7 cells, WT EBOV activates TMEM16F via increasing intracellular calcium levels, resulting in elevated cellular and envelope surface PS (33). We did not find any cellular or viral phenotypes in HAP1ΔTMEM16F cells. HAP1 cells also produce TMEM16D, another calcium mediated scramblase which may compensate for the loss of TMEM16F. Therefore, the specific scramblase responsible for viral envelope PS may vary based on the viral model and producer cells used.

Reduced PS levels did not inhibit rVSV/G infectivity, likely because VSV-G-mediated entry proceeds primarily through VSV-G binding to LDLR (low density lipoprotein receptor), rather than PS-PS receptor binding (67). This is consistent with

several other studies showing that rVSV infection and VSV pseudoparticle transduction efficiencies are only marginally affected by the presence or absence of PS receptors both *in vitro* and *in vivo* (13, 16, 25). Alternatively, rVSV/EBOV-GP infectivity in Vero cells directly correlated to envelope PS levels, demonstrating that apoptotic mimicry more significantly contributes to EBOV-GP-mediated entry. This rVSV/EBOV-GP infectivity data aligns with those from the Younan and Nanbo groups, which both find that reducing viral envelope PS inhibits EBOV-GFP viral spread and EBOV VLP uptake in Vero E6 cells, and with numerous groups that have suggested that PS receptors are key EBOV attachment factors (13-19, 25).

We also examined rVSV/G, rVSV/EBOV-GP, and EBOV VLP budding and discovered that all three types of particles required XKR8 activity for efficient budding. Previous work by Adu-Gyamfi et al. showed that EBOV VP40 specifically binds to inner leaflet plasma membrane PS, and this interaction is required for efficient VP40 trafficking, oligomerization, and egress (27). In the same study, they report VP40-induced PS scrambling in transfected HEK293 cells. While seemingly counterintuitive, Adu-Gyamfi et al. suggested that VP40 dimers oligomerizing at the plasma membrane inner leaflet may eventually stabilize and release PS, and that subsequent enzyme-mediated PS externalization would promote particle egress by inducing positive membrane curvature. Therefore, for Ebolavirus, we postulate a mechanism wherein EBOV induces XKR8 activation after VP40 has bound to inner leaflet PS and oligomerized, and particle assembly has begun, which maximizes both viral budding efficiency and virion infectivity.

Parallel VSV M-PS budding experiments have not been conducted; however, evidence in the literature suggests a similar mechanism could describe VSV budding. Previous studies demonstrate that VSV M tightly associates with the cytosolic face of plasma membranes (68), preferentially binds to vesicles containing negatively charged phospholipids (69, 70), and that VSV infection causes cellular apoptosis and PS externalization (53, 54). Our data suggest efficient VSV budding requires PS externalization via XKR8 activation. Additional studies on VSV M-PS interactions will be needed to confirm this mechanism.

Evaluating the importance of XKR8 and EBOV envelope PS in more biologically relevant systems will be critical for better characterizing the EBOV apoptotic mimicry mechanism and the impact of this viral entry strategy on EBOV pathogenesis. Thus far, studies published on the role of scramblases in EBOV infectivity, including this study, produce EBOV in scramblase-deficient immortalized human cell lines and assess infectivity on Vero cells. Future studies expanding on this topic may incorporate primary target cell types in EBOV-infected humans, such as macrophages, dendritic cells, and cells from the liver, lung, spleen, kidneys, and blood vessels (6). Research investigating EBOV-induced effects on upstream determinants of scramblase activation such as cellular apoptosis and calcium effectors may provide additional clarity on the driving force behind EBOV envelope PS.

Experiments more closely examining EBOV budding in ΔXKR8 cells will also be needed to clarify inner/outer leaflet PS requirements. If EBOV VP40-PS binding and PS scrambling both enhance viral production, what specifically triggers XKR8 activation? Furthermore, if XKR8-induced positive membrane curvature aids in both VSV and

EBOV virion egress, XKR8 activity may promote budding of other enveloped viruses that assemble at the plasma membrane. These research avenues will deepen our understanding of virus-host lipid interactions, which may uncover novel, broadly applicable antivirals for EBOV and other enveloped viruses of great public health concern.

Materials and Methods

Cell lines and transfections. HAP1, HAP1ΔXKR8 (HZGHC005916c007), and HAP1ΔTMEM16F (HZGHC002956c003) cells (Horizon Discovery) were maintained in Iscove's media supplemented with 8% (vol/vol) fetal bovine serum (FBS). Knock-out HAP1 cells were verified by amplifying exon 2 of XKR8 and confirming it contained a two base pair insertion causing a frameshift mutation. ΔTMEM16f exon 5 lacked 20 base pairs. Vero (African green monkey kidney) cells stably expressing human SLAM and baby hamster kidney (BHK-21) cells stably expressing T7 polymerase (BSR-T7/5 [BHK-T7]) (71) were maintained in Dulbecco's modified Eagle's medium (DMEM) supplemented with 5% (vol/vol) FBS (58). All cells were kept at 37°C and 5% CO_2. BHK-T7 transfections were performed using Gene Juice (MilliporeSigma) and HAP1 and Vero transfections used JetOptimus (Polyplus) as per manufacturer's instructions.

Drugs and compounds. To induce the release of intracellular calcium stores, cells were treated for 5 minutes with 5 μM A23187 (Enzo Life Sciences) in PBS at room temperature prior to Annexin V cell staining. VLP-transfected cells were treated with 0.5 μM A23187 for 36 hours. To functionally inhibit XKR8, VLP-producing cells were treated with 20 μM Z-VAD-FMK (Enzo Life Sciences) 3 hours following VLP transfection.

Annexin V cell staining. HAP1-derived cells were infected with rVSV/G (MOI 0.5) for 16 hours to induce apoptosis or treated with 5 μM A23187 for 5 minutes to induce intracellular calcium influx. Phosphatidylserine externalization was quantified by co-staining with both annexin V-Pacific Blue (AnV-PacBlue) (Invitrogen) and propidium iodide (PI) (Sigma Aldrich). Cells were lifted using trypsin without EDTA, washed with PBS, and incubated in 100 μL of annexin binding buffer (10 mM HEPES, 140 mM NaCl, and 2.5 mM $CaCl_2$, pH 7.4) containing AnV-PacBlue and PI for 30 minutes on ice. Cells were then diluted 1:4 in annexin binding buffer and analyzed in a flow cytometer (BD-LSRII). Cell populations were gated using forward scatter/side scatter. We excluded doublets and cell aggregates by gating cell populations using side scatter area/side scatter height. The same gates were used for all samples. Mean Fluorescence Intensity (MFI) of the Pacific Blue fluorophore in PI negative cells was quantified and averaged over a minimum of 3 independent experiments.

TMEM16F immunoblot analysis. Parental and scramblase knockout HAP1 total cell lysates were subjected to SDS-PAGE and immunoblot analysis using anti-TMEM16F (1:1000, Sigma Aldrich, HPA038958) and β-actin C4 (1:1000, Santa Cruz Biotechnology Inc., sc-47778) antibodies. Immunoblots were probed with appropriate secondary antibodies conjugated with HRP and imaged with a ChemiDoc XRS digital imaging system (Bio-Rad).

Viruses. Measles virus (MeV-GFP), Edmonston strain, expressing GFP in a pre-N position has been previously described (72).

Generation of replication competent recombinant VSV. The full-length cDNA clone of the VSV genome (Indiana serotype) in which a multiple cloning site (MCS) (5'-

MluI- XmaI-SmaI-EagI-NheI-3') replaced the glycoprotein and GFP is encoded as an additional transcriptional unit between the MCS and the L gene, pVSV-ΔG-GFP-2.6 (courtesy of Dr. Michael Whitt; KeraFAST #EH1027) (73), was used as the backbone for all recombinant viruses. The VSV G Indiana strain (accession number: NP_041715.1) and EBOV glycoprotein Zaire strain (accession number: AAA96744.1) sequences were PCR amplified (ATG-stop codon) with primers that added a 5' MluI and 3' NheI sites (74). The glycoproteins were cloned into the genome using the MluI and NheI restriction sites. Viral constructs containing nano-luciferase within the viral particle were made by replacing the matrix (M) gene with the M-nLuc construct. M-nLuc was generated by adding the nano-luciferase coding region after residue 37 as was previously done with GFP (75).

Viruses were recovered by co-transfecting BHK-T7 cells with a plasmid carrying a cDNA copy of the recombinant VSV genome and plasmids encoding VSV polymerase (L), nucleocapsid (N), phosphoprotein (P), and glycoprotein (G) proteins (courtesy of Dr. Michael Whitt; KeraFAST) (73). All constructs were under the control of the T7 promoter. Transfected BHK-T7 cells were overlaid on Vero cells after 48 hours, and virus stocks were passaged onto fresh Vero cells using a low MOI 0.001 to generate subsequent stocks. All experiments were completed with virus produced from passage 3 or 4 in Vero cells. Viral titers were determined by performing end-point dilutions on HAP1 cells and calculating the 50% tissue culture infective dose ($TCID_{50}$) according to the Spearman-Karber method (76).

Multi-step replication curve. HAP1, ΔXKR8, and ΔTMEM16F cells were seeded in 12-well plates ($1.25x10^5$ cells/mL for rVSV/EBOV-GP or $2.5x10^5$ cells/mL for

rVSV/G and MeV) and infected with 25-100 virions of the indicated virus. Virus-containing media was removed 1 hour following infection and replaced with fresh Iscove's medium. At each time point, the supernatant was collected and replaced with fresh Iscove's medium. Because MeV is cell associated, the infected monolayer was scraped in 500 μL of supernatant and viral particles were released with two freeze-thaw cycles (72). All samples were stored at -80°C and later titrated on Vero cells.

Virus cell-cell spread. Cells were seeded in 12-well plates ($5x10^5$ cells/mL). After 24 hours, cells were incubated with rVSV/EBOV-GP or rVSV/G at MOI 0.01 for 2 hours at 37°C, inoculum was removed, and fresh media was replaced. Representative images were captured using the Zoe microscope (Bio-Rad) (magnification x20) at the indicated time points.

qRT-PCR. Viral RNA was isolated from infected cell supernatant (QIAamp® Viral RNA Mini Kit, Qiagen) and cell lysate (RNeasy Mini Kit, Qiagen). All samples were collected in duplicate. RNA was reverse transcribed into cDNA (High-Capacity RNA-to-cDNA™ Kit, Thermo Scientific). VSV genome copies were measured with qRT-PCR using the TaqMan Gene Expression Master Mix (Applied Biosystems), VSV-L forward and reverse primers, and probe (TaqMan MGB Probe) (77). Each sample was analyzed in duplicate, and each assay contained a DNA standard curve (VSV molecular clone, ranged from 3 to $3x10^7$ plasmid copies), no template, and no primer controls. Because the primers detect VSV-L RNAs, copies generated from cellular RNA detected both full-length genome as well as VSV-L transcripts. We extrapolated VSV copy numbers from the generated standard curve using the Applied Biosystems protocol. Final

copy numbers were adjusted by back-calculations to the total RNA and cDNA volume and expressed as copies per lysate or supernatant sample.

Virus entry and replication: qRT-PCR. HAP1 and ΔXKR8 cells were seeded in 12-well plates ($5x10^5$ cells/mL). After 24 hours, cells were infected with rVSV/G or rVSV/EBOV-GP (MOI= 0.05) for 2 hours at 37°C 5% CO_2. Virus-containing media was removed, and cells were treated with citric acid buffer (40 mM citric acid, 10 mM KCl, 135 mM NaCl, pH 3.0) for 1 minute to inactivate any remaining viral particles. Citric acid was removed, cells were washed with Iscove's media, and fresh Iscove's media was added.

Viral entry. To examine virus entry, viral genomes were quantified in cells 2 hours after infection. Viral copy number was determined by comparing the C(t) values in the total cellular RNA to a DNA standard curve. Three independent experiments were performed.

Viral RNA replication. Viral genome or RNA copy numbers were quantified in cells and supernatants 12 hours post-infection. Cell viral RNA numbers were adjusted for total ng RNA isolated and represented viral replication ability. Samples were collected in duplicate from 3 independent experiments.

GFP virus entry. HAP1 and ΔXKR8 cells were seeded in 48-well plates ($5x10^5$ cells/mL). After 24 hours, cells were incubated with rVSV/G or rVSV/EBOV-GP at a high MOI >1. After cells were infected for 3 hours at 37°C, virus-containing media was removed and replaced with fresh Iscove's medium containing 10 mM ammonium chloride (NH_4Cl; 30 mM, pH 7.0) in order to prevent subsequent rounds of virus replication (78). Cells were trypsinized 12 hours after infection, fixed with 4%

formaldehyde, and GFP-positive virus-infected cells were quantified using flow cytometry (BD-LSRII).

rVSV budding assays. *Luminescence assay.* Cells were seeded in 12-well plates ($5x10^5$ cells/mL). After 48 hours, cells were incubated with rVSV-MnLuc/G or rVSV-MnLuc/EBOV-GP (MOI= 0.2) for 2 hours at 37°C, inoculum was removed, cells were citric acid treated, washed, and fresh media was replaced. Twelve hours post infection supernatants were collected and cells were lysed in M2 lysis buffer (50 mM Tris [pH 7.4], 150 mM NaCl, 1 mM EDTA, 1% Triton X-100) at 4°C and clarified with centrifugation (20,000 × *g*, 15 min). Lysates and supernatants were assayed for nano-luciferase activity using Nano-Glo luciferase substrate (Promega) and luminescence was measured in the Glomax® Explorer (Promega). Budding efficiency was calculated by dividing the luminescent signals from the supernatant by the cell lysate. In all experiments, HAP1 budding efficiency was set to 100%.

Protein production. HAP1 and ΔXKR8 cells were seeded in 12-well plates ($5x10^5$ cells/mL). After 24 hours, cells were infected with rVSV/G or rVSV/EBOV-GP at high MOI >1 for 2 hours at 37°C 5% CO_2. Virus-containing media was removed, cells were treated with citric acid buffer for 1 minute, washed with Iscove's media, and fresh Iscove's medium containing 10 mM ammonium chloride was added. Cells were incubated at 37°C 5% CO_2 for 12 hours, after which cell lysates and supernatants were collected. Cell lysates and supernatants were subjected to immunoblot analysis using antibodies against cellular GAPDH (1:2000, SouthernBiotech, 47724), VSV-G (1:2000, Alpha Diagnostic, VSIG11-S), EBOV-GP (1:1000, IBT Bioservices, 0301-015), and VSV-M (1:2500, Kerafast, EB0011).

Transmission electron microscopy. Confluent flasks of HAP1 and ΔXKR8 cells were infected with rVSV/EBOV-GP or rVSV/G and harvested on day when >80% of the cells were GFP positive. Cells were fixed with 2.5% glutaraldehyde and 2% paraformaldehyde in PBS for 1 hour at room temperature. Cells were gently scraped of the flask, rinsed several times in PBS and enrobed in 4% Noble agar. Enrobed samples were rinsed several times in PBS and incubated for 1 hour in 1% OsO_4 in PBS and rinsed again several times in deionized water. Samples were then dehydrated in a series of graded ethanol. Subsequently, samples were infiltrated with Embed 812 resin and processed for 1-2 days at 60°C. Thin sections were mounted on copper mesh grids and post-stained with uranyl acetate and lead citrate. Specimens were viewed on a JEOL JEM1011 transmission electron microscope (JEOL, Inc., Peabody, MA). Samples were produced three independent times and representative images are shown.

Viral particle infectivity. HAP1 and ΔXKR8 cells were seeded in T75 flasks ($5x10^5$ cells/mL). After 24 hours, cells were infected with rVSV/G (MOI= 0.01) or rVSV/EBOV-GP (MOI= 2) for 2 hours at 37°C and 5% CO_2. Due to rVSV/G replicating and spreading at a much faster rate than rVSV/EBOV-GP, less virus was added so at time-of-harvest a similar level of infection had occurred in both populations. Virus-containing media was removed, cells were treated with citric acid buffer for 1 minute and washed, and fresh Iscove's media was added. After 24 hours, the supernatant was collected, concentrated and purified using Vivaspin 20 ultrafiltration units (300kDa MW cut-off, Sartorius), and stored at -80°C.

Genome:PFU analysis. The infectivities of viruses produced in HAP1 and ΔXKR8 cells were calculated by taking the ratio of genome copy numbers to PFU/mL for

each sample. To quantify genome copy numbers in each sample, qRT-PCR was performed on harvested virus as was described above. The PFU/mL for all samples was determined using plaque assays on Vero cells. Genome:PFU values were averaged from virus produced from 3-4 independent trials.

Vero genome:PFU rescue. Vero cells were seeded in a 24-well plate ($5x10^5$ cells/mL) and infected with HAP1-made or ΔXKR8-made rVSV/G or rVSV/EBOV-GP (MOI= 0.01). Infection proceeded for 2 hours at 37°C and 5% CO_2. Virus-containing media was removed, and cells were treated with citric acid buffer for 1 minute, washed, and fresh Iscove's media was added. After 24 hours, the supernatants were collected and stored at -80°C. Genome:PFU for these samples was determined as described above.

Viral particle glycoprotein incorporation. HAP1 and ΔXKR8 cells were seeded in 6-well plates ($5x10^5$ cells/mL). After 24 hours, cells were infected with rVSV/EBOV-GP (MOI 2) for 2 hours at 37°C 5% CO_2. Virus-containing media was removed, cells were treated with citric acid buffer for 1 minute, washed, and fresh Iscove's media was added. Cells were incubated at 37°C 5% CO_2 for 24 hours, after which cell supernatants were collected. A portion of supernatants was used for viral genome quantification in order to normalize samples. Normalized supernatants were precipitated using 10% (wt/vol) TCA (79). The TCA-treated proteins were pelleted (17,000 × *g*, 30 min, 4°C), washed with acetone, dried, and denatured using SDS-urea buffer (200 mM Tris [pH 6.8], 8 M urea, 5% SDS, 0.1 mM EDTA, 0.03% bromophenol blue). The denatured TCA-treated proteins were subjected to immunoblot and densitometry analysis for VSV M and EBOV GP protein levels using anti-VSV M (1:2500, Kerafast, EB0011) and anti-EBOV GP (1:1000, IBT Bioservices, 0301-015) antibodies.

rVSV surface PS quantification. HAP- or ΔXKR8- produced purified rVSV/G or rVSV/EBOV-GP ($1.5x10^9$ genomes) were conjugated to 4-μm aldehyde/sulfate latex beads (Thermo Fisher Scientific) overnight at 4°C with gentle shaking. Beads were blocked with 1% BSA in PBS for 2 hours while rotating at room temperature. The reaction was quenched by adding 100 mM of glycine for 30 minutes at room temperature. Beads were washed 3 times with 1% BSA in PBS, then incubated with 100 μL of AnV binding buffer containing AnV-PacBlue for 15 minutes at room temperature. Beads were diluted 1:5 in AnV binding buffer and analyzed using flow cytometry. Beads were then washed 3 times with 1% BSA in PBS, followed by a 2 hour incubation with antibodies against VSV-G (1:200, Alpha Diagnostic International, VSIG11-S) or EBOV-GP (1:50, IBT Bioservices, 21D10) at room temperature with gentle shaking. Beads were then washed and incubated with anti-rabbit FITC (1:100, KPL, 02-15-16) or anti-mouse APC (1:50, Jackson ImmunoResearch, 115-135-164) secondary antibodies for 1 hour at room temperature with gentle shaking. Samples were analyzed by flow cytometry (BD-LSRII).

Generation of EBOV VLPs. EBOV VLPs were produced by transfecting plasmids encoding EBOV GP, NP, and VP40 at a 1:1:1 ratio into the indicated cell lines. The GP reading frame from pcDNA-ZaireEBOV GP encoding the Zaire EBOV GP (a gift from Patrick Sinn, University of Iowa) was cloned into a pcDNA3.1intron vector (80). The pCAGGS-NP-EBOV plasmid encoding the Zaire EBOV NP was a gift from Elke Mühlberger (Addgene plasmid #103049) (81). The pmCherry-VP40 plasmid was a gift from Judith White (Addgene plasmid #74421) (82). We replaced the mCherry reading frame with nano-luciferase (VP40-nLuc) (Promega). In some experiments, additional plasmids encoding $XKR8_{FLAG}$, empty vector, or tetherin were also transfected.

The human XKR8 reading frame was cloned into pcDNA-intron (83) and a 3xFLAG tag was added to the N-terminus. pCMV-HA-Tetherin was a gift from Paul Spearman (Addgene plasmid # 41068) (84).

VLP budding assays. *Immunoblotting.* HAP1 or ΔXKR8 cells were seeded in 100mm dishes ($6x10^5$ cells/mL). After 24 hours, cells were transfected with VP40, NP, GP, and either empty vector or tetherin, an EBOV budding inhibitor (64). Media was replaced 4 hours after transfection, and supernatants and cell lysates were collected 48 hours after transfection and cleared of cell debris with centrifugation. To remove non-VLP-associated monomeric VP40, supernatants were overlaid on 2 mL 20% (w/v) sucrose and ultracentrifuged at 37,000 RPM at 4°C for 2 hours, and VLP pellets were resuspended in 100 µL of PBS (85). Cell lysates and VLP pellets were denatured using SDS-urea buffer and subjected to SDS-PAGE. Gels were then immunoblotted with anti-VP40 antibody (1:2000, IBT Bioservices, 0301-010) and anti-GP antibody (1:2000, IBT Bioservices, 0301-015). Lysate samples were also immunoblotted with anti-vinculin antibody (1:2000, BioRad, MCA465GA). Immunoblots were imaged with a ChemiDoc XRS digital imaging system (Bio-Rad).

Luminescence assays. HAP1 and ΔXKR8 cells were seeded in 6-well plates ($6x10^5$ cells/mL). After 24 hours, cells were co-transfected with VP40-nLuc, NP, GP, and either tetherin, $XKR8_{FLAG}$, caspase-resistant XKR8-2DA, or empty vector (51). Media was replaced 3-4 hours post transfection, and supernatants and cell lysates were collected 24 hours post transfection and cleared of cell debris with centrifugation. NLuc-VLP pellets were prepared as described above. Luciferase activity was detected using Nano-Glo Luciferase substrate (Promega) and luminescence was measured in the Glomax®

Explorer (Promega). In experiments that included DMSO or Z-VAD-FMK (20μM), treatments were added during media replacement 4 hours following transfection. In experiments that included DMSO or A23187 (0.5μM), treatments were added 12 hours following transfection, and lysates and supernatants were collected 48 hours following transfection. Budding efficiency was determined by dividing the luminescence signals in the supernatant by the cell lysate. In all experiments, HAP1 budding efficiency was set to 100%.

We also produced VLPs by transfecting cells with VP40-nLuc and either empty vector (1:2), GP+empty vector (1:1:1), NP+empty vector (1:1:1), GP+NP (1:1:1), or SARS-CoV-2 $S_{Met1}\Delta 21$+empty vector (1:1:1). SARS-CoV-2 $S_{Met1}\Delta 21$ contains an additional 9 residues in the signal peptide to reflect a previously proposed upstream in-frame alternate start codon (referred to with the subscript Met1) and a truncated cytoplasmic tail (86). VLP budding efficiency was measured as described above.

VLP Glycoprotein Incorporation. HAP1 and ΔXKR8 cells were seeded in 6-well plates ($6x10^5$ cells/mL). After 24 hours, cells were co-transfected with VP40-nLuc, NP, and GP. Media was replaced 4 hours post transfection. Supernatants were collected 24 hours post transfection and nLuc-VLP pellets were prepared as described above. NLuc-VLP's were normalized using luciferase activity, denatured using SDS-urea buffer, and subjected to SDS-PAGE. Gels were then immunoblotted with anti-VP40 antibody (1:2000, IBT Bioservices, 0301-010) and anti-GP antibody (1:2000, IBT Bioservices, 0301-015). Immunoblots were imaged with a ChemiDoc XRS digital imaging system (Bio-Rad). VP40 and GP protein levels were quantified using densitometry analysis.

XKR8-2DA validation. A caspase-resistant pcDNA-XKR8-2DA$_{FLAG}$ plasmid was produced by introducing alanine substitutions at residues D352 and D355 to our XKR8$_{FLAG}$ plasmid using site-directed mutagenesis (51). The XKR8-2DA$_{FLAG}$ mutation was verified first by sequence analysis, then by immunoblot analysis to ensure that only full-length XKR8-2DA$_{FLAG}$ (48kda) was present in ΔXKR8 cells producing EBOV VLPs (rather than the cleaved product at ~42kda). ΔXKR8 cells were seeded in 6-well plates ($6x10^5$ cells/mL). After 24 hours, cells were co-transfected with VP40-nLuc, NP, GP, and either empty plasmid, XKR8$_{FLAG}$, or XKR8-2DA$_{FLAG}$. Media was replaced 4 hours post transfection, and supernatants and cell lysates were collected 48 hours post transfection and cleared of cell debris with centrifugation. NLuc-VLP pellets were prepared as described above. Cell lysates and pellets were denatured using SDS-urea buffer and subjected to SDS-PAGE. Gels were immunoblotted with anti-vinculin antibody (1:2000, BioRad, MCA465GA), anti-FLAG antibody (1:2500, Sigma Aldrich, F1804), and anti-VP40 (1:2000, IBT Bioservices, 0301-010). Immunoblots were imaged with a ChemiDoc XRS digital imaging system (Bio-Rad).

Statistical Analysis. Results are presented as averages with standard errors of the mean (SEM) from at least 3 independent trials. Averages were compared using the Student's t-test or Welch's t-test if unequal variance in JMP® Pro software (version 13.2.0) or GraphPad Prism. A p-value of less than 0.05 was considered statistically significant.

Acknowledgments

We thank the CVM Cytometry Core Facility for technical assistance, and members of the Brindley lab for helpful comments on the manuscript.

Research reported in this publication was supported by the National Institute of Allergy and Infectious Diseases of the National Institutes of Health under Award Number R01AI139238.

The content is solely the responsibility of the authors and does not necessarily represent the official views of the National Institutes of Health.

References

1. CDC. 15 May 2018. Ebola Virus Disease Distribution Map: Cases of Ebola Virus Disease in Africa Since 1976. https://www.cdc.gov/vhf/ebola/history/distribution-map.html. Accessed 23 August 2018.

2. Bausch DG. 2021. The need for a new strategy for Ebola vaccination. Nat Med 27:580-581.

3. Dokubo EK, Wendland A, Mate SE, Ladner JT, Hamblion EL, Raftery P, Blackley DJ, Laney AS, Mahmoud N, Wayne-Davies G, Hensley L, Stavale E, Fakoli L, Gregory C, Chen TH, Koryon A, Roth Allen D, Mann J, Hickey A, Saindon J, Badini M, Baller A, Clement P, Bolay F, Wapoe Y, Wiley MR, Logue J, Dighero-Kemp B, Higgs E, Gasasira A, Williams DE, Dahn B, Kateh F, Nyenswah T, Palacios G, Fallah MP. 2018. Persistence of Ebola virus after the end of widespread transmission in Liberia: an outbreak report. Lancet Infect Dis 18:1015-1024.

4. WHO. 12 February 2018. Ebola virus disease. http://www.who.int/news-room/fact-sheets/detail/ebola-virus-disease. Accessed 23 August 2018.

5. Prescott JB, Marzi A, Safronetz D, Robertson SJ, Feldmann H, Best SM. 2017. Immunobiology of Ebola and Lassa virus infections. Nat Rev Immunol 17:195-207.

6. Martines RB, Ng DL, Greer PW, Rollin PE, Zaki SR. 2015. Tissue and cellular tropism, pathology and pathogenesis of Ebola and Marburg viruses. J Pathol 235:153-74.

7. Mulherkar N, Raaben M, de la Torre JC, Whelan SP, Chandran K. 2011. The Ebola virus glycoprotein mediates entry via a non-classical dynamin-dependent macropinocytic pathway. Virology 419:72-83.

8. Hunt CL, Kolokoltsov AA, Davey RA, Maury W. 2011. The Tyro3 receptor kinase Axl enhances macropinocytosis of Zaire ebolavirus. J Virol 85:334-47.

9. Carette JE, Raaben M, Wong AC, Herbert AS, Obernosterer G, Mulherkar N, Kuehne AI, Kranzusch PJ, Griffin AM, Ruthel G, Dal Cin P, Dye JM, Whelan SP, Chandran K, Brummelkamp TR. 2011. Ebola virus entry requires the cholesterol transporter Niemann-Pick C1. Nature 477:340-3.

10. Chandran K, Sullivan NJ, Felbor U, Whelan SP, Cunningham JM. 2005. Endosomal proteolysis of the Ebola virus glycoprotein is necessary for infection. Science 308:1643-5.

11. Fujihira H, Usami K, Matsuno K, Takeuchi H, Denda-Nagai K, Furukawa JI, Shinohara Y, Takada A, Kawaoka Y, Irimura T. 2018. A Critical Domain of Ebolavirus Envelope Glycoprotein Determines Glycoform and Infectivity. Sci Rep 8:5495.

12. Rogers KJ, Maury W. 2018. The role of mononuclear phagocytes in Ebola virus infection. J Leukoc Biol 104:717-727.

13. Jemielity S, Wang JJ, Chan YK, Ahmed AA, Li W, Monahan S, Bu X, Farzan M, Freeman GJ, Umetsu DT, Dekruyff RH, Choe H. 2013. TIM-family proteins promote infection of multiple enveloped viruses through virion-associated phosphatidylserine. PLoS Pathog 9:e1003232.

14. Moller-Tank S, Kondratowicz AS, Davey RA, Rennert PD, Maury W. 2013. Role of the phosphatidylserine receptor TIM-1 in enveloped-virus entry. J Virol 87:8327-41.

15. Brindley MA, Hunt CL, Kondratowicz AS, Bowman J, Sinn PL, McCray PB, Jr., Quinn K, Weller ML, Chiorini JA, Maury W. 2011. Tyrosine kinase receptor Axl enhances entry of Zaire ebolavirus without direct interactions with the viral glycoprotein. Virology 415:83-94.

16. Kondratowicz AS, Lennemann NJ, Sinn PL, Davey RA, Hunt CL, Moller-Tank S, Meyerholz DK, Rennert P, Mullins RF, Brindley M, Sandersfeld LM, Quinn K, Weller M, McCray PB, Jr., Chiorini J, Maury W. 2011. T-cell immunoglobulin and mucin domain 1 (TIM-1) is a receptor for Zaire Ebolavirus and Lake Victoria Marburgvirus. Proc Natl Acad Sci U S A 108:8426-31.

17. Shimojima M, Takada A, Ebihara H, Neumann G, Fujioka K, Irimura T, Jones S, Feldmann H, Kawaoka Y. 2006. Tyro3 family-mediated cell entry of Ebola and Marburg viruses. J Virol 80:10109-16.

18. Amara A, Mercer J. 2015. Viral apoptotic mimicry. Nat Rev Microbiol 13:461-9.

19. Richard AS, Zhang A, Park SJ, Farzan M, Zong M, Choe H. 2015. Virion-associated phosphatidylethanolamine promotes TIM1-mediated infection by Ebola, dengue, and West Nile viruses. Proc Natl Acad Sci U S A 112:14682-7.

20. Brouillette RB, Phillips EK, Patel R, Mahauad-Fernandez W, Moller-Tank S, Rogers KJ, Dillard JA, Cooney AL, Martinez-Sobrido L, Okeoma C, Maury W. 2018. TIM-1 Mediates Dystroglycan-Independent Entry of Lassa Virus. J Virol doi:10.1128/JVI.00093-18.

21. Fedeli C, Torriani G, Galan-Navarro C, Moraz ML, Moreno H, Gerold G, Kunz S. 2018. Axl Can Serve as Entry Factor for Lassa Virus Depending on the Functional Glycosylation of Dystroglycan. J Virol 92.

22. Shimojima M, Stroher U, Ebihara H, Feldmann H, Kawaoka Y. 2012. Identification of cell surface molecules involved in dystroglycan-independent Lassa virus cell entry. J Virol 86:2067-78.

23. Meertens L, Labeau A, Dejarnac O, Cipriani S, Sinigaglia L, Bonnet-Madin L, Le Charpentier T, Hafirassou ML, Zamborlini A, Cao-Lormeau VM, Coulpier M, Misse D, Jouvenet N, Tabibiazar R, Gressens P, Schwartz O, Amara A. 2017. Axl Mediates ZIKA Virus Entry in Human Glial Cells and Modulates Innate Immune Responses. Cell Rep 18:324-333.

24. Morizono K, Xie Y, Olafsen T, Lee B, Dasgupta A, Wu AM, Chen IS. 2011. The soluble serum protein Gas6 bridges virion envelope phosphatidylserine to the TAM receptor tyrosine kinase Axl to mediate viral entry. Cell Host Microbe 9:286-98.

25. Brunton B, Rogers K, Phillips EK, Brouillette RB, Bouls R, Butler NS, Maury W. 2019. TIM-1 serves as a receptor for Ebola virus in vivo, enhancing viremia and pathogenesis. PLoS Negl Trop Dis 13:e0006983.

26. Younan P, Iampietro M, Nishida A, Ramanathan P, Santos RI, Dutta M, Lubaki NM, Koup RA, Katze MG, Bukreyev A. 2017. Ebola Virus Binding to Tim-1 on T Lymphocytes Induces a Cytokine Storm. mBio 8.

27. Adu-Gyamfi E, Johnson KA, Fraser ME, Scott JL, Soni SP, Jones KR, Digman MA, Gratton E, Tessier CR, Stahelin RV. 2015. Host Cell Plasma Membrane Phosphatidylserine Regulates the Assembly and Budding of Ebola Virus. J Virol 89:9440-53.

28. Lyles DS. 2013. Assembly and budding of negative-strand RNA viruses. Adv Virus Res 85:57-90.

29. Pierson TC, Diamond MS. 2012. Degrees of maturity: the complex structure and biology of flaviviruses. Curr Opin Virol 2:168-75.

30. Johnson DC, Baines JD. 2011. Herpesviruses remodel host membranes for virus egress. Nat Rev Microbiol 9:382-94.

31. van Meer G, Voelker DR, Feigenson GW. 2008. Membrane lipids: where they are and how they behave. Nat Rev Mol Cell Biol 9:112-24.

32. Moller-Tank S, Maury W. 2014. Phosphatidylserine receptors: enhancers of enveloped virus entry and infection. Virology 468-470:565-80.

33. Younan P, Iampietro M, Santos RI, Ramanathan P, Popov VL, Bukreyev A. 2018. Role of Transmembrane Protein 16F in the Incorporation of Phosphatidylserine Into Budding Ebola Virus Virions. J Infect Dis 218:S335-S345.

34. Gupta M, Spiropoulou C, Rollin PE. 2007. Ebola virus infection of human PBMCs causes massive death of macrophages, CD4 and CD8 T cell sub-populations in vitro. Virology 364:45-54.

35. Johnson KA, Taghon GJ, Scott JL, Stahelin RV. 2016. The Ebola Virus matrix protein, VP40, requires phosphatidylinositol 4,5-bisphosphate (PI(4,5)P2) for extensive oligomerization at the plasma membrane and viral egress. Sci Rep 6:19125.

36. Nanbo A, Maruyama J, Imai M, Ujie M, Fujioka Y, Nishide S, Takada A, Ohba Y, Kawaoka Y. 2018. Ebola virus requires a host scramblase for externalization of phosphatidylserine on the surface of viral particles. PLoS Pathog 14:e1006848.

37. Segawa K, Suzuki J, Nagata S. 2014. Flippases and scramblases in the plasma membrane. Cell Cycle 13:2990-1.

38. Huang D, Xu B, Liu L, Wu L, Zhu Y, Ghanbarpour A, Wang Y, Chen FJ, Lyu J, Hu Y, Kang Y, Zhou W, Wang X, Ding W, Li X, Jiang Z, Chen J, Zhang X, Zhou H, Li JZ, Guo C, Zheng W, Zhang X, Li P, Melia T, Reinisch K, Chen XW. 2021. TMEM41B acts as an ER scramblase required for lipoprotein biogenesis and lipid homeostasis. Cell Metab doi:10.1016/j.cmet.2021.05.006.

39. Li YE, Wang Y, Du X, Zhang T, Mak HY, Hancock SE, McEwen H, Pandzic E, Whan RM, Aw YC, Lukmantara IE, Yuan Y, Dong X, Don A, Turner N, Qi S, Yang H. 2021. TMEM41B and VMP1 are scramblases and regulate the distribution of cholesterol and phosphatidylserine. J Cell Biol 220.

40. Hoffmann HH, Schneider WM, Rozen-Gagnon K, Miles LA, Schuster F, Razooky B, Jacobson E, Wu X, Yi S, Rudin CM, MacDonald MR, McMullan LK, Poirier JT, Rice CM. 2021. TMEM41B Is a Pan-flavivirus Host Factor. Cell 184:133-148 e20.

41. Trimarco JD, Heaton BE, Chaparian RR, Burke KN, Binder RA, Gray GC, Smith CM, Menachery VD, Heaton NS. 2021. TMEM41B is a host factor required for the replication of diverse coronaviruses including SARS-CoV-2. PLoS Pathog 17:e1009599.

42. Zaitseva E, Zaitsev E, Melikov K, Arakelyan A, Marin M, Villasmil R, Margolis LB, Melikyan GB, Chernomordik LV. 2017. Fusion Stage of HIV-1 Entry Depends on Virus-Induced Cell Surface Exposure of Phosphatidylserine. Cell Host Microbe 22:99-110 e7.

43. Braga L, Ali H, Secco I, Chiavacci E, Neves G, Goldhill D, Penn R, Jimenez-Guardeno JM, Ortega-Prieto AM, Bussani R, Cannata A, Rizzari G, Collesi C, Schneider E, Arosio D, Shah AM, Barclay WS, Malim MH, Burrone J, Giacca M. 2021. Drugs that inhibit TMEM16 proteins block SARS-CoV-2 spike-induced syncytia. Nature 594:88-93.

44. Bevers EM, Williamson PL. 2016. Getting to the Outer Leaflet: Physiology of Phosphatidylserine Exposure at the Plasma Membrane. Physiol Rev 96:605-45.

45. Feng S, Dang S, Han TW, Ye W, Jin P, Cheng T, Li J, Jan YN, Jan LY, Cheng Y. 2019. Cryo-EM Studies of TMEM16F Calcium-Activated Ion Channel Suggest Features Important for Lipid Scrambling. Cell Rep 28:567-579 e4.

46. Kunzelmann K, Ousingsawat J, Benedetto R, Cabrita I, Schreiber R. 2019. Contribution of Anoctamins to Cell Survival and Cell Death. Cancers (Basel) 11.

47. Suzuki J, Fujii T, Imao T, Ishihara K, Kuba H, Nagata S. 2013. Calcium-dependent phospholipid scramblase activity of TMEM16 protein family members. J Biol Chem 288:13305-16.

48. Suzuki J, Umeda M, Sims PJ, Nagata S. 2010. Calcium-dependent phospholipid scrambling by TMEM16F. Nature 468:834-8.

49. Suzuki J, Imanishi E, Nagata S. 2016. Xkr8 phospholipid scrambling complex in apoptotic phosphatidylserine exposure. Proc Natl Acad Sci U S A 113:9509-14.

50. Suzuki J, Imanishi E, Nagata S. 2014. Exposure of phosphatidylserine by Xk-related protein family members during apoptosis. J Biol Chem 289:30257-67.

51. Suzuki J, Denning DP, Imanishi E, Horvitz HR, Nagata S. 2013. Xk-related protein 8 and CED-8 promote phosphatidylserine exposure in apoptotic cells. Science 341:403-6.

52. Flint M, Chatterjee P, Lin DL, McMullan LK, Shrivastava-Ranjan P, Bergeron E, Lo MK, Welch SR, Nichol ST, Tai AW, Spiropoulou CF. 2019. A genome-wide CRISPR screen identifies N-acetylglucosamine-1-phosphate transferase as a potential antiviral target for Ebola virus. Nat Commun 10:285.

53. Gaddy DF, Lyles DS. 2005. Vesicular stomatitis viruses expressing wild-type or mutant M proteins activate apoptosis through distinct pathways. J Virol 79:4170-9.

54. Gaddy DF, Lyles DS. 2007. Oncolytic vesicular stomatitis virus induces apoptosis via signaling through PKR, Fas, and Daxx. J Virol 81:2792-804.

55. Finkelshtein D, Werman A, Novick D, Barak S, Rubinstein M. 2013. LDL receptor and its family members serve as the cellular receptors for vesicular stomatitis virus. Proc Natl Acad Sci U S A 110:7306-11.

56. Noyce RS, Bondre DG, Ha MN, Lin LT, Sisson G, Tsao MS, Richardson CD. 2011. Tumor cell marker PVRL4 (nectin 4) is an epithelial cell receptor for measles virus. PLoS Pathog 7:e1002240.

57. Tatsuo H, Ono N, Tanaka K, Yanagi Y. 2000. SLAM (CDw150) is a cellular receptor for measles virus. Nature 406:893-7.

58. Ono N, Tatsuo H, Hidaka Y, Aoki T, Minagawa H, Yanagi Y. 2001. Measles viruses on throat swabs from measles patients use signaling lymphocytic activation molecule (CDw150) but not CD46 as a cellular receptor. J Virol 75:4399-401.

59. Takada A, Fujioka K, Tsuiji M, Morikawa A, Higashi N, Ebihara H, Kobasa D, Feldmann H, Irimura T, Kawaoka Y. 2004. Human macrophage C-type lectin specific for galactose and N-acetylgalactosamine promotes filovirus entry. J Virol 78:2943-7.

60. Obiang L, Raux H, Ouldali M, Blondel D, Gaudin Y. 2012. Phenotypes of vesicular stomatitis virus mutants with mutations in the PSAP motif of the matrix protein. J Gen Virol 93:857-865.

61. Taylor GM, Hanson PI, Kielian M. 2007. Ubiquitin depletion and dominant-negative VPS4 inhibit rhabdovirus budding without affecting alphavirus budding. J Virol 81:13631-9.

62. Jayakar HR, Murti KG, Whitt MA. 2000. Mutations in the PPPY motif of vesicular stomatitis virus matrix protein reduce virus budding by inhibiting a late step in virion release. J Virol 74:9818-27.

63. Licata JM, Johnson RF, Han Z, Harty RN. 2004. Contribution of ebola virus glycoprotein, nucleoprotein, and VP24 to budding of VP40 virus-like particles. J Virol 78:7344-51.

64. Kaletsky RL, Francica JR, Agrawal-Gamse C, Bates P. 2009. Tetherin-mediated restriction of filovirus budding is antagonized by the Ebola glycoprotein. Proc Natl Acad Sci U S A 106:2886-91.

65. Olejnik J, Alonso J, Schmidt KM, Yan Z, Wang W, Marzi A, Ebihara H, Yang J, Patterson JL, Ryabchikova E, Muhlberger E. 2013. Ebola virus does not block apoptotic signaling pathways. J Virol 87:5384-96.

66. Soares MM, King SW, Thorpe PE. 2008. Targeting inside-out phosphatidylserine as a therapeutic strategy for viral diseases. Nat Med 14:1357-62.

67. Nikolic J, Belot L, Raux H, Legrand P, Gaudin Y, A AA. 2018. Structural basis for the recognition of LDL-receptor family members by VSV glycoprotein. Nat Commun 9:1029.

68. Chong LD, Rose JK. 1993. Membrane association of functional vesicular stomatitis virus matrix protein in vivo. J Virol 67:407-14.

69. Zakowski JJ, Petri WA, Jr., Wagner RR. 1981. Role of matrix protein in assembling the membrane of vesicular stomatitis virus: reconstitution of matrix protein with negatively charged phospholipid vesicles. Biochemistry 20:3902-7.

70. Luan P, Yang L, Glaser M. 1995. Formation of membrane domains created during the budding of vesicular stomatitis virus. A model for selective lipid and protein sorting in biological membranes. Biochemistry 34:9874-83.

71. Buchholz UJ, Finke S, Conzelmann KK. 1999. Generation of bovine respiratory syncytial virus (BRSV) from cDNA: BRSV NS2 is not essential for virus replication in tissue culture, and the human RSV leader region acts as a functional BRSV genome promoter. J Virol 73:251-9.

72. Paal T, Brindley MA, St Clair C, Prussia A, Gaus D, Krumm SA, Snyder JP, Plemper RK. 2009. Probing the spatial organization of measles virus fusion complexes. J Virol 83:10480-93.

73. Whitt MA. 2010. Generation of VSV pseudotypes using recombinant DeltaG-VSV for studies on virus entry, identification of entry inhibitors, and immune responses to vaccines. J Virol Methods 169:365-74.

74. Brindley MA, Hughes L, Ruiz A, McCray PB, Jr., Sanchez A, Sanders DA, Maury W. 2007. Ebola virus glycoprotein 1: identification of residues important for binding and postbinding events. J Virol 81:7702-9.

75. Soh TK, Whelan SP. 2015. Tracking the Fate of Genetically Distinct Vesicular Stomatitis Virus Matrix Proteins Highlights the Role for Late Domains in Assembly. J Virol 89:11750-60.

76. Ramakrishnan MA. 2016. Determination of 50% endpoint titer using a simple formula. World J Virol 5:85-6.

77. Hole K, Clavijo A, Pineda LA. 2006. Detection and serotype-specific differentiation of vesicular stomatitis virus using a multiplex, real-time, reverse transcription-polymerase chain reaction assay. J Vet Diagn Invest 18:139-46.

78. Lay Mendoza MF, Acciani MD, Levit CN, Santa Maria C, Brindley MA. 2020. Monitoring Viral Entry in Real-Time Using a Luciferase Recombinant Vesicular Stomatitis Virus Producing SARS-CoV-2, EBOV, LASV, CHIKV, and VSV Glycoproteins. Viruses 12.

79. Acciani M, Alston JT, Zhao G, Reynolds H, Ali AM, Xu B, Brindley MA. 2017. Mutational Analysis of Lassa Virus Glycoprotein Highlights Regions Required for Alpha-Dystroglycan Utilization. J Virol 91.

80. Sinn PL, Hickey MA, Staber PD, Dylla DE, Jeffers SA, Davidson BL, Sanders DA, McCray PB, Jr. 2003. Lentivirus vectors pseudotyped with filoviral envelope glycoproteins transduce airway epithelia from the apical surface independently of folate receptor alpha. J Virol 77:5902-10.

81. Nelson EV, Pacheco JR, Hume AJ, Cressey TN, Deflube LR, Ruedas JB, Connor JH, Ebihara H, Muhlberger E. 2017. An RNA polymerase II-driven Ebola virus minigenome system as an advanced tool for antiviral drug screening. Antiviral Res 146:21-27.

82. Shoemaker CJ, Schornberg KL, Delos SE, Scully C, Pajouhesh H, Olinger GG, Johansen LM, White JM. 2013. Multiple cationic amphiphiles induce a Niemann-Pick C phenotype and inhibit Ebola virus entry and infection. PLoS One 8:e56265.

83. Willard KA, Alston JT, Acciani M, Brindley MA. 2018. Identification of Residues in Lassa Virus Glycoprotein Subunit 2 That Are Critical for Protein Function. Pathogens 8.

84. Ali MS, Hammonds J, Ding L, Spearman P. 2010. CAML does not modulate tetherin-mediated restriction of HIV-1 particle release. PLoS One 5:e9005.

85. Lin AE, Diehl WE, Cai Y, Finch CL, Akusobi C, Kirchdoerfer RN, Bollinger L, Schaffner SF, Brown EA, Saphire EO, Andersen KG, Kuhn JH, Luban J, Sabeti PC. 2020. Reporter Assays for Ebola Virus Nucleoprotein Oligomerization, Virion-Like Particle Budding, and Minigenome Activity Reveal the Importance of Nucleoprotein Amino Acid Position 111. Viruses 12.

86. Havranek KE, Jimenez AR, Acciani MD, Lay Mendoza MF, Reyes Ballista JM, Diaz DA, Brindley MA. 2020. SARS-CoV-2 Spike Alterations Enhance Pseudoparticle Titers and Replication-Competent VSV-SARS-CoV-2 Virus. Viruses 12.

CHAPTER 5

FLIPPASE SUBUNIT CDC50A REQUIRED FOR EBOLA VIRUS ENTRY AND OPTIMAL VESICULAR STOMATITIS VIRUS REPLICATION[3]

[3]Acciani MD, Reyes Ballista JM, Jimenez AR, Linn OL, Brindley MA. To be submitted to *J Virol*, May 1, 2022.

Abstract

The primary function of membranous viral envelopes is traditionally considered to be shielding viruses from the extracellular environment; however, their known role in virus replication has recently expanded. Evidence now suggests that for many viruses, envelope phospholipid phosphatidylserine (PS) enhances virus-cell surface attachment by binding to cellular PS receptors (PSRs), an entry strategy termed apoptotic mimicry. Cellular scramblases XKR8 and TMEM16F, are required for Ebola virus (EBOV) to incorporate PS in the envelope outer leaflet and increase infectivity via apoptotic mimicry. In this study, we investigated the role of cellular flippase activity in EBOV entry. Flippases maintain cellular membrane asymmetry by ensuring PS is localized to the inner leaflet of plasma membranes. Using human haploid HAP1 cells, we targeted P4-type ATPase ATP11C, a PS-specific plasma membrane flippase that directly transports outer leaflet PS to the inner leaflet, and beta subunit CDC50a, an essential P4 ATPase chaperone. While ATP11C was dispensable for cell PS internalization in HAP1 cells, normal-state HAP1ΔCDC50a (ΔCDC50a) cells constitutively exposed PS. Using recombinant vesicular stomatitis virus producing the EBOV GP (rVSV/EBOV-GP) or native glycoprotein (rVSV/G), we investigated how cells lacking CDC50a alter virus replication. We initially hypothesized that ΔCDC50a-made rVSV/EBOV-GP particles would spread through these cells more efficiently, because viral envelopes derived from ΔCDC50a cells would be more enriched in exposed PS and more easily engage PSR's on cell surfaces. Instead, we observed that rVSV/EBOV-GP multi-step replication was severely inhibited in ΔCDC50a cells, owing to a 78% decrease in rVSV/EBOV-GP entry caused by decreased levels of ΔCDC50a surface PSRs. Using rVSV encoding luciferase-

tagged matrix protein (MnLuc), we also examined viral budding efficiency and detected 3-4-fold more extracellular viral matrix protein released from ΔCDC50a cells. While deleting CDC50a appeared to enhance viral budding, we determined that these particles were approximately 3-4-fold less infectious than those produced in WT cells. Thus, our data indicates that the maintenance of plasma membrane inner leaflet PS by flippases is critical for basal HAP1 surface PSR levels and susceptibility to viruses entering via apoptotic mimicry. In addition, eliminating flippase activity in virus-infected HAP1 cells also promotes the release of defective viral particles.

Introduction

Ebola virus (EBOV) is an enveloped filovirus containing a single-stranded (-)RNA genome. EBOV infection can cause Ebola virus disease (EVD), characterized by a sudden onset of fever, intense weakness, muscle pain, headache, and sore throat. Disease can progress to vomiting, diarrhea, rash, impaired kidney and liver function, hemorrhaging, and death in approximately 50% of cases (1). Sporadic EBOV outbreaks have been recorded in Western and Central Africa since EBOV was identified in 1976, however, two of Africa's largest and deadliest outbreaks have occurred in the past 6 years (2014-2016 and 2018-2020). These recent outbreaks were caused by the *Zaire ebolavirus* species, but the *Sudan*, *Taï Forest*, and *Bundibugyio ebolavirus* species can also cause disease in humans (2).

EBOV is transmitted through direct contact of mucous membranes with infectious particles. The virus first infects dendritic cells and macrophages, which distribute particles throughout the body, ultimately infecting and replicating in multiple organs, including the liver (3). The EBOV glycoprotein (GP) mediates entry into host cells. GP1,

the GP receptor-binding domain, can anchor particles to the cell surface by binding to C-type lectins or glycosaminoglycans (GAGs) (4, 5). Virus-cell surface attachment may also occur via apoptotic mimicry, a GP-independent mechanism wherein viruses bind phagocytic receptors that typically mediate the clearance of phosphatidylserine (PS)-coated apoptotic cells. Once virions are surface-bound, they are internalized into endosomes through a dynamin-2-dependent macropinocytosis process (6). Host cell factors including homotypic fusion and protein sorting (HOPS) complex and UV radiation resistance-associated gene (UVRAG) traffic EBOV to endosomal/lysosomal compartments containing endosomal receptor Niemann-Pick C1 (NPC1) (7, 8). Cathepsins B/L carryout low pH-dependent GP proteolysis, enabling GP1 to interact with NPC1. This releases the GP fusion domain GP2, which orchestrates envelope-membrane fusion and the release of the viral genome into the cell cytoplasm (8-10). Following viral protein production and genome replication, newly translated structural viral proteins and nucleoprotein (NP)-coated genomes traffic to the cell surface. EBOV matrix protein VP40 then mediates particle assembly and budding through the plasma membrane, where particles are enveloped in GP-studded plasma membrane bilayer (11).

Much has been learned recently in the field of viral apoptotic mimicry, especially for EBOV. Several groups identified PS receptor (PSRs) that enhance *in vitro* EBOV entry, including T-cell immunoglobulin and mucin domain proteins TIM-1 and TIM-4, and receptor tyrosine kinases (RTKs) Tyro-3, Axl, and Mer (12). Furthermore, EBOV entry via RTKs may activate downstream signaling that promotes EBOV trafficking to NPC1 compartments (13). *In vivo*, knocking out TIM-1 in mice significantly improved

EVD survival, although it is unclear whether this was due to TIM-1's role as entry factor or as an immune system modulator (14, 15).

Several groups, including ours, also uncovered mechanisms contributing to exposed PS on the EBOV envelope (16-18). Our group and Nanbo et al found that plasma membrane phospholipid scramblase XKR8 is activated during EBOV virus-like particle (VLP) formation, resulting in particles with increased surface PS and improved entry into Vero cells (16, 18). In contrast, Younan et al observed that calcium-activated scramblase TMEM16F was required for optimal wild-type (WT) EBOV PS and cell-cell spread (17). Considering EBOV VLP production and WT-EBOV infection raise cytosolic calcium levels and activate several hallmarks of apoptosis, these scramblases may contribute to envelope PS individually or synergistically depending on the cell type and EBOV model tested, or even the stage virus replication in the cell (17-20).

For efficient apoptotic cell PS exposure and macrophage engulfment, the mechanism exploited in viral apoptotic mimicry, cells must inactivate flippases in addition to activating scramblases (21). However, studies on the role of flippases in viral apoptotic mimicry, and virus replication in general, are limited. Flippases are highly conserved, constitutively active, ATP-dependent enzymes that restrict PS to the inner leaflet of the plasma membrane in normal state cells. Cell PS exposure is highly regulated and reserved for essential biological processes such as blood clotting, bone mineralization, and apoptotic cell clearance (22). Thus, in normal-state cells, flippases transport any PS detected on the outer leaflet of the PM to the inner leaflet. Flippases are complexes consisting of a P4-ATPase and a CDC50 trafficking/folding chaperone. Out of 14 human P4-ATPases and two CDC50 subunits, ATP11C complexed with CDC50a is

the most well-characterized flippase complex that localizes to the plasma membrane and demonstrates PS specificity. Structural analysis showed that ATP11C attracts polar PS headgroups in the outer leaflet, then transports PS in its entirety to the inner leaflet through a transmembrane crevice (23). The cytoplasmic portion of ATP11C also contains three caspase recognition sites that, when cleaved, inactivate ATP11C by possibly inhibiting ATP binding (23). A rise in cytosolic calcium can also temporarily inhibit ATP11C/CDC50a flippase activity, although the mechanism is unknown (24). Therefore, it is speculated that TMEM16F is active and ATP11C/CDC50a is inactive during calcium-induced cellular PS exposure, while XKR8 is active and ATP11C/CDC50a is inactive during apoptosis-induced PS exposure. To sufficiently mimic an apoptotic cell, EBOV also likely requires ATP11C/CDC50a inactivation in addition to scramblase activation during budding.

In our previous study, we showed that producing recombinant vesicular stomatitis virus encoding EBOV GP (rVSV/EBOV-GP) in human haploid HAP1 XKR8 knockout cells, which lack apoptosis-induced scrambling activity, yielded virions with reduced surface PS levels (16). In this study, we aimed to produce virions with above-wild-type (WT) surface PS levels and infectivity by using flippase knockout HAP1ΔATP11C (ΔATP11C) and HAP1ΔCDC50a (ΔCDC50a) cells, which fail to internalize PS (21). We observed no changes in ΔATP11C PS externalization, however, normal state and apoptotic ΔCDC50a cells exposed significantly more PS than WT HAP1 cells. While evaluating rVSV/EBOV-GP replication in ΔCDC50a cells, we observed unanticipated EBOV GP-specific and non-specific phenotypes in addition to altered infectivity (which was reduced rather than enhanced). We found that deleting CDC50a downregulated

HAP1 PSR Tyro-3 surface levels and severely reduced rVSV/EBOV GP entry but did not impact the entry of rVSV producing native glycoprotein (rVSV/G). Furthermore, rVSV budding was enhanced by 3-4-fold in ΔCDC50a cells, but ΔCDC50a-made particles were less infectious relative to those produced by WT cells. Therefore, we concluded that cell maintenance of PS in the inner leaflet is critical for EBOV entry and optimal VSV replication.

Results

Cells lacking flippase CDC50a, but not ATP11C, constitutively expose PS. Nagata et al. first identified ATP11C and CDC50a using a genetic screen in KMB7 cells- a chronic myelogenous leukemia (CML) cell line from which HAP1 cells are derived (25). After incubating WT, ΔATP11C, and ΔCDC50a KMB7 cells with fluorescent PS analogue 7-nitro-2-1,3-benzoxadiazol-4-yl-PS (NBD-PS), they observed that WT plasma membranes incorporated and internalized NBD-PS while ΔATP11C, and ΔCDC50a cells did not. When they stained cell surfaces with PS-binding protein annexin V (AnV), they observed that normal state WT and ΔATP11C cells internalized PS, however, normal state ΔCDC50a cells demonstrated apoptosis-level PS exposure (21).

To characterize normal state and apoptotic flippase activity in our HAP1, ΔATP11C, and ΔCDC50a cell lines, we stained untreated and MG132-treated cells with AnV-Pacific Blue (AnV-PacBlue) (Fig1). MG132-treated ΔXKR8 cells served as an apoptotic AnV-low negative control. While we did not observe any difference in ΔATP11C and WT basal and apoptotic PS exposure, normal state and apoptotic ΔCDC50a cells exposed approximately 5.6 and 2.9 times more PS than normal state and apoptotic wild type HAP1 cells, respectively. We concluded that CDC50a is essential for

PS internalization and even reduces apoptotic PS exposure in HAP1 cells, while ATP11C is dispensable. Therefore, we excluded ΔATP11C cells from future experiments.

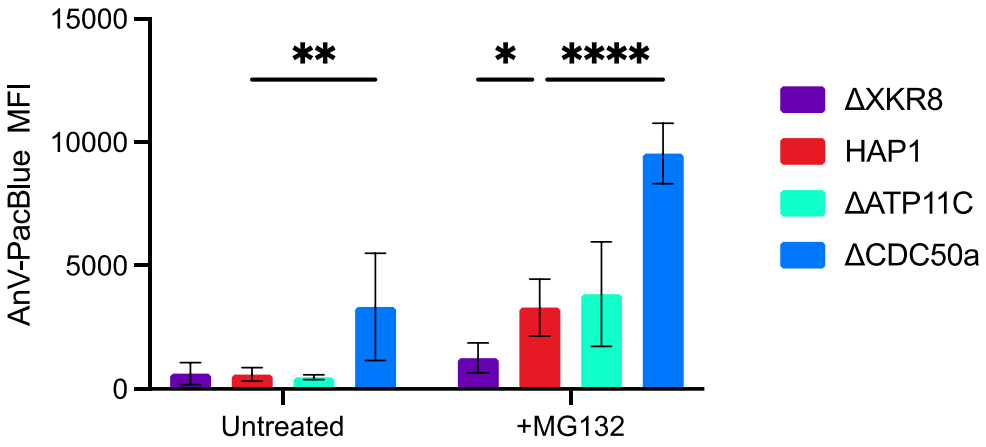

Fig 1. Deleting CDC50a increases baseline and apoptotic cellular PS exposure. HAP1, ΔATP11C, and ΔCDC50a cells were treated with 1μM MG132 for 24 h to induce apoptosis. Treated and untreated cells were then double stained with AnV-PacBlue and PI and analyzed using a BD LSRII flow cytometer. Anv-PacBlue average mean fluorescence intensities (MFIs) of live, single, nonnecrotic cells are shown. The values shown are averages from at least three independent experiments ± SEM. *, $P < 0.05$, **, $P < 0.01$, and ****, $P < 0.0001$, by Student's t test.

EBOV-GP mediated rVSV cell-to-cell spread is delayed in ΔCDC50a cells.

We then assessed multi-cycle virus replication in WT and ΔCDC50a cells using rVSV encoding EBOV-GP (rVSV/EBOV-GP) or its native glycoprotein (rVSV/G), as well as live attenuated Chikungunya virus strain 181/25 (CHIKV 181/25) (Fig 2A-C). rVSV/G cell surface attachment occurs primarily through specific protein binding interactions, although there is some evidence that PSRs can enhance VSV entry (26, 27). Like EBOV, CHIKV entry can proceed through several attachment factors including PSRs. All viruses were titrated on Vero-hSLAM cells that naturally produce PS receptors (TIM-1 and Axl) as well as rVSV/G receptors, but do not produce EBOV-enhancing C-type lectins.

Because ΔCDC50a cells demonstrate better-than-WT PS exposure, we hypothesized ΔCDC50a cells would produce highly infectious rVSV/EBOV-GP and CHIKV particles, resulting in faster replication kinetics and/or higher concentrations of infectious particles at each time point sampled. Instead, we observed significantly delayed rVSV/EBOVGP cell-to-cell spread in ΔCDC50a cells (Fig 2A). rVSV/G $TCID_{50}$ values were slightly reduced 12, 24, and 36 h post infection (Fig 2B). CHIKV-infected ΔCDC50a cells, however, released more infectious particles at 12, 24, 84, and 96 hours after infection (Fig 2C). These data indicate that ΔCDC50a cells support or enhance rVSV/G and CHIKV multi-cycle replication, but do not support efficient rVSV/EBOV-GP multi-cycle replication.

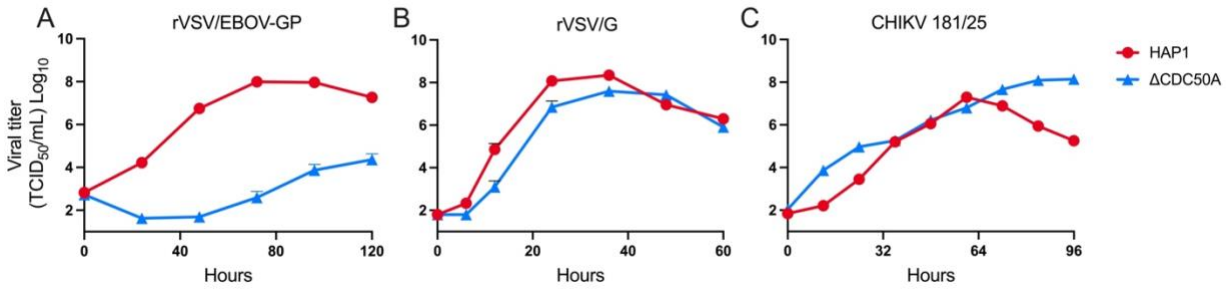

Fig 2. rVSV/EBOV-GP cell-to-cell spread is inhibited in cells lacking CDC50a. HAP1 and ΔCDC50a cells were infected with rVSV/EBOV-GP (A), rVSV/G (B), or CHIKV (C) MOI<1. Cell supernatants were collected at the indicated time points and titrated on Vero cells. The values shown are the average log_{10} $TCID_{50}$/mL from at least three independent experiments ± SEM.

EBOV-GP-mediated entry is inhibited in cells lacking CDC50a. Because we observed EBOV GP-specific cell-to-cell spread was defective in ΔCDC50 cells, we hypothesized these cells may be refractory to EBOV GP-mediated entry. To test this, we infected WT and ΔCDC50 cells with rVSV/EBOV-GP, rVSV/G, and CHIKV 181/25 (all encoding GFP), and quantified GFP+ cells after one round of virus replication (Fig 3A-C). While viral entry and RNA transcription precede cellular GFP production for

rVSV/EBOV-GP and rVSV/G, RNA transcription is governed by VSV machinery for both viruses. Therefore, differences in the proportion of GFP+ ΔCDC50a cells would indicate viral entry efficiency was altered. We found that rVSV/EBOV-GP entry was reduced by approximately 80% in ΔCDC50a cells (Fig 3A), however, rVSV/G and CHIKV entries were unaffected (Fig 3B-C).

We hypothesized that ΔCDC50 cells contained fewer surface PSRs as a potential downstream consequence of constitutive PS exposure. Because Tyro-3 is the main PSR produced by HAP1 cells, we examined surface versus cytoplasmic Tyro-3 levels in WT and ΔCDC50 cells (Fig 3D). We confirmed that surface Tyro-3 is reduced on ΔCDC50 cells, likely reducing EBOV-GP entry. While CHIKV also binds to PSRs, a genetic screen indicated that heparin sulfate is important for CHIKV entry in HAP1 cells (28). Therefore, CHIKV entry may proceed efficiently via heparin sulfate in ΔCDC50 cells.

We then asked if we could recover rVSV/EBOV-GP entry efficiency in ΔCDC50 cells by infecting these cells with more virus to better engage the limited amounts of Tyro-3 (Fig 3E). Indeed, we observed comparable proportions of GFP+ cells in WT and ΔCDC50 cells by incubating ΔCDC50 cells with 5-10 times more infectious particles.

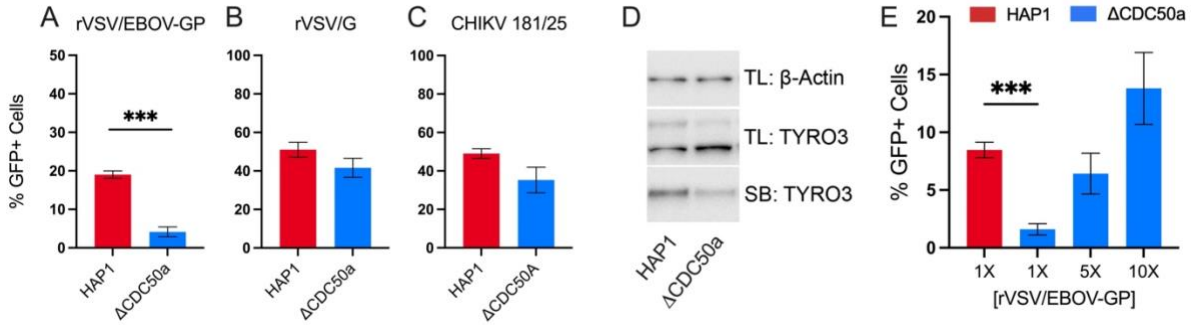

Fig 3. EBOV entry-enhancing PSRs are reduced on ΔCDC50a cells.
rVSV/EBOV-GP (A), rVSV/G (B), and CHIKV (C) entry was assessed in HAP1 and ΔCDC50a cells. Cells were infected with rVSV/G (MOI 1), rVSV/EBOV-GP (MOI 20)

of CHIKV (MOI 0.3) for 12 h, after which cells were harvested, fixed, and analyzed for viral reporter GFP fluorescence. (D) HAP1 and ΔCDC50a cells were subjected to surface biotinylation. Surface expressed biotinylated proteins were concentrated using streptavidin sepharose beads. Surface biotinylated proteins (SB) and total lysates (TL) were separated by SDS-PAGE and immunoblot analysis was performed using anti-Tyro-3 and β-actin antibodies. E) To achieve similar entry efficiencies, ΔCDC50a cells were infected with 1, 5, or 10 times more rVSV/EBOV-GP infectious particles. The values shown are averages from at least three independent experiments ± SEM. ***, $P < 0.001$, by Student's t test. (C) Data collected by colleague Dr. Kerri Miazgowicz.

Eliminating flippase activity increases rVSV budding. After VSV entry, RNA transcription/translation, and genome replication, new particles assemble at the cell surface and bud through the plasma membrane. To monitor rVSV budding efficiency in ΔCDC50a cells, we produced viruses containing matrix protein (M) tagged with nano-luciferase (MnLuc) and quantified luciferase levels in cell lysates and supernatants after one round of replication (Fig 4). rVSV/EBOV-GP-MnLuc infection of ΔCDC50a cells produced only 17% of the luciferase levels compared to infected WT cells, likely due to reduced EBOV-GP entry in ΔCDC50a cells (Fig 4A). In contrast, rVSV/G efficiently infects both WT and ΔCDC50a cells and produced similar luciferase levels in both cells types (Fig 4C). Unexpectedly, we observed 3 to 4 fold increases in rVSV/EBOV-GP-MnLuc and rVSV/G-MnLuc budding efficiency in ΔCDC50a cells, respectively, indicating that greater cellular PS exposure during rVSV infection may aid in particle budding in a glycoprotein-independent manner (Fig 4B and D). Notably rVSV/EBOV-GP and rVSV/G multi-cycle replication efficiency was reduced in ΔCDC50a cells in comparison to WT cells despite enhanced particle budding (Fig 2A and B).

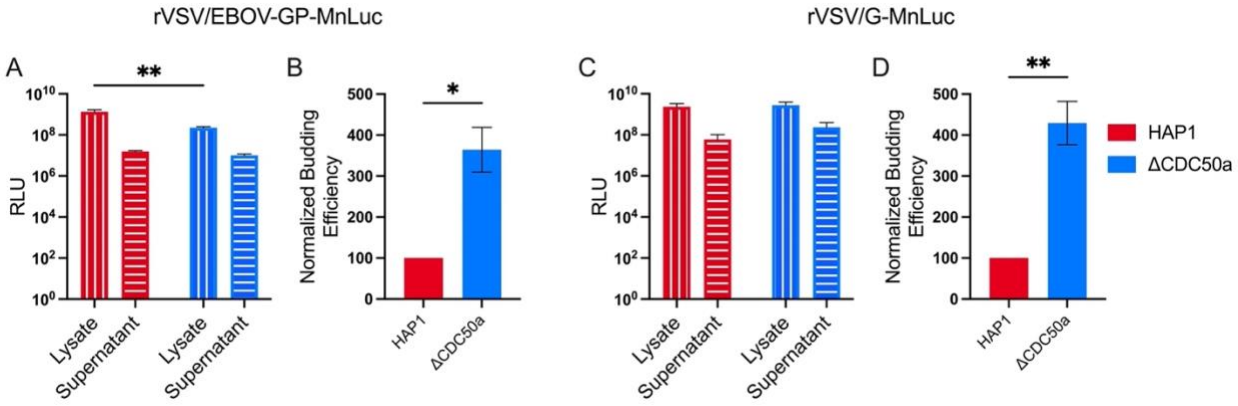

Fig 4. rVSV budding is enhanced in ΔCDC50a cells. HAP1 WT and ΔCDC50a cells were infected with rVSV/EBOV-GP-MnLuc (MOI 0.25) and rVSV/G-MnLuc (MOI 1). After one round of virus replication, cell lysate and supernatant nLuc activity was quantified using a luciferase assay (A and C). Budding efficiency was calculated by dividing supernatant nLuc activity by lysate nLuc activity, and values were normalized to HAP1 budding efficiency (B and D). The values shown are averages from at least three independent experiments ± SEM. *, P < 0.05, **, P < 0.01, by 2way ANOVA using the Šidák correction (A and C) or unpaired t test with Welch correction (B and D). (C and D) Data collected by colleague Judith M Reyes-Ballista.

rVSV virions produced by ΔCDC50a cells are less infectious. We then asked if producing rVSV/EBOV-GP in ΔCDC50a cells improves particle infectivity, presuming that viral envelopes derived from ΔCDC50a cells would contain more exposed PS and better engage PSRs. We infected WT and ΔCDC50a cells with rVSV/EBOV-GP or rVSV/G and collected viral particles in the supernatant after one round of replication. Because rVSV/EBOV-GP enters ΔCDC50a cells less efficiently (Fig 3A), we infected these cells with 20X more virus to establish similar numbers of infected cells. We quantified viral genomic RNA using qRT-PCR and infectious particle concentration by performing plaque assays on Vero cells (Fig 5A and C). We used the genome:plaque forming unit (PFU) ratio as a measure of infectivity, as it determines the number of viral genomes required to produce one plaque. Therefore, a lower genome:PFU value

means particles are more infectious, whereas high values suggest that many more viral particles are required to establish infection. We found that both rVSV/EBOV-GP and rVSV/G particles were less infectious when produced in ΔCDC50a cells (Fig 5 B and D). Three times more rVSV/EBOV-GP genomes and 4.8 times more rVSV/G genomes were required to form a plaque in comparison to WT HAP-made virus. We concluded that while ΔCDC50a cells release more rVSV particles containing genomic RNA and viral proteins, these particles are defective at establishing infection.

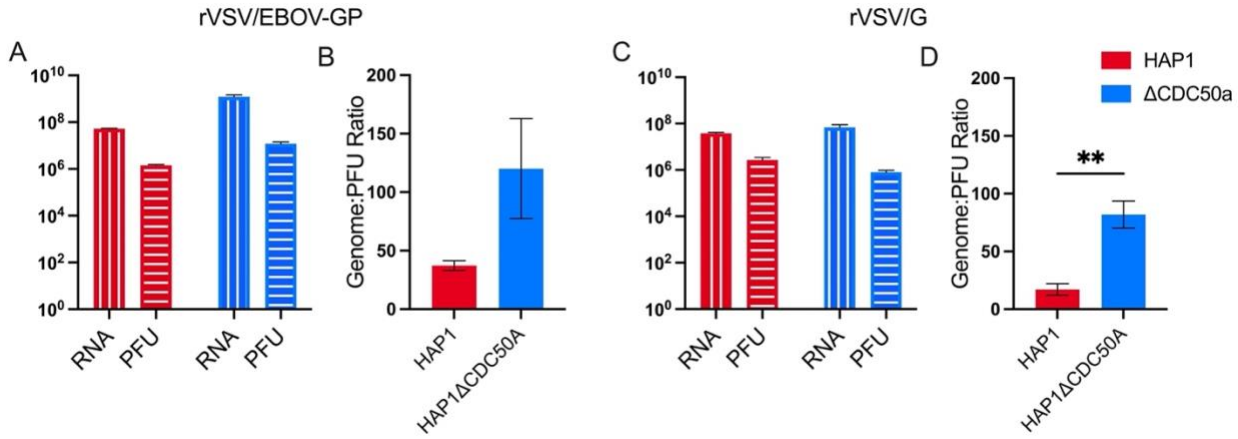

Fig 5. ΔCDC50a-produced rVSV is less infectious. rVSV/EBOV-GP and rVSV/G were propagated in HAP1 and ΔCDC50a cells for 8h (EBOV-GP) or 4h (G) respectively, MOI >1. Supernatants were collected and titrated via plaque assay, and viral genomes were quantified by qRT- PCR (A and C). Viral genome/PFU ratios were determined by calculating the ratio of viral genome copy numbers to infectious particle numbers (PFU/mL) for each sample (B and D).

Discussion

Due to mounting evidence that PS sidedness in cellular plasma membranes directly impacts EBOV infectivity, we investigated whether PS-internalizing flippases serve as EBOV host-cell factors. We determined that P4-ATPase subunit CDC50a was required for internalizing plasma membrane PS in normal-state HAP1 cells, and

eliminating this protein via CRISPR resulted in constitutive PS exposure and higher-than-WT levels of apoptosis-induced PS exposure. We expected this phenotype to be ultimately proviral for rVSV/EBOV-GP multi-cycle replication, presuming that particles emerging from ΔCDC50a cells would likely contain high levels of exposed envelope PS and may therefore bind PSR Tyro-3 on target cells with a greater efficiency. Instead, constitutive PS exposure on ΔCDC50a cell surfaces downregulated Tyro-3, reducing EBOV-GP-mediated entry by 78% and severely inhibiting rVSV/EBOV-GP cell-to-cell spread. Unexpectedly, we also observed that rVSV-infected ΔCDC50 cells released more VSV M protein into the supernatant, indicating that increasing outer leaflet PS on the plasma membrane enhances rVSV budding. Upon further inspection, however, ΔCDC50a-made rVSV particles were 3.2-4.8 times less infectious in Vero cells, suggesting that these cells may release non-infectious rVSV protein and RNA into the supernatant in addition to infectious rVSV virions.

We propose that EBOV-GP-mediated ΔCDC50a entry was reduced at the cell surface attachment stage with the discovery that surface Tyro-3, the primary PSR expressed in HAP1 cells, was downregulated in the cells. Our data suggests this downregulation was specific to PSRs rather than all surface molecules, because receptors and alternative entry factors sufficiently facilitated rVSV/G and CHIKV entry into ΔCDC50a cells. Tyro-3 binds to PS through adaptor proteins Gas6 or Protein S, resulting in dimerization, auto-phosphorylation, and downstream signaling resulting in apoptotic cell engulfment (29, 30). Considering ΔCDC50a cells constitutively expose PS, cell surface Tyro-3 likely encounters PS on neighboring cells, triggering Tyro-3 activation and internalization. Researchers have also noted cells undergoing non-apoptotic PS

exposure exhibit a blebbing, balloon-like morphology and/or release PS-coated vesicles, which could out-compete rVSV/EBOV-GP particles for PSR binding (31-33). Beyond reliance on PSRs, however, there are other unique characteristics of EBOV-GP-mediated entry that may have been impacted by the loss of PS internalization. Unlike VSV and CHIK, which fuse in early/less acidic endosomes, EBOV GP requires deeper trafficking into the cytoplasm, a lower pH, cathepsin processing, and NPC1 binding to complete fusion. These stages should also be explored to fully characterize how eliminating flippase activity alters EBOV entry.

We also observed a glycoprotein-independent 3.6 to 4.3-fold enhancement of rVSV budding in ΔCDC50a cells by comparing MnLuc luciferase levels in cell lysates and supernatants after one round of virus replication. Furthermore, we assessed the infectivity of ΔCDC50a-made rVSV particles relative to viral RNA copies, which revealed that these particles were less infectious than WT-made particles. Therefore, we posit that constitutive PS exposure on ΔCDC50a cells induces the nonspecific release of viral components in addition to bon-fide virions.

VSV assembly and budding occur at the cell plasma membrane and are primarily orchestrated by VSV matrix (M). While the majority of newly translated M protein can be found in the cell cytoplasm, about 10-20% associates with the plasma membrane inner leaflet and ribonucleoprotein. Meanwhile, VSV G trafficked to the cell surface via the ER-Golgi secretory pathway distributes into lipid microdomains in the plasma membrane and promotes the formation of bud sites (34). Because the final stages of VSV replication are intimately involved with plasma membrane lipid dynamics, eliminating PS internalization likely disturbed these processes. In our previous study, we found that

inhibiting PS *exposure* also alters VSV replication. Deleting apoptosis-activated PS scramblase XKR8 reduced VSV budding, slightly inhibited multi-step replication, but did not affect infectivity (16). This suggests that VSV-induced PS exposure supports efficient budding of infectious particles, but cells constitutively exposing PS do not. Inner leaflet PS may be involved in VSV budding, likely during an early stage before cytoplasmic M protein levels trigger apoptosis (35). Future investigation into the role of CDC50a in VSV production should thoroughly characterize the contents released from infected ΔCDC50a cells. We will separate mature enveloped virions from smaller vesicles and free proteins and analyze these virions for surface PS levels (to test our original hypothesis) and the incorporation of G, M, nucleoprotein (N), phosphoprotein (P), and the RNA-dependent RNA polymerase (L), which are required to execute VSV replication.

EBOV budding is highly dependent on plasma membrane PS sidedness. EBOV matrix protein VP40 dimers directly binds to inner leaflet PS and associate into higher-order oligomers, which serve as a scaffold for assembling virions (36). Curiously, cells producing VP40 also externalize PS, which we discovered occurs through caspase-cleaved XKR8 and enhances EBOV virus-like particle (VLP) budding (16). Therefore, we proposed that EBOV budding is intricately timed mechanism wherein particles assemble at the PS-rich inner leaflet of the plasma membrane followed by apoptosis signaling, XKR8 activation, and PS exposure, leading to optimal particle release. In future experiments, we will assess EBOV VP40-mediated budding efficiency in ΔCDC50a cells using the EBOV VLP model, which will enable us to bypass defective EBOV-GP-mediated entry by directly transfecting EBOV VP40, NP, and GP into cells. Future experiments should also examine the relationship between EBOV and CDC50a in

more biologically relevant systems by using WT EBOV and cell types directly implicated in EBOV pathogenesis.

Many questions remain in the field of virus-host membrane interactions, especially considering we are still identifying and defining the biological functions of membrane—regulating enzymes like flippases. Here, we discovered that CDC50a, a P4ATPase subunit essential for sequestering PS in healthy cells, was critical for EBOV-GP-mediated entry and contributes to optimal VSV replication. Other studies investigating the relationship between viruses and flippases are limited. CDC50a has appeared in viral host factor screens for arenavirus Lujo virus and coronavirus SARS-CoV2, which found that CDC50a increases cell susceptibility to virus (37, 38). In determining the human-paramyxovirus protein-protein interactome, CDC50a was found to interact with the antiviral Nipah virus C protein (an innate immunity antagonist) (39). Cumulatively, these data indicate that flippase activity may be broadly important for virus replication, and proteins like CDC50a warrant more detailed studies.

Materials and Methods

Cell lines and plasmids. Human near-haploid cells (HAP1) derived from the male chronic myelogenous leukemia cell line KBM-7, HAP1ΔATP11C (HZGHC005338c011), HAP1ΔCDC50A (HZGHC005423c007), and HAP1ΔXKR8 (HZGHC005916c007) were purchased from Horizon Discovery (United Kingdom). HAP1 and knockout cell lines were cultured in Iscove's modified Dulbecco's medium (IMDM) supplemented with 8% (v/v) fetal bovine serum (FBS). Vero-hSLAM cells (VeroS) (40) were maintained in high-glucose Dulbecco's Modified Eagle Medium

(DMEM; Mediatech, Manassas, VA, USA) supplemented with 5% fetal bovine serum (FBS; Seradigm-VWR, Radnor, PA, USA) (vol/vol) at 37°C.

Viruses. Recombinant, replication-competent VSV viruses encoding either VSV G (Indiana strain, accession number: NP_041715.1) or EBOV GP (Zaire strain accession number: AAA96744.1), GFP, and matrix (M) tagged with nano-luciferase (M-nLuc) were rescued as was previously described in chapter 2. To rescue Chikungunya virus (CHIKV) strain 181 clone 25 (181/c25), the full-length DNA CHIKV clone containing GFP was linearized and *in vitro* transcribed (Ambion, cat. AM1344) adhering to the manufacturer's protocol. Infectious CHIKV virions encoding GFP were recovered after direct RNA transfection (1μg) into Vero cells with Lipofectamine 3000 (Thermofisher, cat. L3000001). All experiments were completed with virus produced from passage 3 or 4 in Vero cells. Viral titers were determined by performing end-point dilutions on HAP1 or VeroS cells and calculating the 50% tissue culture infective dose ($TCID_{50}$) according to the Spearman-Karber method (41).

Cell Surface PS quantification. HAP1 WT, ΔXKR8, and ΔCDC50a cells were seeded in 24-well plates (HAP1 5×10^5 cells/mL). One subset of each cell type was treated with 1 μM MG132 20-24 hours prior to harvesting. Treated and untreated cells were trypsinized, pelleted (300 × g for 10 min at 4°C) and washed with 1X PBS. Cells were resuspended in 100 μL of 1X AnV binding buffer (10 mM HEPES, 140 mM NaCl, and 2.5 mM $CaCl_2$, pH 7.4) containing AnnexinV-PacificBlue (AnV-PacBlue, Invitrogen) and propidium iodide (Sigma Aldrich). Cells were stained for 30 minutes at 4°C in the dark then diluted 1:5 in AnV binding buffer and analyzed by flow cytometry using the BD-LSRII. Cell populations were gated using forward scatter/side scatter. We excluded

doublets and cell aggregates by gating cell populations using side scatter area/side scatter height. The same gates were used for all samples. Mean Fluorescence Intensity (MFI) of the Pacific Blue fluorophore in PI negative cells was quantified and averaged over a minimum of three independent experiments.

Virus replication curves. HAP1 WT, ΔCDC50a, and ΔXKR8 knockout cells were seeded in a 12-well plate at 2.5×10^5 cells/mL. After 24 hours, cells were infected with rVSV/G (MOI=0.01) or rVSV/EBOV-GP MOI (MOI=0.1). Two hours later, the infectious supernatant was replaced with fresh Iscove's media and then immediately collected for time point 0. At each indicated time point, the supernatant was collected and replaced with fresh Iscove's media and then stored at -80°C. Samples were titrated by $TCID_{50}$ on Vero cells.

Entry assays. *rVSV entry*. HAP1 WT and ΔCDC50a cells were seeded in 24-well plates (5×10^5 cells/mL) and incubated for approximately 24 hours. Cells were infected with rVSV/G or rVSV/EBOV-GP using a volume of stock required to yield ~50% GFP+ cells after one round of replication. Three hours after infection, virus inoculum was removed and replaced with serum containing media with 10mM of ammonium chloride (42). Cells were harvested 12 hours after infection and analyzed via flow cytometry.

CHIKV entry. HAP1 WT and ΔCDC50a cells were seeded in 48-well plates (3×10^5 cells/mL) and incubated for approximately 24 hours. Cells were then infected with CHIKV (MOI 0.3). Viral inoculum was removed and replaced with complete medium 1 hour after infection, and 30 mM ammonium chloride was added 2 hours later. Cells were lifted 12 hours following infection, resuspended in PBS, fixed in with formaldehyde, and analyzed via flow cytometry.

rVSV/EBOV-GP entry rescue. HAP1 and ΔCDC50a cells were seeded in 24-well plates (5×10^5 cells/mL) and incubated for approximately 24 hours. ΔCDC50a cells were infected with 1X, 5X, and 10X more infectious particles relative to HAP1 cells and incubated for 12 hours. Cells were then harvested and analyzed via flow cytometry.

*Flow cytomet*ry. Cell populations were gated using forward scatter/side scatter. We excluded doublets and cell aggregates by gating cell populations using side scatter area/side scatter height. % GFP+ cells were quantified and averaged over a minimum of three independent experiments. All cells were analyzed using the Acea Novocyte Quanteon 4025.

Tyro3 surface biotinylation. HAP1 WT and knockout cells were seeded in a 6-well plate at 2.5×10^5 cells/mL and incubated for 48 hours. Cell were then washed with cold PBS and biotinylated with 0.5 mg/ml sulfosuccinimidyl-2-(biotinamido) ethyl-1,3-dithiopropionate (Thermo) while gently shaking for 45 minutes on ice. The reaction was quenched using Tris-HCl. Cells were lysed in M2 lysis buffer (50 mM Tris [pH 7.4], 150 mM NaCl, 1 mM EDTA, 1% Triton X-100) at 4°C and clarified with centrifugation 17,000 × g, 10 min). Lysate was incubated with streptavidin Sepharose beads (GE Healthcare) overnight while rotating at 4°C. Following incubation, the streptavidin Sepharose beads were washed in buffer 1 (100 mM Tris, 500 mM lithium chloride, 0.1% Triton X-100) and then in buffer 2 (20 mM HEPES [pH 7.2], 2 mM EGTA, 10 mM magnesium chloride, 0.1% Triton X-100), incubated in urea buffer (200 mM Tris [pH 6.8], 8 M urea, 5% sodium dodecyl sulfate [SDS], 0.1 mM EDTA, 0.03% bromophenol blue, 1.5% dithiothreitol [DTT]) for 30 minutes at 56°C, and subjected to immunoblot analysis using anti-βactin C4 (1:1000, Santa Cruz Biotechnology, sc-47778) and anti-

Tyro-3 (1:1000, R&D Systems, MAB859100) antibodies. Immunoblots were probed with appropriate secondary antibodies conjugated with HRP and imaged with a ChemiDoc XRS digital imaging system (Bio-Rad).

rVSV Budding. HAP1 WT and ΔCDC50a cells were infected rVSV/EBOV-GP-MnLuc and rVSV/G-MnLuc with (MOI 0.5) for 2 hours at 37°C, after which inoculum was removed, cells were treated with citric acid, washed, and replaced with fresh media. Eight hours (rVSV/G) and 12 hours (rVSV/EBOV-GP) after infection, supernatants were collected and cells were lysed in M2 lysis buffer (50 mM Tris [pH 7.4], 150 mM NaCl, 1 mM EDTA, 1% Triton X-100) at 4°C and clarified with centrifugation (20,000 × *g*, 15 min). Lysates and supernatants were assayed for nano-luciferase activity using Nano-Glo luciferase substrate (Promega) and luminescence was measured in the Glomax® Explorer (Promega). Budding efficiency was calculated by dividing the luminescent signals from the supernatant by the cell lysate, and HAP1 budding efficiency was set to 100%.

Viral particle infectivity. *Virus production*. HAP1 and ΔCDC50a cells were seeded in 12-well plates (5×10^5 cells/mL). After 24 hours, cells were infected with rVSV/G (MOI= 1) or rVSV/EBOV-GP (HAP MOI= 1, ΔCDC50a 20X) for 2 hours at 37°C and 5% CO_2. Due to rVSV/EBOV-GP replicating and spreading in ΔCDC50a cells at a much slower rate than in WT cells, more virus was added so a similar level of infection had occurred in both populations after one round of replication. Virus-containing media was removed, cells were treated with citric acid buffer for 1 minute and washed, and fresh Iscove's media was added. Cellular supernatant was collected 4 and 8 hours after rVSV/G and rVSV/EBOV-GP infection, respectively, cleared using centrifugation, and stored at -80°C.

qRT-PCR. Viral RNA was isolated from infected cell supernatant (QIAamp® Viral RNA Mini Kit, Qiagen. RNA was reverse transcribed into cDNA (High-Capacity RNA-to-cDNA™ Kit, Thermo Scientific). VSV genome copies were measured with qRT-PCR using the TaqMan Gene Expression Master Mix (Applied Biosystems), VSV-L forward and reverse primers, and probe (TaqMan MGB Probe) (43). Each sample was analyzed in duplicate, and each assay contained a DNA standard curve (VSV molecular clone, ranged from 3 to 3×10^7 plasmid copies), no template, and no primer controls. Because the primers detect VSV-L RNAs, copies generated from cellular RNA detected both full-length genome as well as VSV-L transcripts. We extrapolated VSV copy numbers from the generated standard curve using the Applied Biosystems protocol. Final copy numbers were adjusted by back-calculations to the total RNA and cDNA volume and expressed as copies per lysate or supernatant sample.

Genome:PFU analysis. The infectivities of viruses produced in HAP1 and ΔCDC50a cells were calculated by taking the ratio of genome copy numbers to PFU/mL for each sample. The PFU/mL for all samples was determined using plaque assays on Vero cells. Genome:PFU values were averaged from virus produced from three independent trials.

Acknowledgements

We thank the CVM Cytometry Core Facility for technical assistance.

Research reported in this publication was supported by the National Institute of Allergy and Infectious Diseases of the National Institutes of Health under Award Number R01AI139238. The content is solely the responsibility of the authors and does not necessarily represent the official views of the National Institutes of Health.

ARJ was supported by NIGMS grant GM109435, Post-Baccalaureate Training in Infectious Diseases Research.

References

1. WHO. 10 Feb 2020. Ebola Virus Disease. https://www.who.int/news-room/fact-sheets/detail/ebola-virus-disease. Accessed 10 Dec 2020.

2. Rojas M, Monsalve DM, Pacheco Y, Acosta-Ampudia Y, Ramirez-Santana C, Ansari AA, Gershwin ME, Anaya JM. 2020. Ebola virus disease: An emerging and re-emerging viral threat. J Autoimmun 106:102375.

3. Prescott JB, Marzi A, Safronetz D, Robertson SJ, Feldmann H, Best SM. 2017. Immunobiology of Ebola and Lassa virus infections. Nat Rev Immunol 17:195-207.

4. Fujihira H, Usami K, Matsuno K, Takeuchi H, Denda-Nagai K, Furukawa J-i, Shinohara Y, Takada A, Kawaoka Y, Irimura T. 2018. A Critical Domain of Ebolavirus Envelope Glycoprotein Determines Glycoform and Infectivity. Scientific Reports 8:5495.

5. Davey RA, Shtanko O, Anantpadma M, Sakurai Y, Chandran K, Maury W. 2017. Mechanisms of Filovirus Entry. Curr Top Microbiol Immunol 411:323-352.

6. Mulherkar N, Raaben M, de la Torre JC, Whelan SP, Chandran K. 2011. The Ebola virus glycoprotein mediates entry via a non-classical dynamin-dependent macropinocytic pathway. Virology 419:72-83.

7. Bo Y, Qiu S, Mulloy RP, Côté M. 2020. Filoviruses Use the HOPS Complex and UVRAG To Traffic to Niemann-Pick C1 Compartments during Viral Entry. J Virol 94.

8. Carette JE, Raaben M, Wong AC, Herbert AS, Obernosterer G, Mulherkar N, Kuehne AI, Kranzusch PJ, Griffin AM, Ruthel G, Dal Cin P, Dye JM, Whelan SP, Chandran K, Brummelkamp TR. 2011. Ebola virus entry requires the cholesterol transporter Niemann-Pick C1. Nature 477:340-3.

9. Chandran K, Sullivan NJ, Felbor U, Whelan SP, Cunningham JM. 2005. Endosomal proteolysis of the Ebola virus glycoprotein is necessary for infection. Science 308:1643-5.

10. Hunt CL, Kolokoltsov AA, Davey RA, Maury W. 2011. The Tyro3 receptor kinase Axl enhances macropinocytosis of Zaire ebolavirus. J Virol 85:334-47.

11. Gordon TB, Hayward JA, Marsh GA, Baker ML, Tachedjian G. 2019. Host and Viral Proteins Modulating Ebola and Marburg Virus Egress. Viruses 11:25.

12. Moller-Tank S, Kondratowicz AS, Davey RA, Rennert PD, Maury W. 2013. Role of the phosphatidylserine receptor TIM-1 in enveloped-virus entry. J Virol 87:8327-41.

13. Stewart CM, Phan A, Bo Y, LeBlond ND, Smith TKT, Laroche G, Giguere PM, Fullerton MD, Pelchat M, Kobasa D, Cote M. 2021. Ebola virus triggers receptor tyrosine kinase-dependent signaling to promote the delivery of viral particles to entry-conducive intracellular compartments. PLoS Pathog 17:e1009275.

14. Brunton B, Rogers K, Phillips EK, Brouillette RB, Bouls R, Butler NS, Maury W. 2019. TIM-1 serves as a receptor for Ebola virus in vivo, enhancing viremia and pathogenesis. PLoS Negl Trop Dis 13:e0006983.

15. Younan P, Iampietro M, Nishida A, Ramanathan P, Santos RI, Dutta M, Lubaki NM, Koup RA, Katze MG, Bukreyev A. 2017. Ebola Virus Binding to Tim-1 on T Lymphocytes Induces a Cytokine Storm. mBio 8.

16. Acciani MD, Lay Mendoza MF, Havranek KE, Duncan AM, Iyer H, Linn OL, Brindley MA. 2021. Ebola virus requires phosphatidylserine scrambling activity for efficient budding and optimal infectivity. J Virol doi:10.1128/JVI.01165-21:JVI0116521.

17. Younan P, Iampietro M, Santos RI, Ramanathan P, Popov VL, Bukreyev A. 2018. Role of Transmembrane Protein 16F in the Incorporation of Phosphatidylserine Into Budding Ebola Virus Virions. J Infect Dis 218:S335-S345.

18. Nanbo A, Maruyama J, Imai M, Ujie M, Fujioka Y, Nishide S, Takada A, Ohba Y, Kawaoka Y. 2018. Ebola virus requires a host scramblase for externalization of phosphatidylserine on the surface of viral particles. PLoS Pathog 14:e1006848.

19. Han Z, Madara JJ, Herbert A, Prugar LI, Ruthel G, Lu J, Liu Y, Liu W, Liu X, Wrobel JE, Reitz AB, Dye JM, Harty RN, Freedman BD. 2015. Calcium Regulation of Hemorrhagic Fever Virus Budding: Mechanistic Implications for Host-Oriented Therapeutic Intervention. PLoS Pathog 11:e1005220.

20. Olejnik J, Alonso J, Schmidt KM, Yan Z, Wang W, Marzi A, Ebihara H, Yang J, Patterson JL, Ryabchikova E, Muhlberger E. 2013. Ebola virus does not block apoptotic signaling pathways. J Virol 87:5384-96.

21. Segawa K, Kurata S, Yanagihashi Y, Brummelkamp TR, Matsuda F, Nagata S. 2014. Caspase-mediated cleavage of phospholipid flippase for apoptotic phosphatidylserine exposure. Science 344:1164-8.

22. Bevers EM, Williamson PL. 2016. Getting to the Outer Leaflet: Physiology of Phosphatidylserine Exposure at the Plasma Membrane. Physiol Rev 96:605-45.

23. Nakanishi H, Irie K, Segawa K, Hasegawa K, Fujiyoshi Y, Nagata S, Abe K. 2020. Crystal structure of a human plasma membrane phospholipid flippase. J Biol Chem 295:10180-10194.

24. Segawa K, Kurata S, Nagata S. 2016. Human Type IV P-type ATPases That Work as Plasma Membrane Phospholipid Flippases and Their Regulation by Caspase and Calcium. J Biol Chem 291:762-72.

25. Kotecki M, Reddy PS, Cochran BH. 1999. Isolation and characterization of a near-haploid human cell line. Exp Cell Res 252:273-80.

26. Morizono K, Chen IS. 2014. Role of phosphatidylserine receptors in enveloped virus infection. J Virol 88:4275-90.

27. Jemielity S, Wang JJ, Chan YK, Ahmed AA, Li W, Monahan S, Bu X, Farzan M, Freeman GJ, Umetsu DT, Dekruyff RH, Choe H. 2013. TIM-family proteins promote infection of multiple enveloped viruses through virion-associated phosphatidylserine. PLoS Pathog 9:e1003232.

28. Tanaka A, Tumkosit U, Nakamura S, Motooka D, Kishishita N, Priengprom T, Sa-Ngasang A, Kinoshita T, Takeda N, Maeda Y. 2017. Genome-Wide Screening Uncovers the Significance of N-Sulfation of Heparan Sulfate as a Host Cell Factor for Chikungunya Virus Infection. J Virol 91.

29. Myers KV, Amend SR, Pienta KJ. 2019. Targeting Tyro3, Axl and MerTK (TAM receptors): implications for macrophages in the tumor microenvironment. Mol Cancer 18:94.

30. Shimojima M, Takada A, Ebihara H, Neumann G, Fujioka K, Irimura T, Jones S, Feldmann H, Kawaoka Y. 2006. Tyro3 family-mediated cell entry of Ebola and Marburg viruses. J Virol 80:10109-16.

31. Gong YN, Guy C, Olauson H, Becker JU, Yang M, Fitzgerald P, Linkermann A, Green DR. 2017. ESCRT-III Acts Downstream of MLKL to Regulate Necroptotic Cell Death and Its Consequences. Cell 169:286-300 e16.

32. Reddy EC, Rand ML. 2020. Procoagulant Phosphatidylserine-Exposing Platelets in vitro and in vivo. Front Cardiovasc Med 7:15.

33. Shlomovitz I, Speir M, Gerlic M. 2019. Flipping the dogma - phosphatidylserine in non-apoptotic cell death. Cell Commun Signal 17:139.

34. Jayakar HR, Jeetendra E, Whitt MA. 2004. Rhabdovirus assembly and budding. Virus Res 106:117-32.

35. Irie T, Liu Y, Drolet BS, Carnero E, Garcia-Sastre A, Harty RN. 2012. Cytopathogenesis of vesicular stomatitis virus is regulated by the PSAP motif of M protein in a species-dependent manner. Viruses 4:1605-18.

36. Adu-Gyamfi E, Johnson KA, Fraser ME, Scott JL, Soni SP, Jones KR, Digman MA, Gratton E, Tessier CR, Stahelin RV. 2015. Host Cell Plasma Membrane Phosphatidylserine Regulates the Assembly and Budding of Ebola Virus. J Virol 89:9440-53.

37. Baggen J, Persoons L, Vanstreels E, Jansen S, Van Looveren D, Boeckx B, Geudens V, De Man J, Jochmans D, Wauters J, Wauters E, Vanaudenaerde BM, Lambrechts D, Neyts J, Dallmeier K, Thibaut HJ, Jacquemyn M, Maes P, Daelemans D. 2021. Genome-wide CRISPR screening identifies TMEM106B as a proviral host factor for SARS-CoV-2. Nat Genet 53:435-444.

38. Raaben M, Jae LT, Herbert AS, Kuehne AI, Stubbs SH, Chou YY, Blomen VA, Kirchhausen T, Dye JM, Brummelkamp TR, Whelan SP. 2017. NRP2 and CD63 Are Host Factors for Lujo Virus Cell Entry. Cell Host Microbe 22:688-696 e5.

39. Martinez-Gil L, Vera-Velasco NM, Mingarro I. 2017. Exploring the Human-Nipah Virus Protein-Protein Interactome. J Virol 91.

40. Ono N, Tatsuo H, Hidaka Y, Aoki T, Minagawa H, Yanagi Y. 2001. Measles Viruses on Throat Swabs from Measles Patients Use Signaling Lymphocytic Activation Molecule (CDw150) but Not CD46 as a Cellular Receptor. Journal of Virology 75:4399-4401.

41. Ramakrishnan MA. 2016. Determination of 50% endpoint titer using a simple formula. World J Virol 5:85-6.

42. Lay Mendoza MF, Acciani MD, Levit CN, Santa Maria C, Brindley MA. 2020. Monitoring Viral Entry in Real-Time Using a Luciferase Recombinant Vesicular Stomatitis Virus Producing SARS-CoV-2, EBOV, LASV, CHIKV, and VSV Glycoproteins. Viruses 12:1457.

43. Hole K, Clavijo A, Pineda LA. 2006. Detection and serotype-specific differentiation of vesicular stomatitis virus using a multiplex, real-time, reverse transcription-polymerase chain reaction assay. J Vet Diagn Invest 18:139-46.

CHAPTER 6: CONCLUSIONS

Summary and Conclusions

Hemorrhagic fever viruses LASV and EBOV demonstrate complex surface receptor/attachment factor usage, interacting with glycans, lectins, and/or PSRs in addition to high-affinity receptors. Target cells may display one or more of these evolutionarily conserved attachment factors at any given time, enabling LASV and EBOV to infect a wide variety of cell types, tissues, and vertebrates. In order to develop effective vaccines and therapeutics against these dangerous emerging pathogens, we must understand the viral and host cell determinants governing viral entry.

For LASV, which binds to cell surfaces using high affinity receptor αDG, previous work identified the general domains in GP1 and αDG that interact during attachment and several neutralizing epitopes on GP1 and GP2 (1-3). However, no studies performed in-depth biochemical analysis of LASV GP1 to locate the receptor binding site. Thus, in Chapter 3, we probed LASV GP1 for sites critical for high-affinity interactions with αDG using insertional mutagenesis, carbohydrate shielding, and alanine scanning mutagenesis. We determined that GP1 residues between 141-150 form a putative receptor binding site at the top central core of the GP trimer and that residues between 248-250, located deeper in the trimer core, may be more important for the formation of the αDG binding domain above. Importantly, inhibiting LASV-GP-αDG binding did not completely inhibit VSV pseudoparticle transduction in HAP1 cells, leading us to investigate alternative LASV attachment mechanisms.

There are many outstanding questions regarding LASV and EBOV attachment and internalization using PSRs. *In vitro* assays using BSL-2 LASV and EBOV models identified several PSRs that can mediate or enhance entry (4-13); however, the roles of PSRs in *in vivo* entry are not well-characterized (14, 15). No studies examined viral envelope requirements for apoptotic mimicry until 2018, when cellular scramblases TMEM16F and XKR8 were each implicated in increased EBOV envelope PS and infectivity (16, 17). These scramblases are activated through distinct pathways, thus their involvement in EBOV replication also implies certain cell signaling events occurring in EBOV-infected cells. In Chapter 4, we sought to clarify the contributions of calcium-activated scramblase TMEM16F and apoptosis-activated scramblase XKR8 in EBOV PS levels using HAP1 CRISPR knockout cell lines. We found that XKR8 is required for increased rVSV/EBOV-GP PS levels and infectivity, while TMEM16F was dispensable. Our data also suggested that XKR8 activity improved rVSV budding. Upon further investigation, we discovered that caspase-cleaved XKR8 scrambling promoted optimal EBOV VLP budding. Therefore, we concluded that in HAP1 cells, apoptosis-induced PS scrambling facilitates to optimal EBOV budding, PS levels, and infectivity. Interestingly, EBOV does not always trigger the classical hallmarks of apoptosis, and limited caspase activation has been observed in EBOV-infected cells (16-20). Future studies should elucidate the upstream factors leading to XKR8 activation in EBOV-infected cells. Furthermore, because TMEM16F was not the primary mediator of calcium-induced PS scrambling in HAP1 cells, we could not rule out this pathway as a contributing factor to EBOV PS levels or budding. Additional experiments must identify and target the primary

calcium-activated scramblase(s) in HAP1 cells to fully determine the roles of each pathway in EBOV replication.

In Chapter 5 we sought to alter EBOV envelope PS levels and infectivity by targeting host proteins ATP11C and CDC50a. ATP11C is the most well-characterized PS-specific plasma membrane flippase, and its associated subunit CDC50a is essential for all P4 ATPase folding, transport, and functionality. Our data indicated that ATP11C was not a primary flippase in HAP1 cells. However, deleting all P4 ATPase activity in ΔCDC50a cells inhibited PS internalization in normal state cells and raised apoptotic PS levels relative to those of apoptotic WT cells. We also determined that constitutive PS exposure in HAP1 cells downregulated cell surface PSR levels and reduced rVSV/EBOV-GP entry. This not only supports the role of PSRs in EBOV entry, but also suggests that cells exposing PS even transiently may be refractory to EBOV entry. Finally, we observed significantly higher levels of rVSV budding in ΔCDC50a cells which, when combined with the finding that these particles were proportionally less infectious, lead us to speculate that inner leaflet PS may be required for the efficient assembly and budding of infectious VSV particles. Because matrix VP40-PS binding is essential for EBOV budding, we also expect this process will be altered in ΔCDC50a cells. Although we originally intended to use ΔCDC50a cells as a tool to alter viral envelopes, we learned that regular cellular maintenance of inner leaflet PS impacts other aspects of virus replication. Moving forward, ΔCDC50a cells may be particularly useful in conjunction with ΔXKR8 cells for examining lipid-dependent budding and egress of other viruses at the cell surface.

Because PS plays an integral role in membrane integrity, fluidity, and curvature, it is unsurprising that PS-distributing enzymes were recently implicated in additional stages of virus replication, specifically in those involving cell membrane rearrangements. Several studies suggest that calcium-activated TMEM16F scrambling enhances HIV and SARS-CoV-2 viral envelope-cellular membrane fusion at the cell surface (21-23). For (+) RNA flaviviruses and coronaviruses, which form membranous replication complexes (RCs) on the ER, scramblase TMEM41B was required for RC formation and genome replication (24-29). Considering these enzymes and XKR8, ATP11C, and CDC50a were only recently identified, there is much left to discover about their significance in virus replication. Their structures, functions, and upstream effectors are not yet fully characterized but will likely be critical for fully understanding how viral infection changes the lipid landscape in host cell membranes to optimize replication.

Final Remarks

We currently face many challenges in preventing and controlling future LASV and EBOV outbreaks. While there are several promising preclinical vaccine candidates against the LASV-GP and one approved vaccine against the EBOV Zaire GP, these vaccines each target only one of several pathogenic strains or species and evidence of cross-protection is limited (30-33). New strains may also emerge as a result of highly likely zoonotic crossover events, necessitating the development and implementation of effective therapeutics. Current therapeutics such as antivirals and monoclonal GP-specific antibodies have demonstrated varying individual success, leading scientists to recommend combination therapies of mechanistically independent therapeutics (34-36). Here, we investigated glycoprotein-dependent and -independent mechanisms of

hemorrhagic fever virus entry to improve upon and expand our arsenal of virus-targeting treatments. We identified the putative LASV GP1-αDG binding site, which is conserved among LASV strains and across Old World arenaviruses that use αDG. We also discovered new roles for conserved PS-regulating enzymes XKR8 and CDC50a in EBOV replication, illustrating the reliance of enveloped viruses on plasma membrane lipid dynamics and indicating the presence of upstream apoptosis activators in EBOV-infected cells. In sum, this work improved our understanding of specific and broad requirements for hemorrhagic fever virus replication and illuminated a portion of the complex relationship between viruses and cellular lipids.

References

1. Robinson JE, Hastie KM, Cross RW, Yenni RE, Elliott DH, Rouelle JA, Kannadka CB, Smira AA, Garry CE, Bradley BT, Yu H, Shaffer JG, Boisen ML, Hartnett JN, Zandonatti MA, Rowland MM, Heinrich ML, Martinez-Sobrido L, Cheng B, de la Torre JC, Andersen KG, Goba A, Momoh M, Fullah M, Gbakie M, Kanneh L, Koroma VJ, Fonnie R, Jalloh SC, Kargbo B, Vandi MA, Gbetuwa M, Ikponmwosa O, Asogun DA, Okokhere PO, Follarin OA, Schieffelin JS, Pitts KR, Geisbert JB, Kulakoski PC, Wilson RB, Happi CT, Sabeti PC, Gevao SM, Khan SH, Grant DS, Geisbert TW, Saphire EO, Branco LM, Garry RF. 2016. Most neutralizing human monoclonal antibodies target novel epitopes requiring both Lassa virus glycoprotein subunits. Nat Commun 7:11544.

2. Kunz S, Rojek JM, Kanagawa M, Spiropoulou CF, Barresi R, Campbell KP, Oldstone MB. 2005. Posttranslational modification of alpha-dystroglycan, the cellular receptor for arenaviruses, by the glycosyltransferase LARGE is critical for virus binding. J Virol 79:14282-96.

3. Kunz S, Rojek JM, Perez M, Spiropoulou CF, Oldstone MB. 2005. Characterization of the interaction of lassa fever virus with its cellular receptor alpha-dystroglycan. J Virol 79:5979-87.

4. Shimojima M, Stroher U, Ebihara H, Feldmann H, Kawaoka Y. 2012. Identification of cell surface molecules involved in dystroglycan-independent Lassa virus cell entry. J Virol 86:2067-78.

5. Brouillette RB, Phillips EK, Patel R, Mahauad-Fernandez W, Moller-Tank S, Rogers KJ, Dillard JA, Cooney AL, Martinez-Sobrido L, Okeoma C, Maury W.

2018. TIM-1 Mediates Dystroglycan-Independent Entry of Lassa Virus. J Virol 92.

6. Fedeli C, Torriani G, Galan-Navarro C, Moraz ML, Moreno H, Gerold G, Kunz S. 2018. Axl Can Serve as Entry Factor for Lassa Virus Depending on the Functional Glycosylation of Dystroglycan. J Virol 92.

7. Jemielity S, Wang JJ, Chan YK, Ahmed AA, Li W, Monahan S, Bu X, Farzan M, Freeman GJ, Umetsu DT, Dekruyff RH, Choe H. 2013. TIM-family proteins promote infection of multiple enveloped viruses through virion-associated phosphatidylserine. PLoS Pathog 9:e1003232.

8. Moller-Tank S, Kondratowicz AS, Davey RA, Rennert PD, Maury W. 2013. Role of the phosphatidylserine receptor TIM-1 in enveloped-virus entry. J Virol 87:8327-41.

9. Kondratowicz AS, Lennemann NJ, Sinn PL, Davey RA, Hunt CL, Moller-Tank S, Meyerholz DK, Rennert P, Mullins RF, Brindley M, Sandersfeld LM, Quinn K, Weller M, McCray PB, Jr., Chiorini J, Maury W. 2011. T-cell immunoglobulin and mucin domain 1 (TIM-1) is a receptor for Zaire Ebolavirus and Lake Victoria Marburgvirus. Proc Natl Acad Sci U S A 108:8426-31.

10. Shimojima M, Takada A, Ebihara H, Neumann G, Fujioka K, Irimura T, Jones S, Feldmann H, Kawaoka Y. 2006. Tyro3 family-mediated cell entry of Ebola and Marburg viruses. J Virol 80:10109-16.

11. Shimojima M, Ikeda Y, Kawaoka Y. 2007. The mechanism of Axl-mediated Ebola virus infection. J Infect Dis 196 Suppl 2:S259-63.

12. Brindley MA, Hunt CL, Kondratowicz AS, Bowman J, Sinn PL, McCray PB, Jr., Quinn K, Weller ML, Chiorini JA, Maury W. 2011. Tyrosine kinase receptor Axl enhances entry of Zaire ebolavirus without direct interactions with the viral glycoprotein. Virology 415:83-94.

13. Bhattacharyya S, Zagorska A, Lew ED, Shrestha B, Rothlin CV, Naughton J, Diamond MS, Lemke G, Young JA. 2013. Enveloped viruses disable innate immune responses in dendritic cells by direct activation of TAM receptors. Cell Host Microbe 14:136-47.

14. Younan P, Iampietro M, Nishida A, Ramanathan P, Santos RI, Dutta M, Lubaki NM, Koup RA, Katze MG, Bukreyev A. 2017. Ebola Virus Binding to Tim-1 on T Lymphocytes Induces a Cytokine Storm. mBio 8.

15. Brunton B, Rogers K, Phillips EK, Brouillette RB, Bouls R, Butler NS, Maury W. 2019. TIM-1 serves as a receptor for Ebola virus in vivo, enhancing viremia and pathogenesis. PLoS Negl Trop Dis 13:e0006983.

16. Younan P, Iampietro M, Santos RI, Ramanathan P, Popov VL, Bukreyev A. 2018. Role of Transmembrane Protein 16F in the Incorporation of Phosphatidylserine Into Budding Ebola Virus Virions. J Infect Dis 218:S335-S345.

17. Nanbo A, Maruyama J, Imai M, Ujie M, Fujioka Y, Nishide S, Takada A, Ohba Y, Kawaoka Y. 2018. Ebola virus requires a host scramblase for externalization of phosphatidylserine on the surface of viral particles. PLoS Pathog 14:e1006848.

18. Adu-Gyamfi E, Johnson KA, Fraser ME, Scott JL, Soni SP, Jones KR, Digman MA, Gratton E, Tessier CR, Stahelin RV. 2015. Host Cell Plasma Membrane Phosphatidylserine Regulates the Assembly and Budding of Ebola Virus. J Virol 89:9440-53.

19. Gupta M, Spiropoulou C, Rollin PE. 2007. Ebola virus infection of human PBMCs causes massive death of macrophages, CD4 and CD8 T cell sub-populations in vitro. Virology 364:45-54.

20. Olejnik J, Alonso J, Schmidt KM, Yan Z, Wang W, Marzi A, Ebihara H, Yang J, Patterson JL, Ryabchikova E, Muhlberger E. 2013. Ebola virus does not block apoptotic signaling pathways. J Virol 87:5384-96.

21. Zaitseva E, Zaitsev E, Melikov K, Arakelyan A, Marin M, Villasmil R, Margolis LB, Melikyan GB, Chernomordik LV. 2017. Fusion Stage of HIV-1 Entry Depends on Virus-Induced Cell Surface Exposure of Phosphatidylserine. Cell Host Microbe 22:99-110 e7.

22. Braga L, Ali H, Secco I, Chiavacci E, Neves G, Goldhill D, Penn R, Jimenez-Guardeno JM, Ortega-Prieto AM, Bussani R, Cannata A, Rizzari G, Collesi C, Schneider E, Arosio D, Shah AM, Barclay WS, Malim MH, Burrone J, Giacca M. 2021. Drugs that inhibit TMEM16 proteins block SARS-CoV-2 spike-induced syncytia. Nature 594:88-93.

23. Chua BA, Ngo JA, Situ K, Morizono K. 2019. Roles of phosphatidylserine exposed on the viral envelope and cell membrane in HIV-1 replication. Cell Commun Signal 17:132.

24. Huang D, Xu B, Liu L, Wu L, Zhu Y, Ghanbarpour A, Wang Y, Chen FJ, Lyu J, Hu Y, Kang Y, Zhou W, Wang X, Ding W, Li X, Jiang Z, Chen J, Zhang X, Zhou H, Li JZ, Guo C, Zheng W, Zhang X, Li P, Melia T, Reinisch K, Chen XW. 2021. TMEM41B acts as an ER scramblase required for lipoprotein biogenesis and lipid homeostasis. Cell Metab doi:10.1016/j.cmet.2021.05.006.

25. Li YE, Wang Y, Du X, Zhang T, Mak HY, Hancock SE, McEwen H, Pandzic E, Whan RM, Aw YC, Lukmantara IE, Yuan Y, Dong X, Don A, Turner N, Qi S, Yang H. 2021. TMEM41B and VMP1 are scramblases and regulate the distribution of cholesterol and phosphatidylserine. J Cell Biol 220.

26. Ghanbarpour A, Valverde DP, Melia TJ, Reinisch KM. 2021. A model for a partnership of lipid transfer proteins and scramblases in membrane expansion and organelle biogenesis. Proc Natl Acad Sci U S A 118.

27. Hoffmann HH, Schneider WM, Rozen-Gagnon K, Miles LA, Schuster F, Razooky B, Jacobson E, Wu X, Yi S, Rudin CM, MacDonald MR, McMullan LK, Poirier JT, Rice CM. 2021. TMEM41B Is a Pan-flavivirus Host Factor. Cell 184:133-148 e20.

28. Schneider WM, Luna JM, Hoffmann HH, Sanchez-Rivera FJ, Leal AA, Ashbrook AW, Le Pen J, Ricardo-Lax I, Michailidis E, Peace A, Stenzel AF, Lowe SW, MacDonald MR, Rice CM, Poirier JT. 2021. Genome-Scale Identification of SARS-CoV-2 and Pan-coronavirus Host Factor Networks. Cell 184:120-132 e14.

29. Baggen J, Persoons L, Vanstreels E, Jansen S, Van Looveren D, Boeckx B, Geudens V, De Man J, Jochmans D, Wauters J, Wauters E, Vanaudenaerde BM, Lambrechts D, Neyts J, Dallmeier K, Thibaut HJ, Jacquemyn M, Maes P, Daelemans D. 2021. Genome-wide CRISPR screening identifies TMEM106B as a proviral host factor for SARS-CoV-2. Nat Genet 53:435-444.

30. Warner BM, Safronetz D, Stein DR. 2018. Current research for a vaccine against Lassa hemorrhagic fever virus. Drug Des Devel Ther 12:2519-2527.

31. Lukashevich IS, Paessler S, de la Torre JC. 2019. Lassa virus diversity and feasibility for universal prophylactic vaccine. F1000Res 8.

32. Ibukun FI. 2020. Inter-Lineage Variation of Lassa Virus Glycoprotein Epitopes: A Challenge to Lassa Virus Vaccine Development. Viruses 12.

33. Suder E, Furuyama W, Feldmann H, Marzi A, de Wit E. 2018. The vesicular stomatitis virus-based Ebola virus vaccine: From concept to clinical trials. Hum Vaccin Immunother 14:2107-2113.

34. Cross RW, Hastie KM, Mire CE, Robinson JE, Geisbert TW, Branco LM, Ollmann Saphire E, Garry RF. 2019. Antibody therapy for Lassa fever. Curr Opin Virol 37:97-104.

35. Hansen F, Jarvis MA, Feldmann H, Rosenke K. 2021. Lassa Virus Treatment Options. Microorganisms 9.

36. Iversen PL, Kane CD, Zeng X, Panchal RG, Warren TK, Radoshitzky SR, Kuhn JH, Mudhasani RR, Cooper CL, Shurtleff AC, Nasar F, Sunay MM, Duplantier AJ, Eaton BP, Zumbrun EE, Bixler SL, Martin S, Meinig JM, Chiang CY, Sanchez-Lockhart M, Palacios GF, Kugelman JR, Martins KA, Pitt ML, Crozier I, Saunders DL. 2020. Recent successes in therapeutics for Ebola virus disease: no time for complacency. Lancet Infect Dis 20:e231-e237.